6.

High resolution modeling of meteorological, hydrodynamic, wave and sediment processes in SAMP study area

by

Stephan Grilli[1], Jeffrey Harris[1], Ravi Sharma[1], Lauren Decker[2], David Stuebe[2], Danny Mendelsohn[2], Deborah Crowley[2] and Steve Decker[3]

1. Department of Ocean Engineering, University of Rhode Island
2. Applied Sciences Associates, Inc., Wakefield, RI
3. Rutgers University

University of Rhode Island, July 13, 2010

Executive Summary

This work was performed as a part of the Rhode Island Ocean Special Area Management Plan (SAMP), to acquire insight into local meteorological, hydrodynamic, wave, and sediment processes. The approach followed consists in first performing an exhaustive literature review of relevant work to date in the area, and then in light of this, to develop and apply numerical models of wind, wave, current, and sediment suspension and transport processes. Several models were considered and used, including two for simualting wind fields over Block Island (WRF and RAMS), and a coupled hydrodynamic, wave, and sediment model of the waters of southern New England (ROMS/SWAN). Additionally since tides are the key and ever present forcing for sediment processes in local shelf waters, an additional and independent tidal model was applied (HYDROMAP), whose results were compared to ROMS to provide cross-validation.

Atmospheric modeling with WRF was performed in collaboration with Applied Sciences Associates (ASA) to show effects of Block Island on wind velocity and shear in the wake of the island. Detailed two-dimensional (2D) simulations in vertical planes were performed across the island, for 8 main wind directions and a variety of atmospheric shear (i.e., neutral, stable, unstable) related to air-sea temperature differences. A limited number of three-dimensional (3D) simulations were then performed with WRF, but due to computational limitations, work was shifted to using the less computationally intensive "Regional Atmospheric Model System" (RAMS), for 3D simulations, as part of a collaboration with Weatherflow Inc. (this part of the work is only summarized in this report and reported on in detailed elsewhere). RAMS was used to create a five-month (10/09-2/10) high-resolution hindcast of the wind fields over Block Island, using a 4 level nesting model, with increasing resolution, whose finer encompassed the entire SAMP study area. These fields were then used to force the hydrodynamic model ROMS.

The "Regional Ocean Modeling System" (ROMS) was used to simulate currents due to various environmental forcing, in a computational domain extending from Long Island Sound to the Nantucket Shoals at a grid resolution of 600 m. Various configurations were considered: (i) only tidal forcing; (ii) tidal and wind forcing; and (iii) tidal, wind, and wave forcings (the latter using the wave model SWAN coupled to ROMS, with boundary conditions obtained form the larger scale operational wave model WAVEWATCH III). In addition, all ROMS simulations included an embedded sediment suspension and transport model, which was used to study sediment suspension in the SAMP study area.

HYDROMAP simulations were performed using tidal and wind forcing (although only spatially uniform wind forcing given from a point-measurement were used), and compared to ROMS results for the same forcing cases. HYDROMAP results generally supported similar ROMS results and at higher spatial resolution, although HYDROMAP was not used to study the effects of sediment suspension.

All results are compared against available data. RAMS simulations results for wind speed and direction were extensively compared to and validated with field data (this is reported on in detail elsewhere). Wave and current data recorded at five buoys in and near the SAMP study area, for the period from October 2009 to January 2010, was favorably compared to ROMS simulation results for the same period. Surficial sediment processes simulated with ROMS/SWAN were also qualitatively compared to measurements at the field buoys (using backscattering level in ADCP measurements as an indicator of sediment suspension concentration).

Overall simulation results indicate that some level of sediment suspension occurs in limited locations of the SAMP area, due to tidal forcing, and additional suspension occurs in shallower waters, as a result of episodes of strong long swells. None of this sediment activity, however, should pose a problem for wind turbine foundation.

Table of Contents

List of Figures

List of Tables

List of Attachments and Appendices

Appendix A : HYDROMAP tidal simulations.

Abstract

As a part of the Rhode Island Ocean Special Area Management Plan (SAMP) work, local meteorological, hydrodynamic, wave, and sediment processes are studied through numerical simulation, analyzed and summarized in this report. The work consists in both a literature review and the application of numerical models. Several models were considered, including two of the wind over Block Island (WRF and RAMS), a coupled hydrodynamic, wave, and sediment model of the waters of southern New England (ROMS/SWAN), and an additional tidal model (HYDROMAP). Results are compared against available data, including surficial sediment properties and processes, and wave and current data recorded at five buoys in and near the SAMP study area for the period from October 2009 to January 2010.

Overall simulation results indicate that some level of sediment suspension occurs in limited locations of the SAMP area, due to tidal forcing, and additional suspension occurs in shallower waters, as a result of episodes of strong long swells. None of this sediment activity, however, should pose a problem for wind turbine foundation.

1 Background

It has been proposed that a wind turbine farm be developed off the southeastern coast of Block Island, south of the Rhode Island mainland. The development of an offshore wind farm will necessarily require a great deal of underwater construction including drilling and setting the piles for the turbine foundations, burying electrical transmission cables and other infrastructure construction tasks. During this period additional water column suspended sediments may impact the construction areas and it is therefore of interest to understand what the current speeds and circulation patterns are in the development area, as a result of environmental forcing from tides, waves and wind. Additionally, it is important to characterize the seafloor sediment properties and their distribution, as well as to quantify sediment suspension and transport, as a result of the bottom currents.

To this end, in this work, we perform a hydrodynamic modeling study using the coupled ROMS/SWAN model, to estimate currents and circulation in the tentative wind farm siting area, thereby referred to as the SAMP study area, with a focus on bottom stress and currents, as well as sediment processes (characteristics and suspension). We do not model the specific effects of individual wind turbine sites, or the collective effects of a wind farm, as the models used have not been developed for that purpose and are applied on meshes with grid cell sizes adequate to capture salient environmental processes, but too large to resolve wind turbine support structures.

While tidal forcing along the SAMP study area boundary can be (and is being) obtained at a reasonable resolution from tidal databases (either based directly on assimilated satellite altimetry, or from the results of a hydrodynamic model such as ADCIRC on a larger domain), and wave forcing is obtained from operational wind-wave models such as NOAA's WAVEWATCH-III, high-resolution winds are not readily available in the SAMP area, particularly in and around Block Island (Fig. 1), around which tentative wind farm sites have been selected. Such wind fields can only be obtained through atmospheric modeling at sufficient resolution. The latter is done using two different atmospheric models: (1) WRF at a very high resolution in a series of vertical (two-dimensional; 2D) sections through Block Island (Fig. 1), in order to gain insight into the key wind processes in the lee of the island where tentative sites were selected; (2) in a coarser resolution three-dimensional (3D) implementation of the RAMS model.

Hence, in section 2, we present results of the 2D-WRF wind modeling (performed in collaboration with Applied Science Associates, Inc., as part of a sub-contract), in Section 3, we summarize results of the 3D-RAMS modeling (performed as part of a subcontract to Weatherflow Inc. and analyzed and reported on in another SAMP sub-project; Spaulding et al., 2010a,b), and in Section 4, we detail the hydrodynamic ROMS/SWAN simulations (including HDROMAP tidal simulations, used for validation, and performed as part of a subcontract to Applied Science Associates, Inc., whose full report is attached in Appendix A). Finally, Section 5 provides some conclusions.

2 Fine Scale Meteorological Modeling around Block Island using WRF

2.1 Overview

This part of the work was performed in collaboration with David Stuebe and Lauren Decker at Applied Sciences Associates (ASA), who via a subcontract were tasked to perform "High Resolution Ocean Metrological Modeling in the RI SAMP Study Area" using the atmospheric: "Weather Research and Forecasting" (WRF) model, which is a Large Eddy Simulation (LES) numerical weather prediction and atmospheric simulation system designed for both research and operational applications (WRF, 2008).

At ASA, this part of the work was led by David Stuebe, who managed the project, with help from Lauren Decker, who run the majority of the model test cases (Fig. 1a) and developed the analysis methods for the results. Additionally, Prof. Steve Decker from Rutgers University, who was hired as a consultant by ASA, provided key insight on the dynamics of coastal meteorology and the application of the WRF model. Prof. Decker also did much of the research on the existing literature about compressible flow over topography.

(a) (b)

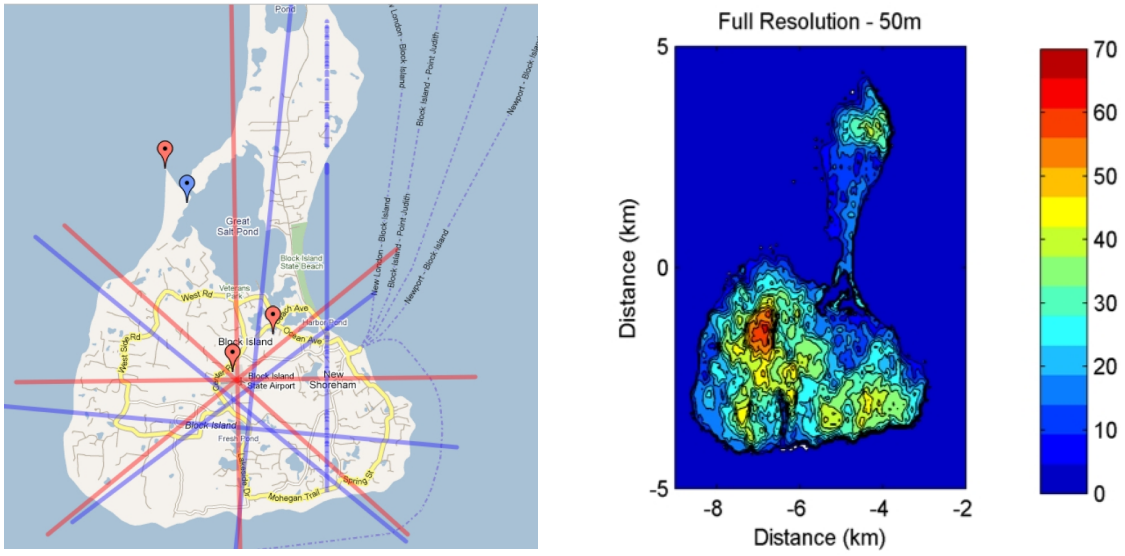

Figure 1: (a) Block Island, RI and various cross section traces where the 2D-WRF model was run; (b) Block Island topography as represented in a 50m by 50m numerical model grid.

This work initially included two main tasks:

- Implement and run the high resolution, atmospheric model WRF to answer critical questions about topographic relief effects (Fig. 1b) on the wind patterns in the lee of Block Island, where windfarm sites are being considering.
- Develop hindcast of meteorological conditions in the dynamically relevant regions of the SAMP study area, to drive a hydrodynamic circulation model and a wave model covering the region.

As work progressed, it became increasingly apparent that the computational cost of running high resolution three-dimensional (3D) simulations using WRF, to address the second task, was prohibitive. Hence, an alternative strategy was selected, which consisted in only addressing the first task using WRF, and to instead use the less demanding "Regional Atmospheric Model System" (RAMS 2010; which is also a LES model, but at more amenable coarser resolution), to address task one. To perform the latter work, ASA subcontracted Weatherflow Inc., who have an operational version of RAMS. The freed resources at ASA were re-allocated for performing an independent set of tidal simulations (since tide-induced currents represent the main forcing for sediment suspension and transport in the SAMP area), in support of the hydrodynamic studies that are also part of this SAMP sub-project.

Accordingly, the following subsections detail WRF results for task 1. Section 3 then briefly summarizes results of task 2, which has been the object of separate reports (Spaulding et al., 2010a,b). Results of ASA's tidal simulations are summarized as part of Section 4, and a full report prepared by ASA is provided in Appendix A.

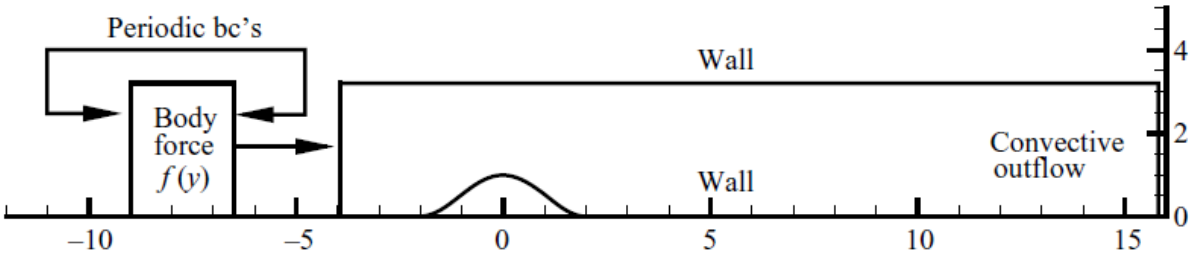

Figure 2: The numerical model WRF setup is similar to that shown in this figure from Garcia-Villalba et.al. The figure sketches the model domain and the inflow and outflow boundary conditions, as well as an idealized topographic hill. Axes are arbitrarily graduated in kilometers.

2.2 Literature Review

The bibliography relevant to the study was reviewed and findings are summarized in the following. Topographic relief affects wind flow over islands the most when:

- The hill/island is taller
- The wind speed is faster
- The ground slope is steeper (i.e., higher aspect ratio), and
- The atmospheric stability is higher (i.e., colder ocean and warmer or stratified atmosphere).

2.2.1 Large Island Wake

Previous studies have employed theory, observations, and modeling to study the effects of 3D obstacles on low-level atmospheric flow. Some of the earliest work focused on vortex streets observed in the lee of large islands. These could be monitored via satellite and are considered to be atmospheric analogues to two-dimensional (2D) (horizontal) laboratory flows around cylinders. Thomson and Gower (1977) exemplify this approach to studying wind perturbations induced by large islands. In their case, they used satellite observations of cloud patterns in the wake of the Aleutian Islands to calculate fluid dynamical quantities such as Reynolds and Strouhal numbers. The emphasis is on explaining the cloud patterns in terms of what is observed in the laboratory. Note that the islands studied here have elevations in excess of 1,000 m (as opposed to Block Island, which is 64 m high). Smith and Grubišic (1993) study a similar wake in the lee of the island of Hawaii (elevation over 4,000 m) using a research aircraft. They found counter-rotating vortices and associated shear lines in Hawaii's wake. Due to Hawaii's position in the trade wind regime, these flows are quasi-steady. Incidentally, it was Captain Cook's encounter with the wake of Hawaii that likely damaged his ship, forcing him to return to the island, where he was subsequently killed by the natives. As later studies make it explicit, the large size of Hawaii and the Aleutians forces the air to go primarily around the island, producing notable vortices in their wake. Smaller obstructions behave differently.

A smaller island (St. Vincent, maximum height around 1,000 m) was studied by Smith et al. (1997) to examine the effects of relatively small islands on the flow. St. Vincent generates what is called a “weak wake” (in contrast to Hawaii or the Aleutians) because, although vorticity is generated by the interaction with the island, the wind does not “close off” into eddies (i.e., vortices). In other words, vorticity is present in the wake, but not a closed circulation. This study summarizes previous theoretical work with a discussion of four different types of wakes, depending on the parameter regime. The key parameter is h/h_c (the ratio of maximum obstruction height to the critical height for (atmospheric) wave breaking). If that quantity is less than one, no

wake should be observed. A value between one and two represents a weak wake, and larger values produce strong wakes (e.g., Hawaii). The critical height for wave breaking, h_c, is highly dependent on the shape of the obstruction, the wind speed, and the stability of the atmosphere. If the obstruction has a *Witch of Agnesi* shape (sort of like a Gaussian bump; Fig. 2), wave breaking (and thus a wake) would occur if the non-dimensional terrain height: hN/U is greater than 0.85, where N is the Brunt-Vaisala frequency, and U is wind speed. Thus, the higher the wind speed, the more stable the atmosphere, and the higher the height of the obstruction, the more likely a wake will be produced. For the case of St. Vincent, wakes were observed to extend over 300 km in the lee. To see if these long wakes could be modeled, a highly idealized (inviscid, no surface fluxes, no surface friction, smoothed topography) 3D atmospheric model (not all that different from the WRF Model in its overall construction) was run on a grid with 2 km mesh spacing and 60 vertical levels extending from the surface to 6 km. Their model reached a steady state after about 12 hours of simulation. After varying a host of parameters, they concluded that the effect of the turbulence parameterization was nontrivial, suggesting much finer resolution may be necessary to generate a simulation of high fidelity (since more of the turbulence can be explicitly resolved).

Lane et al. (2006) performed a similar study to model the wake of Kauai, where the non-dimensional height on the day of interest was about 1.67. Once again, a classic wake was successfully simulated using mesh sizes: Δx = 167 m and Δz = 50 m. Kauai is 1,600 m tall.

2.2.2 Small Hills

Much smaller obstacles to the flow (primarily hills), similar to the situation in Block Island, where the maximum elevation is about 70 m (Fig. 1b), have been modeled in a variety of ways. Apsley and Castro (1997) took a highly idealized approach, using an incompressible model (known as the SWIFT model) to simulate flow around Cinder Cone Butte, a 100 m high hill rising above flat terrain. In their run, the atmosphere was set to be highly stable, and as a result, streamlines flowed around the hill below about 20 m, but over the hill at heights above that. [Thus, 20 m is the height of the theoretical *dividing streamline* for this case.] The SWIFT model solves for the steady-state flow only, but because of the computational cost of even this highly simplified model, they did not attempt to demonstrate grid convergence (i.e., that the results are insensitive to grid spacing) for their Cinder Cone Butte run.

In an idealized Large-Eddy Simulation (LES) study, Ding and Street (2003) simulated the flow in the wake of a 3D hill that had a shape similar to a Gaussian bump. Again, the factor

U/Nh was deemed important. When that number is much less than one, then flow around the hill is expected (just like 2D laboratory flow around cylinders). Values closer to one are expected to result in more flow over the hill. However, in either case, counter-rotating vortices are expected in the wake. Additionally, the wake is expected to approach steady state when *Ut/h* is around 25. Because running LES on the real-world scale is so computationally expensive, the domain size used in Ding and Street's work was laboratory scale: 2 m x 1.5 m x 0.8 m, with a hill height of 10 cm, using 194 x 98 x 130 grid points. They found the width of the wake decreased as *U/Nh* increased.

Relating the latter work to Block Island, we should expect to see flow around the island produce a wide wake when the flow is slow and stable. Flow over the island producing a narrow wake is expected during fast-moving neutral flow (most likely in fall/early winter).

Garcia-Villalba et al. (2009) also use LES models to simulate flows on laboratory scales, although their results may have more relevance to designers of wind turbines rather than those trying to determine where to put the turbines.

2.2.3 Askervein Hill

A number of studies have used observations from a field campaign at Askervein Hill (~150 m tall and 1 km wide; in Scotland) to improve their model simulations of flows in complex terrain. These models tend to be one of two types: (1) Reynolds-averaged Navier-Stokes (RANS) solvers; or (2) LES. RANS models solve for the steady-state flow, while LES models attempt to capture the time-dependent turbulent nature of the flow; thus LES model solutions are inherently unsteady. Additionally, the LES approach does not rely on an assumed eddy viscosity. Walmsley and Taylor (1996) provide an early review of this work. It is important to note that most studies involving Askervein Hill examine the flow on the hill and perhaps up to a kilometer or two in the lee. This is closer to the obstruction than the proposed Block Island wind farm.

Eidsvik (2005) notes that the wind power available to windmills varies by a factor of one over flat topography (owing to variations in surface roughness), but by a factor of five in mountainous terrain, and then uses the RANS approach to see how well the flow around Askervein Hill can be modeled in this wind energy context. Their model (SIMRA) matches the observations within 50%, considered to be within the range of the observational errors, showing that confidence can be placed in models to generate fields of wind energy availability on small scales. The SIMRA model used 100 m grid spacing in the horizontal, with 1 m grid spacing in the vertical near the surface. The Coriolis force was ignored, and the flow was assumed to be adiabatic (including no surface heat flux). Eidsvik (2005) mentions that slopes (*H/L*) greater than 0.5 can lead to

separated flow in the lee (i.e., the wind in the direction of the large-scale flow becomes negative) for neutral stratification. Additionally, the following scaling are provided:

$$\frac{l_z}{z_0}\ln^2\left(\frac{l_z}{z_0}\right) \approx 2\kappa^2\frac{L}{z_0} \quad ; \quad \frac{\Delta u(l_z)}{u_0(l_z)} \approx 1.8\frac{H}{L} \quad ; \quad \frac{\Delta K}{K_0} \approx 2\frac{\Delta u}{u_0} \tag{1}$$

Despite the apparent success, Eidsvik (2005) concludes with the following caution: "...any estimation of actual stratified flows in mountainous terrain will probably be associated with significant uncertainty."

Prospathopoulos and Voutsinas (2006) provide an overview of the RANS approach and use it to model the Askervein Hill flow. They perform a number of sensitivity tests (varying vertical and horizontal resolution, the size of the grid, the surface roughness, etc.) to assess the impact the various "tuning knobs" have on their steady-state solution. With appropriate settings, they generate reasonable results. It is interesting to note that they mention problems getting the flow in the lee of the hill correct, but then state that it is an inappropriate location for wind energy applications, so it is irrelevant. [For the Askervein Hill case, it is the speedup region at the top of the hill that is most important for wind energy.] The Askervein Hill is only a few kilometers wide, though, so the "lee of the hill" in their paper just means within a kilometer or two of the summit. Any wake extending further downstream is ignored.

Silva Lopes et al. (2007) used an LES model to simulate the flow over Askervein Hill, and found an improvement relative to the RANS approach on the upwind side, but continued difficulty on the downwind side, including the lack of grid convergence.

Chow and Street (2009) also used the LES approach, describing the situation thusly: "The development of accurate wind energy prediction models for flow over complex terrain has been notoriously difficult as a result of the representation of steep topography, unsteadiness in the flow, poor performance of turbulence models, and lack of adequate field data for validation, among other factors." In their study, Chow and Street focus on improving the modeling of turbulence, using the ARPS model. [ARPS, RAMS, and WRF are the three "standard" Numerical Weather Prediction models in use, at least in this country, and broadly speaking they all are constructed in a similar fashion.] Their run uses 35 m grid spacing in the horizontal and 5 m grid spacing in the vertical at the lowest layer, stretching above that to give 59 layers in their 700-m-deep model domain. They note, this is a coarser vertical resolution than other Askervein Hill studies have used, but state that "finer resolution is not practical for real atmospheric flows over complex terrain." They also emphasize the need to have a suitable aspect ratio between Δx

and Δz in LES modeling. No surface heat or moisture fluxes are allowed, and their run encompassed a day with neutral stability. To force their model, they first ran an identical simulation over a domain with no topography to allow a fully turbulent flow to spin up. The outflow from this run then served as the inflow to their run with topography. An attempted run with uniform inflow did not produce adequate results. Their runs matched the observations well, with a slight reduction in the wind speed on the windward side of the hill, a significant speedup at the summit, and a significant slowdown (about 70% slower) in the lee at 10 m above the ground.

2.2.4 Other Relevant Work

Perhaps the island closest to Block Island in size that has been studied is Nauru, in the tropical Pacific. Nauru is about 5 km x 5 km in size, with a maximum elevation of 71 m, situated in the trade winds where easterlies of 5 to 10 m/s are common. In an observational study, Matthews et al. (2007) attempt to understand how the island generates a plume of cumulus clouds extending up to 200 km in its lee. [Malkus and Bunker (1952) report a less extensive wake (30 km) in the lee of Nantucket.] The physical process producing these plumes is the strong surface flux of sensible heat, which generates a warm plume that results in cumulus clouds at altitudes around 750 m to 1 km. The length of the cloud plume was likely maintained by horizontal convective rolls formed in part by the topographic obstruction. It was found that this warm plume detached from the surface about 20 km in the lee of the island. To the extent that Block Island is similar, we could expect impacts to be felt that far in the lee near the surface in our case as well.

Removing topography from consideration, the understanding and modeling of flows in the boundary layer depends on knowledge of the surface roughness, and the ways in which these flows evolve can be dependent on the wind profile. Fedorovich et al. (2001) present an LES modeling study that examines the effect these two factors have on the flow. They show that rougher surfaces and negative shear (wind speed decrease with height above the boundary layer) increases the depth of the boundary layer when stratified flow is heated from below. This could have applications to understanding flow patterns around Block Island during the fall season, with the added complications of topography of course.

Moeng et al. (2007) document the first use of the WRF model as a LES. After making a few modifications (included in the latest versions of the WRF 2008 model), they obtained good results with their idealized experiments. Their validation consisted of comparing their results to observations, laboratory studies, and other LES results.

Shaw et al. (2009) briefly review the state of the science, highlighting the problems that exist with modeling the turbulent mixing that leads to the actual winds and shears experienced by the turbines. The surface and boundary layers, according to Shaw et al., are still poorly understood, with limited observations being one of the problems. They suggest the LES approach may be a way to bridge the gap.

2.3 Numerical Modeling Approach

2.3.1 Overview

In task 1 of the fine scale meteorological modeling work, reported here, we simulate at high resolution the effects Block Island (BI) has on the turbulent atmospheric flow, under a variety of conditions (e.g., atmospheric stability, wind speed and direction). We focus the analysis of results, particularly on the island's lee side.

For performing high-resolution atmospheric simulations, we use the WRF model in Large Eddy Simulation (LES) mode (WRF 2008). A schematic of the model setup around BI is shown in Fig. 2. In three-dimensions (3D), this approach was found very computationally demanding, so to generate more runs in a given amount of time, 2D runs were first carried out for a series of vertical cross-sections through BI (Fig. 1a). These were followed by a small number of 3D WRF simulations. Although it is expected that the 2D runs may miss critical aspects of the flow, these were deemed good enough for identifying parameters yielding important patterns and phenomena. In the end, comparing the 2D and 3D WRF runs will determine how useful the 2D runs might be. [Note, as explained in the introduction, in view of the demands of running high resolutions 3D WRF simulations, an alternate strategy was selected, consisting in switching to the less computationally demanding RAMS model for performing most of the subsequent 3D simulations in and around BI.]

The LES approach generates inherently unsteady flows (i.e., no steady state is or can be reached in simulations), but this should allow for important quantities for the wind turbines, such as variance in vertical wind shear, to be assessed. LES of a steady turbulent boundary layer, for instance, will only result in a steady state result from a statistical point of view, similar to an actual experiment.

2.3.2 The WRF Model

The Advanced Research WRF (Weather Research Forecast) model is a collaborative effort between multiple federal agencies and universities, to develop a new generation of numerical

weather prediction tools. The model solves the fully compressible Euler equations for non-hydrostatic fluid motion with conservation of all scalar quantities using a 4th order Runge-Kutta integration scheme. The model prognostic variables include momentum and fluid density due to temperature and water vapor. The model uses a sigma, terrain following, pressure coordinate in the vertical. The top of the model is a constant pressure surface, which has no friction and no flux. There is a damping term for vertically propagating gravity waves to prevent artificial reflection. In the horizontal direction, the model uses an Arakawa C-grid discretization. The lateral boundaries used in the model are open (gravity wave radiating), periodic, or specified.

The bottom boundary of the 2D simulations (Fig. 2) uses physical parameterization of surface roughness to estimate shear stress at the no flux boundary. All of the subgrid scale physics options for the surface boundary layer are turned off (i.e., we are attempting to perform direct Navier-Stokes simulations). Unlike a true direct numerical simulation of the Navier-Stokes equations, the smallest turbulent length scales are not resolved, but often at very high Reynolds numbers (where the flow is nearly Reynolds number independent), the subgrid scale physics are not overly dependent on the eddy viscosity. The models run for this project are LESs, which directly resolve the unsteady turbulent flow over the topography of BI. This differentiates this model from other high resolution models, which may use a Reynolds Average or other parameterizations for the turbulent flow (e.g., as will be the case for RAMS simulations).

2.3.3 Development of the Block Island 2D Cross Section Atmospheric Modeling

The WRF model has been adapted from existing idealized 2D simulations for use in studying the flow over BI, in a series of 2D cross-sections (Fig. 1a). Based on an idealized test case of flow over a hill (e.g., Fig. 2), the model setup and initial conditions have been adapted to use the real topography of Block Island (Fig. 1b). Similar to the hill case in Fig. 2, the boundary condition normal to the flow is periodic. The most difficult aspect of this semi-idealized 2D implementation of the model has been the correct expression of the upstream boundary condition. To do so, we experimented with various options for open, periodic and specified boundary conditions, using a range of techniques to relax model results to the desired value, such as nudging and sponge layers. Our experiments showed that the open boundary does not react in a dynamically consistent way when using a specified condition for only velocity and temperature. It is thus critical to specify all of the prognostic variables inside the domain so that the model will adjust in a dynamically consistent way.

2.4 Two-dimensional Idealized WRF Simulations

The idealized 2D simulations in vertical cross-sections (Fig. 1a) use a 25 m horizontal grid resolution. To meet the assumptions of the numerical methods and the physical dynamics of the model, the vertical to horizontal aspect ratio $\Delta z/\Delta x$ must be nearly 1 to 1, so the vertical grid resolution is selected here at 20 m. Figure 3 shows the horizontal grid resolution over Block Island (the vertical grid is omitted for readability). A sensitivity analysis to the grid resolution does suggest, however, that the model is not fully resolved. Selected model runs at 10 m resolution have a more developed boundary layer, but preliminary results suggest that there is little difference in the overall wind profile or the effect of the island when using such a small grid. Hence, simulations are performed using the 25 x 20 m grid.

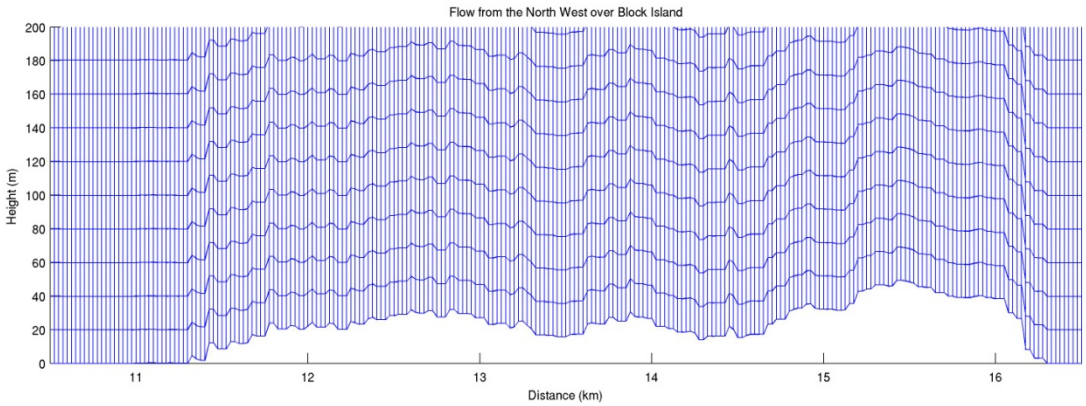

Figure 3: The region of the model grid over Block Island showing the vertical and horizontal resolution.

2.4.1 Ocean Boundary Layer Experiments

Initial experiments have run the 2D micro-scale model, with no topography, to determine the boundary layer thickness in the absence of the island, under the following conditions:

*Wind Speed***:** 5, 10 m/s

*Atmospheric Stability***:** stable, neutral, unstable as determined by the air-sea temperature difference (a colder ocean than the atmosphere yields a more stable atmosphere than a warmer ocean).

Results from these initial experiments, which are aimed at assessing model parameterization and setting open ocean boundary conditions, are not reported here in details. Results of these experiments are then used to specify the inflow boundary condition for the simulation cases examining flow over the BI topography.

Figure 4, for instance, shows the simulated wind speed (horizontal component) in a typical model run for a NW wind of free stream velocity of 10 m/s in a neutral atmosphere. The figure shows instantaneous contours of constant velocity along the length of the model domain, for 166 and 496 min into the simulation, which illustrate the convergence of the (mean) wind speed. We observe that the velocity increases with height and the atmospheric shear increases over the island. These results are characteristic of our initial work, though the issues with the inflow boundary condition make comparison between the upstream and downstream of the flow impossible. These issues have later been resolved as discussed above.

To aid in comparing the flow across the BI topography shown in Fig. 4, we created profiles at different points in the domain as shown in Fig. 5 (from results of Fig. 4b). Such an analysis is critical in determining the effects of the island, once the upstream boundary conditions are properly set, for a specified atmospheric stability. [Note, results shown in Fig. 5 are for a case with a slightly lower resolution of 50 m, used in developing the boundary condition.]

2.4.2 Island Cross Section Experiments

Based on the steady state approximation of the Ocean Boundary Layer experiments reported above, the upstream boundary is set to force an idealized wind field approaching BI from various different directions, wind speeds, and stabilities. For these cases, the island topography and surface roughness have been extracted from the USGS land surface model. Below are the various cases that were simulated using WRF in 2D vertical cross-sections through BI (Fig. 1a):

Direction: 4 compass points (SW,W,NW, N)

Wind Speed: 5, 10 m/s

Atmospheric Stability: Stable, Neutral, Unstable

(a)

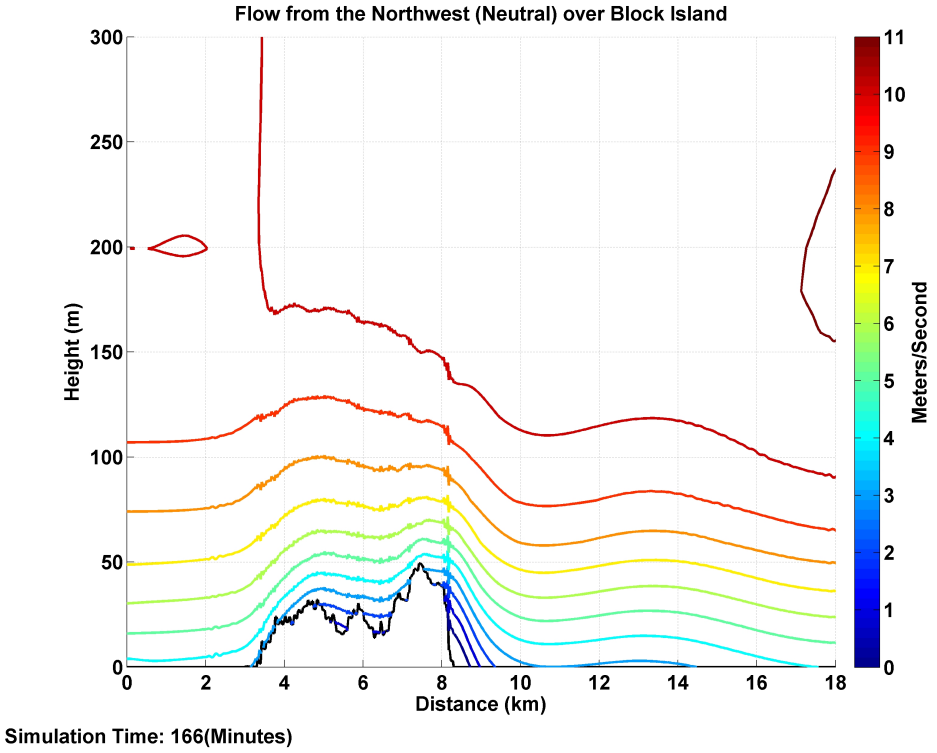

(b)

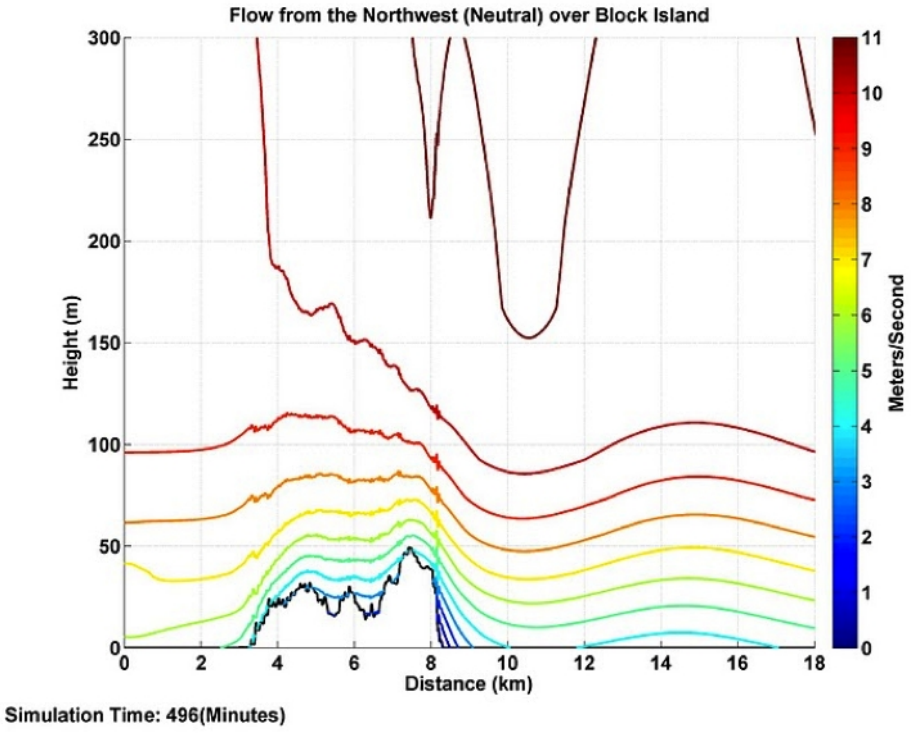

Figure 4: Instantaneous velocity contours for typical neutral NW flow (10 m/s in free stream) over Block Island, at two different simulation times: (a) 166 min; (b) 496 min.

All these results are plotted into figures such as Fig. 4, for velocity components, pressure and temperature (not shown here but available on demand). Based on such simulations, meaningful results for windfarm siting are extracted in the form of horizontal velocity for various stability conditions, as a function of the distance from BI, at selected heights (e.g., 80 and 130 m for approximate extension of windmill airfoils). Figure 6 shows an example of such results obtained from three different simulations. Clearly the marked difference in speed between 80 and 130 m would induce significant shear in the windmill airfoils.

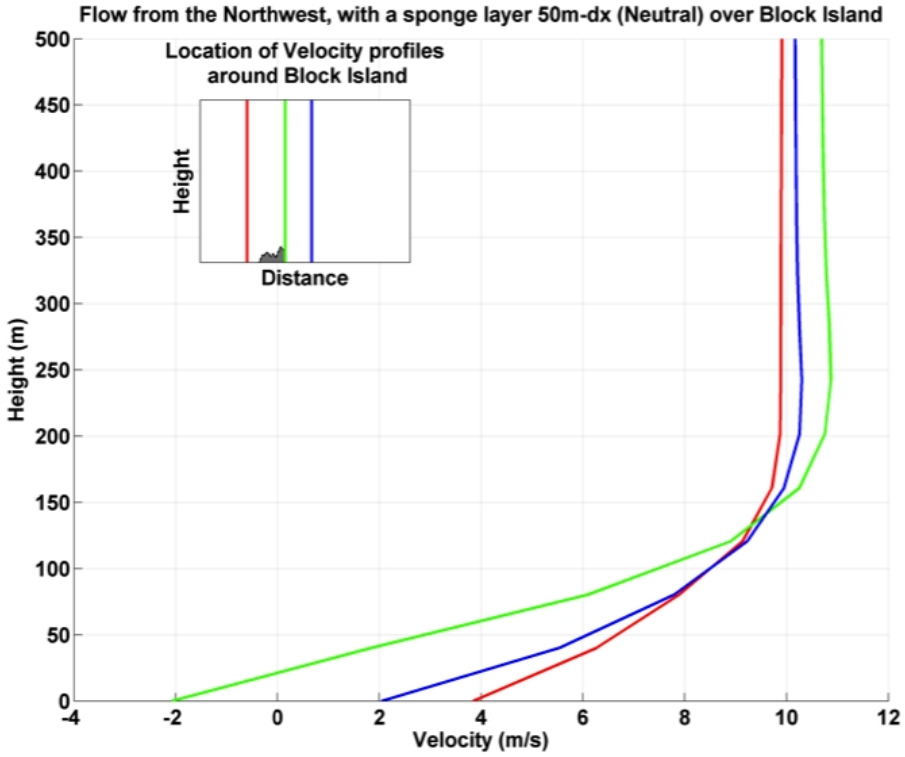

Figure 5: Profiles of horizontal velocity from Fig. 4b results, at different location along the length of the model domain shown in inserted figure.

Figures such as Fig. 6 are available for all tested wind directions and speed, and allow for direct comparison of the impact of air-sea stability on the dynamics of the model and wind speed as a function of distance and height in the lee of the island.

2.4.3 Validation and Verification

To validate the 2D simulation approach illustrated above, a limited number of 3D model experiments were performed, using the same physical parameters as for 2D simulations (e.g., Figs. 4-6). It was initially planned to perform a systematic comparison of 2D and 3D results, by

(a)

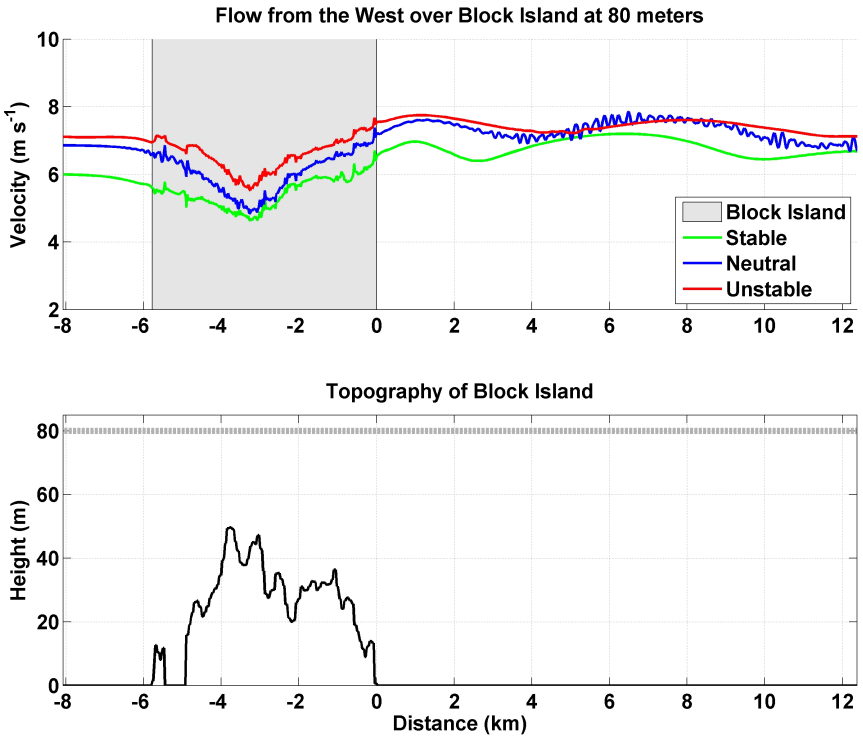

(b)

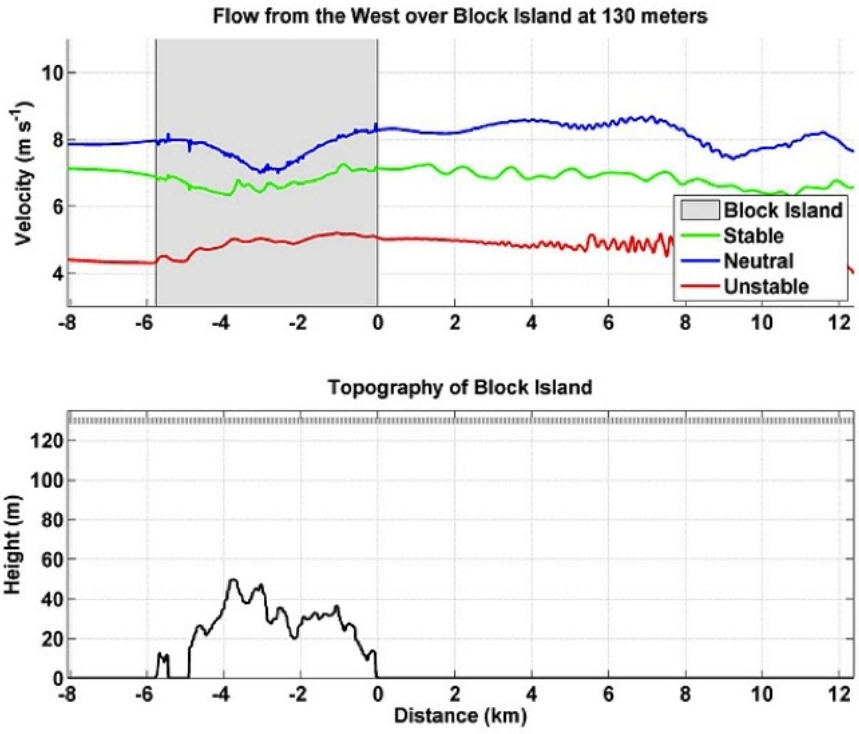

Figure 6: Comparison of horizontal wind speed at two heights : (a) 80 m; (b) 130 m, due to Westerly wind flows (10 m/s free stream velocity), and different atmospheric stability conditions.

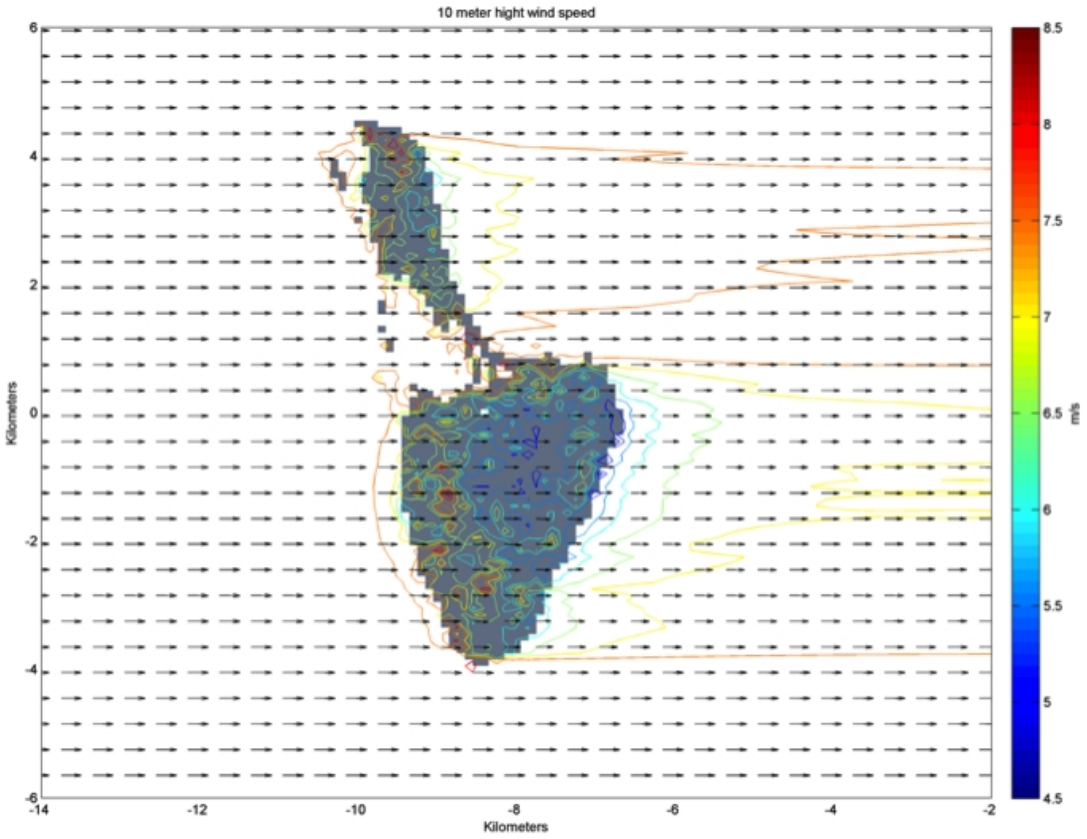

Figure 7: Wind Speed at 10 m high over Block Island, from 3D WRF model simulations for an idealized flow from the West.

extracting 2D section data from 3D results, for comparison with the 2D simulations. Additionally, it was planned to examine the overall magnitude of the turbulent cross-stream flow.

A typical result of 3D WRF simulations is shown in Fig. 7, for a westerly flow (10 m/s free stream velocity) at 10 m elevation over BI. Such results show there is little cross-stream flow, which is consistent with the assumptions of the 2D model approach.

At this stage in view of the high computational cost of running sufficiently resolved 3D WRF simulations, it was decided to change strategy and instead use the regional model RAMS, to perform the 3D simulations of wind over BI on a series of 4 nested grids, the finer and smaller one having a 500 m horizontal resolution (which is to be contrasted with the 25-50 m horizontal and vertical resolution used in the WRF simulations discussed above), and a 20 m vertical resolution in the lower layers (geometrically increased with elevation). This work was performed by another subcontractor, Weatherflow Inc. and results are reported on and analyzed in separate reports by Spaulding et al., 2010a,b. Section 3 of this report gives a brief summary of this work.

3. Regional Meteorological Modeling around Block Island using RAMS

Below is a summary of this work, which is separately reported on in Spaulding et al., 2010a,b. Results of RAMS, in the form of wind field and induced surface shear, are used to force the ROMS/SWAN simulations reported on in Section 4 of this report, over the period 10/1/09 to 2/28/10. On example of 3D RAMS's results obtained in the fourth and finest nested grid is given in Fig. 8, hindcast for the actual situation on 8/5/09; the figure shows wind velocity (magnitude and direction; contour lines) in and around BI at 84 m elevation. Due to BI's topographic relief effects (Fig. 1b), to large size vortex-like structures in wind speed can be seen on the NE and S sides of the island.

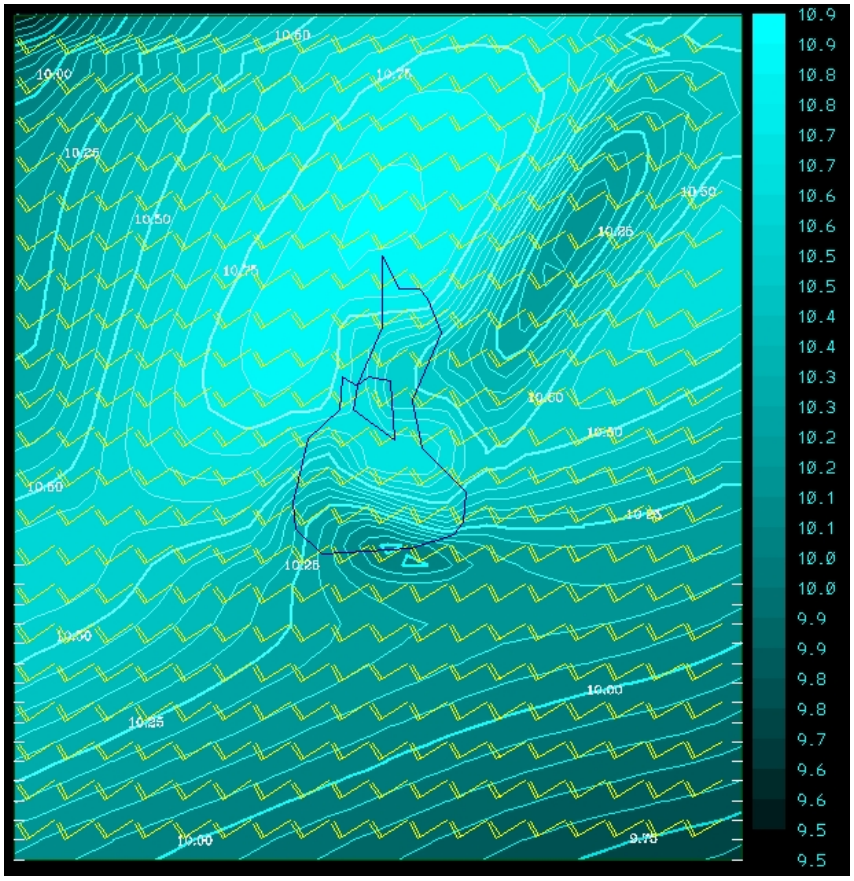

Figure 8: Wind at 84 m high over Block Island, from 3D RAMS model simulations for the hindcast flow on 8/5/09 (speed in m/s, directional symbols). BI is marked by a thin blue line.

3.1. Abstract of Spaulding et al., 2010a

Hindcast simulations of the winds in the vicinity of Block Island were performed using the Regional Atmospheric Modeling System, RAMS, V6, from October 1, 2009 to February 28, 2010 to assist in evaluating various sites south of Block Island for a small wind farm. This period

was selected since wind and air temperature observations were available from an offshore buoy (4 m elevation) immediately south (4.5 km) of the island and from a meteorological tower (9.9, 32, 47.6 and 57.4 m elevations) near the center, west coast of the island. The model was implemented in a four level nested system with grid resolutions of 12, 6, 2, and 0.5 km. The model was driven by NAM 12 km analyses. The model employed a 20 m vertical grid resolution at the surface, that geometrically increased with elevation. Island land cover and topography and sea surface temperature were provided by national digital data bases.

The winds during this period were predominantly from the NW, with the next most frequent direction from the NE. The wind distribution is typical of winter winds in the area, but with enhanced winds from the NE. The meteorological tower observations showed very low shear coefficients, 0.7 to 0.9, during the simulation period, typical of neutral to unstable, winter winds.

Model simulations were compared to meteorological tower observations at 57 m on shore of Block Island and showed good agreement with the data, with similar trends for passing weather events. The observed mean speed was 9.73 m/sec and the RAMS predicted was 9.3 m/sec (5.1% difference). The wind power followed a similar trend, 1000 kW/m^2 observed and 838 kW/m^2 RAMS (16.2% difference). The model predicted shear was higher than meteorological tower observations. The predicted shear coefficients increased dramatically over the island, reaching values as high as 0.45 over the southern end of the island where vegetative cover is dense. Model predictions also show lee effects from the topography/land cover at the southern end of the island (mean elevation of 35 m) for the two predominant wind directions. Lee effects were clearly noted 8 km from the island. Model predictions were also compared to winds (10 m elevation) from an offshore buoy and again showed good agreement (observed - 8.54 m/sec vs RAMS- 8.32 m/sec).

Simulations were performed for the dominant NW wind case to assess the sensitivity of the model to how the island was represented: by both its topography and land cover, or by each separately. The model predictions showed that either topography or land cover contributed substantially to lee effects.

Model predictions were integrated over the simulation period to estimate mean wind speeds and average power at 80 m. The mean wind speed and power contour lines are parallel to the BI shoreline. Wind speeds decrease from 10.2 m/sec south of Block Island to 9.7 m/sec at the northern end of the island. Power decreases from 1150 kW/m^2 to 965 kW/m^2 over the same distance. Power estimates were made at three potential locations for a small wind farm (5 to 8

turbines), SE, S and SW of the island following the state water boundary line (5 km) from the island. Mean powers were predicted to be SE—1,097 kW/m^2, S—1139 kW/m^2, and SW—1,076 kW/m^2. The S site has the highest power production potential; 3.6 to 5.4 % higher than the other two sites. The difference between the sites is due to lee effects from the island for NW winds at the SE site and for NE winds at the SW site. The SW site, in addition, is the lee of eastern end of Long Island (Montauk Point) for westerly winds. Lee effects at the S site are minimal since winds from the N are rare. Simulations have not been performed for spring and summer months where SW winds dominant. Winds from this direction are likely to be comparable at all three sites, since there is no lee effect and the locations are quite close. There is some degradation of winds from the W due however to lee effects from Long Island and an increase to the SW of the island due to channel enhancements for southerly winds.

Simulations, using a template based method, were performed using the observed wind rose at the AWS Met site and model predicted wind fields for eight compass directions. Predicted mean wind speeds and power densities were in generally good agreement with the hindcasts. The differences could be explained in part by the model predicting lower frequency for the NW winds and higher frequency for W winds than observed. When the model predicted wind rose at the AWS Met was used the predictive performance improved measurably.

3.2. Abstract of Spaulding et al., 2010b

The focus of the paper is to assess the wind resources for the area in state waters (4.5 km from land) immediately south of Block Island, a small, 9 km by 6 km, low relief (35 m elevation) pear shaped island located 15 km off the coast of RI, for the siting of a small (5 to 8 turbine) wind farm. The area is being considered for designation as the potential site for offshore wind development. A review of existing wind observations was performed and showed that the wind speed and power density roses were dominated by westerly winds with NW dominant in the winter and SW in the summer. Wind shear measurements from meteorological tower observations on the island showed low shears in the winter during unstable atmospheric conditions and higher values during the stable summer winds. The shears were also strongly impacted by the Block Island land cover and the positioning of the observation tower relative to these features.

A template based scaling method was used to estimate the annual mean wind speed and power density distribution in the vicinity of the southern end of the island. Hindcast simulations were performed using a four level nested version of RAMS for eight points of the compass for selected time periods over the last two years. These model predictions were compared to observations at two locations on the island and showed good agreement for direction and temporal trends of the speed but consistently under predicted the speed. The results of the simulations were used in conjunction with a wind speed frequency rose in the study area and, assuming linear speed scaling, estimates were made for the annual mean values. The large scale patterns showed wind speeds and power increasing with distance offshore. This pattern was modified in the vicinity of the island by lee effects from the predominant and strong NW winds. The impacted area extended at least 8 km to the SE of the island. Areas to the W-WSW of the island were impacted by lee effects from NE winds and roughness effects from Long Island, immediately to the west. Predictions showed the highest annual mean wind speeds and power densities to the S of the island with sites to the SW and SE having lower values. Power production potential was estimated for three sites: SE, S and SW of island. Wind power at the S site was 4.9 % and 6.9 % greater than the SW and SE sites, respectively.

Three separate wake models were applied to the SE and S sites to assess the impact of turbine layout. The SW site was not viable for a farm because of seabed geology making installation of pile foundations challenging. The turbines were nominally spaced 1 km apart. Simulations were performed for each wind direction and showed wake losses as high as 14 %, when the wind was in alignment with the field. When weighted by data from a nearby wind rose, the annual losses were shown to be several percent at the SE site and about half of that at the S site. The difference is due to the fact that SW winds are dominant in the summer while W winds are less frequent.

Considering both lee effects from the island and wake effects, the S site is the preferred location for a small wind farm.

4. Hydrodynamic, Wave, and Sediment Process Modeling using ROMS/SWAN

4.1 Introduction

The goal of this task is to characterize hydrodynamic flows in the ocean in the SAMP area (Fig. 9), due to general circulation currents, tides, waves and wind-driven circulation. Based on these and a data-basis of seafloor sediment characteristics, one also aims at characterizing near bottom sediment processes (namely suspension and transport). Understanding sediment suspension induced by currents resulting from combined environmental processes is important to the ocean SAMP ecological work, because a significant change in suspended sediment can have a detrimental effect on benthic life. Such a study should be conducted prior to any large-scale wind farm installation, in order to characterize suspended sediment processes in the areas envisioned for wind farm development.

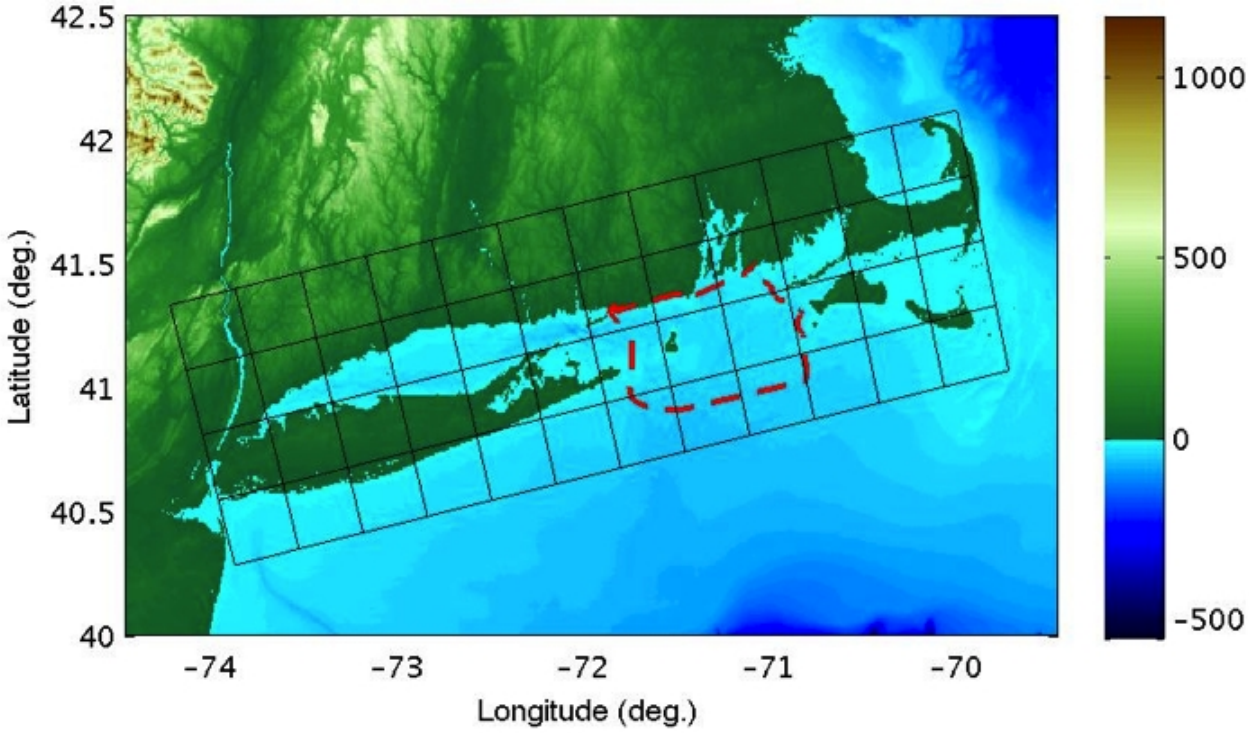

Figure 9: Overview map of bathymetry and topography around the SAMP study area, showing the ROMS model domain (black grid; each square is 30 km across, corresponding to 50x50 gridpoints in the high resolution simulations) and the SAMP study area (dashed; red).

Accordingly, this task included:

- Applying high resolution hydrodynamic and wave models to SAMP study area (Fig. 9) to investigate details of spatial and temporal structures of current and wave fields.

- Developing a characterization of the spatial and temporal variability of the current (tide-, wind-, and wave-driven).
- Estimating the potential for sediment suspension under wave and current forcing in the SAMP study area.

Note that this work does not investigate changes to overall sediment transport around Block Island due to wind farm support structures, since these are at much smaller scales than that of the model grids used in this work. Hence, we do not attempt to characterize scour around the windmill support structures; besides scour around coastal structure is a complex, specific, and still active area of research (see e.g., Sumer et al. 2001), which is outside the scope of the SAMP work. What is known is that wind turbine installations usually consist of several vertical piles, the presence of which can increase suspended sediment by eroding sediment around the pile circumference (Laursen 1963). This process is initiated by the formation of a horseshoe vortex and the contraction of streamlines (Sumer and Fredsoe 2001).

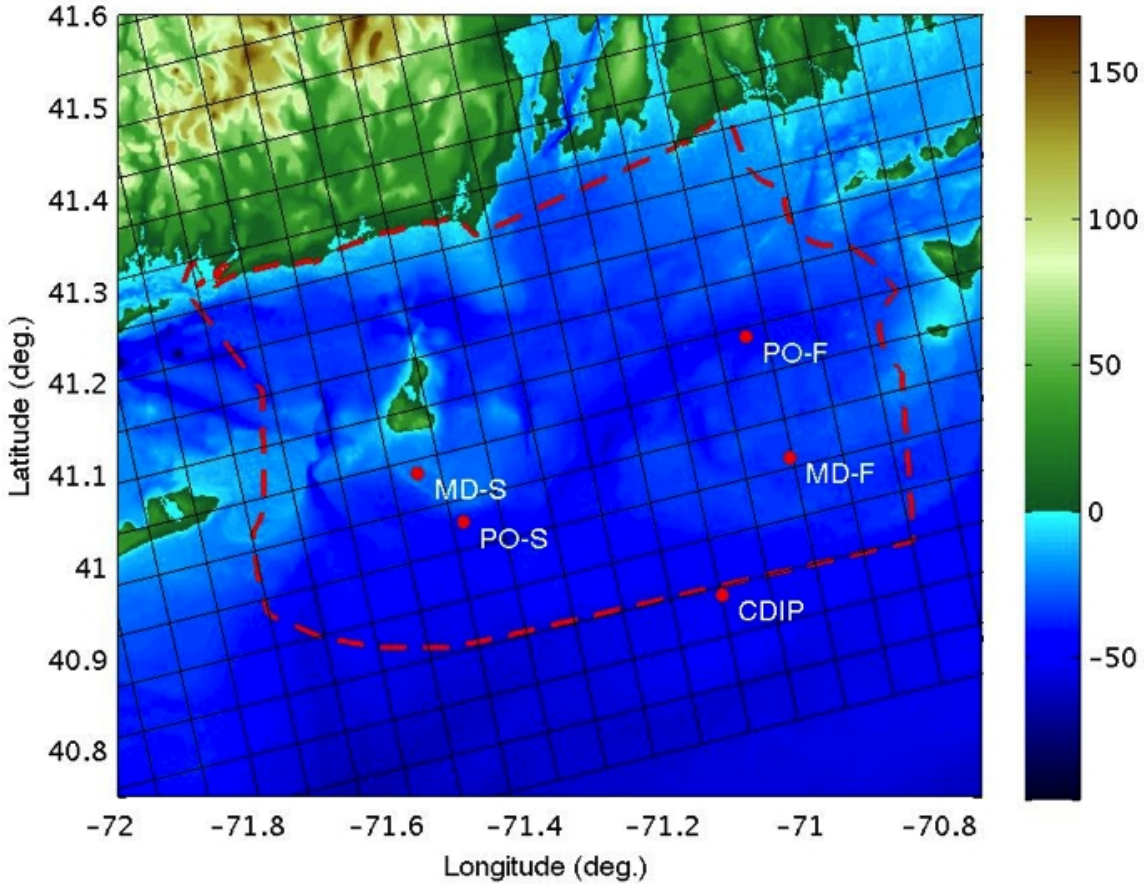

Figure 10: Overview map of bathymetry and topography around the bounds of the SAMP study area (marked by dashed red contour) and domain (black grid; each square is 6 km across, corresponding to 10x10 grid points in the high resolution ROMS/SWAN simulations). White labels show locations where wave and current data was recorded (Table 1).

There are little to no pre-existing measurements of suspended sediments in the SAMP area, but meaningful predictions can be made based on a properly validated regional hydrodynamic model of the area, which is the goal of this work. Sediment suspension is dependent on near-bottom currents, which in the SAMP study area are primarily tidally driven, except during episodes of storm waves (characterized by long, long-crested swells whose induced particle velocity may cause significantly shear on the seafloor). Except during those episodes, subsurface currents generated by winds and waves in the area, and density-driven circulation are relatively weak in comparison to tides, although observations of tidal currents have noted significant seasonal changes in tidal current ellipses (Codiga and Rear 2004).

4.2 Literature Review

A variety of ocean models have recently been used to study hydrodynamics in the area around our SAMP study area (Fig. 1), although none have focused on the waters immediately around Block Island as we seek (e.g., Oey et al., 1995; Edwards et al., 2004; He and Wilkin, 2006; and Mau et al., 2006). In each case, a spin-up time of 15-30 days is used to achieve quasi-periodic model results, which are then compared to observational data. Emery and Thompson (2001) showed that 30 days is sufficient to resolve the 5 major tidal constituents.

Edwards et al. (2004) used the MIT general circulation model (Marshall et al., 1997) to study front generation in BI Sound (BIS). Importantly, although they focused their attention on BIS, their domain extended over the entire length of Long Island Sound, which can experience tidal velocities of over 1 m/s because of a resonance with the period of the M2 component of the tides. Edwards et al. favorably compared their results against ADCP data from the FRONT project (Codiga and Houk, 2002).

He and Wilkin (2006) used the Regional Ocean Modeling System (ROMS; see Shchepetkin and McWilliams, 2005), as we are doing in the present work, to study the tidal dynamics south of Cape Cod, Massachusetts, to the east of our study area (Fig. 1). They specifically focused on tidal gage and bottom pressure measurements, because their domain of interest extended over the New England Shelf where Shearman and Lentz (2004) had previously found that internal waves can have a strong effect on velocity measurements. He and Wilkin were able to find good agreement with measurements. Note that they used a hybrid data assimilation modeling system

that used TRUXTON (see Lynch et al., 1998) as an inverse model to correct the tidal open boundary conditions.

Mau et al. (2006) used the Princeton Ocean Model (Blumberg, 1987) to simulate the semidiurnal tidal currents slightly to the west of our study area. They compared their results against an atlas of tidal current and bottom pressure (Moody et al., 1984), HF radar measurements of surface currents (Ullman and Codiga, 2004), as well as ADCP profiles (Codiga and Houk, 2002), of the New York Bight and BIS. Mau et al. found that the model reproduces the correct flow patterns and vertical structure, which earlier one-dimensional models of the tides in the area could not (see Codiga and Aurin 2007). They claim that such model results for the barotropic tidal currents are as accurate as observations.

Readers are referred to Codiga and Ullman (2010) for a more complete review of the physical oceanography of the SAMP study area. They review satellite measurements, recorded CTD casts, surface currents measured by HF radar, and output from a hydrodynamic model of the region on a large scale. Some of these results are discussed below, particularly regarding the stratification noted in a climatology of the area and numerical simulations of a larger domain.

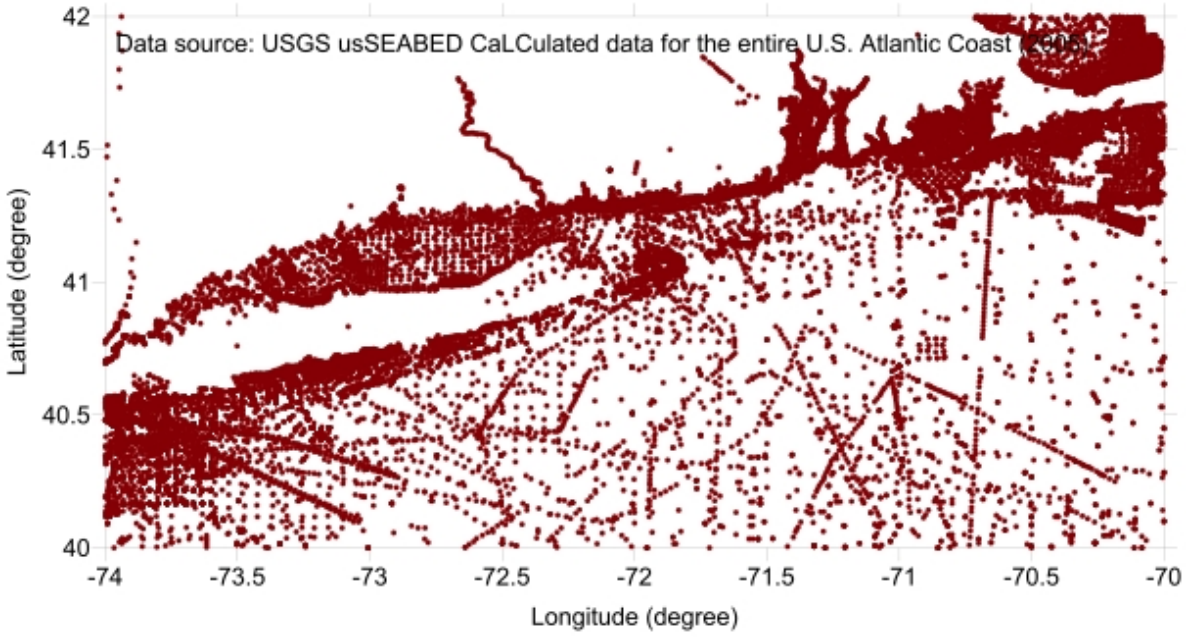

Figure 11: Locations where data was collected for USGS sediment texture database (Reid et al., 2005).

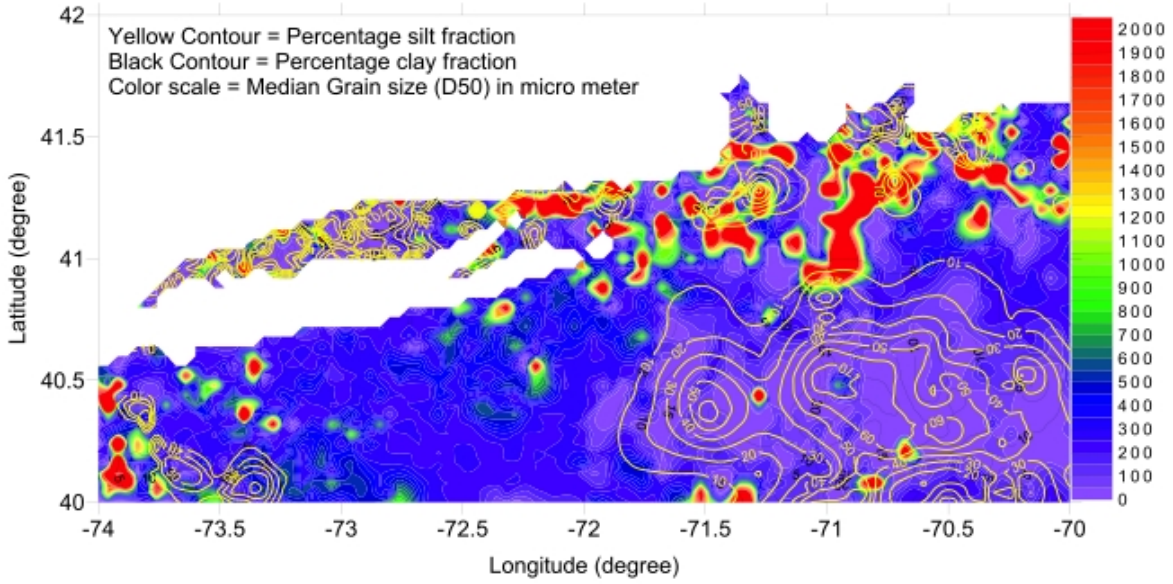

Figure 12: Map of median grain size, silt fraction, and clay fraction from the USGS sediment texture database (Reid et al., 2005).

4.3 Data for Model Validation

4.3.1 Buoy Data

Only a small number of observational studies have looked at currents in the area, and we discuss these below in the context of other modeling studies as well as the observational field program that is part of SAMP. Most data is obtained from tidal gage and bottom pressure measurements, although there is also surface data from radars, and vertical profiles of velocity at a few locations, from moorings or acoustic Doppler current profiler (ADCP) results. For this report, we will limit our discussion to measurements obtained from five locations listed in Table 1 and marked on Fig. 10, which include two buoys with surface-mounted ADCPs (at multi-disciplinary measurement sites in both state and federal waters; MD-S; MD-F), two bottom-mounted ADCPs (at a physical oceanography measurement site at nearby locations; PO-S; PO-F), and at a CDIP buoy station number 44097, which only measures wave parameters. The five locations are positioned in representative locations throughout the ocean SAMP study area (Fig. 10). Details regarding the exact variables measured are given below.

Table 1. Locations and data type for field buoys deployed in SAMP study area

Buoy	Latitude	Longitude	Deployed	Recorded variables
PO-S	41.0482° N	71.5003° W	9-15-2009—1-15-2010	$H_s, T_{peak}, \theta_{mean}, u, v$
PO-F	41.2500° N	71.0917° W	9-15-2009—1-15-2010	$H_s, T_{peak}, \theta_{mean}, u, v$
MD-S	41.1012° N	71.5672° W	9-Oct-2009 —	$H_s, T_{peak}, \theta_{mean}, u, v$
MD-F	41.1183° N	71.0284° W	9-Oct-2009 —	$H_s, T_{peak}, \theta_{mean}, u, v$
CDIP	40.9686° N	71.1261° W	Continuously	$H_s, T_{peak}, \theta_{mean}$

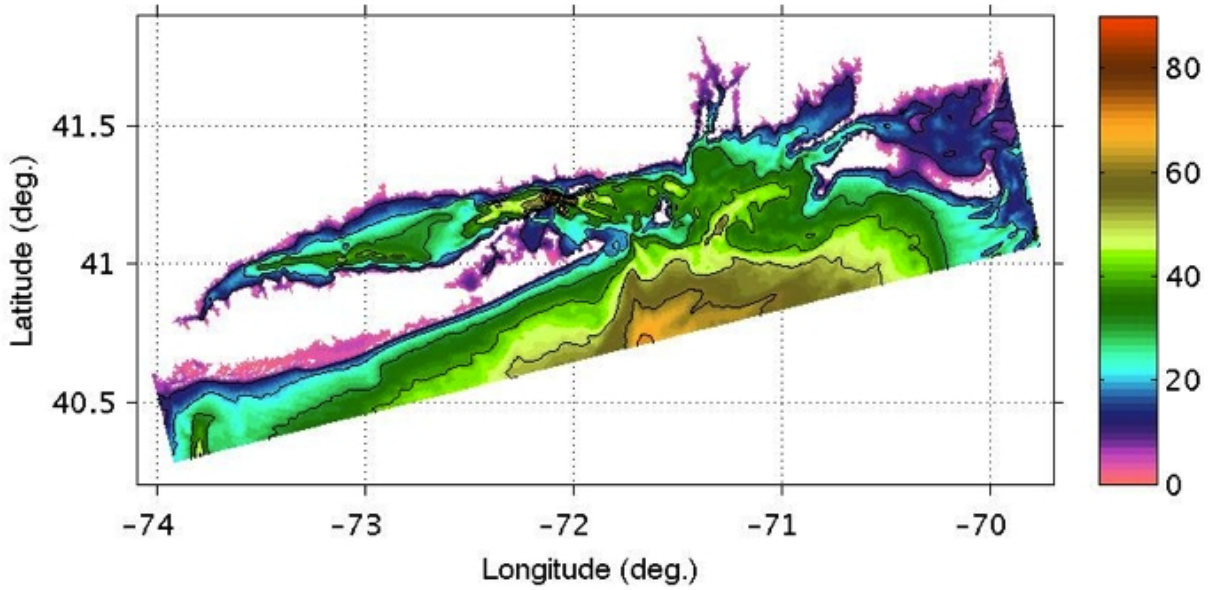

Figure 13. Bathymetry (m) for computational domain. Note that Massachusetts Bay and small rivers have been blanked out, since they do not connect with the computational domain in the area of interest.

4.3.2 Surficial Sediment Data

In order to understand sediment suspension due to bottom current velocity, it is first important to understand the present seafloor surficial sediment properties. A number of surveys have been conducted, of the surficial sediments in the area surrounding the SAMP study area (see e.g. Battelle, 2003). The most comprehensive summary of these studies is the USGS sediment texture database (Reid et al., 2005). By applying kriging to this dataset (Fig. 10), it is possible to

develop a surface map of the sediment properties (Fig. 11). Most of the surface sediment in the SAMP study area is coarse sand, but there is a wide range of variability.

Note that the USGS database only lists median grain size and not the grain size distribution, such as would be required for an initial condition of a sediment transport model. [Earlier results of Hastings et al. (2000) did include grain size distributions, but did not have as many samples in the area of interest.]

Model results mentioned earlier primarily focus on currents and other hydrographic fields, and there is very little information available concerning suspended sediment. Warner et al. (2008a) described a coupling of ROMS, mentioned above, with the wave model "Simulating Waves in the Nearshore" (SWAN) and a sediment transport model. This coupling has been successfully used by Blaas et al. (2007) for modeling sediment transport off of California, and by Warner et al. (2008b) for modeling sediment transport off of Massachusetts. Blaas et al. used a simple relationship between depth and grain size to initialize the seabed characteristics over their domain. One can see comparing Figs. 12 and 13, however, that this would not be an accurate reflection of the SAMP study area. Instead, to model sediment transport here, one would have to follow a methodology more similar to that of Warner et al., who started with an even distribution of many grain sizes, which over the spin-up time of the simulation, evolved into something approximating the actual seabed distribution.

4.4 Hydrodynamic Model ROMS/SWAN Overview and Setup

4.4.1 Bathymetry and Gridding

The Regional Ocean Modeling System (ROMS) is a high-resolution, free-surface, terrain-following coordinate oceanic model (Shchepetkin and McWilliams, 2005), which has been applied extensively to basin-scale and coastal circulation. Here we apply ROMS to study the hydrodynamics of the SAMP study area.

The computational domain, which extends over all of Long Island Sound, Block Island Sound, and Rhode Island Sound (Fig. 9) is discretized horizontally with an orthogonal curvilinear Arakawa-C grid, and vertically with a terrain-following sigma-coordinate formulation. To set-up the grid, detailed bathymetry was obtained from the 3" (about 90 m) resolution Coastal Relief Model data (Divins, 2003; Fig. 11). [In order to prevent numerical instabilities, the bathymetry was smoothed with three iterations of a second-order Shapiro (1975)

filter.] The southwestern-most point of the grid is at 40.8° N 73.92° W, and the grid is rotated 14 degrees counterclockwise with respect to a meridian. The horizontal grid used here for all of the ROMS simulations is 200 x 600, with a uniform 600 m resolution (Figs. 9, 10, 13).

In the vertical direction, the grid consists of 10 terrain-following levels. The vertical coordinate transformation is determined by the stretching function of Song and Haivogel (1994):

$$z(x,y,\sigma,t) = S(x,y,\sigma) + \zeta(x,y,t)\left[1 + \frac{S(x,y,\sigma)}{h(x,y)}\right]$$
$$S(x,y,\sigma) = h_c\sigma + [h(x,y) - h_c]C(\sigma)$$
$$C(\sigma) = (1-\theta_B)\frac{\sinh(\theta_S\sigma)}{\sinh\theta_S} + \theta_B\left[\frac{\tanh[\theta_S(\sigma+\frac{1}{2})]}{2\tanh(\frac{1}{2}\theta_S)} - \frac{1}{2}\right] \quad (2)$$

where σ varies from -1 (at the seabed) to 0 (at the surface). For the simulations in this report, θ_S is 1.0, θ_B is 0.8, and h_c is 0.0.

Unconnected sections of the ocean (e.g., unresolved rivers; Massachusetts Bay) were masked from the computational domain, since their results would be anomalous and have no effect on the region of interest.

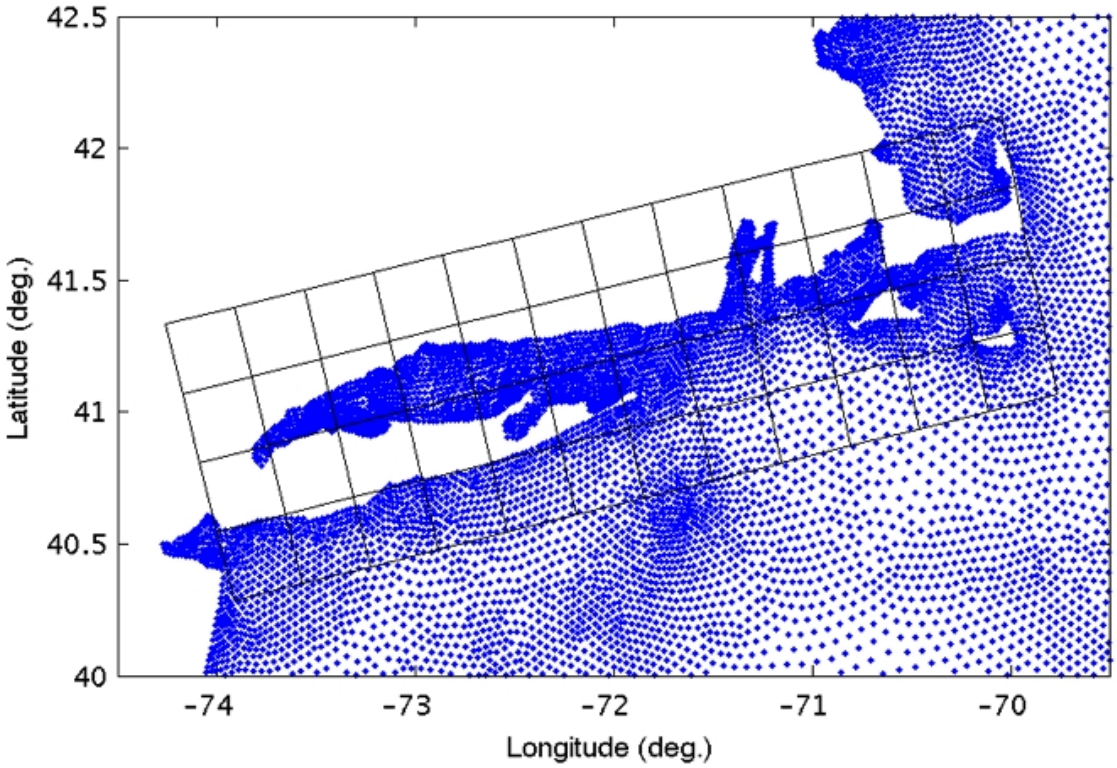

Figure 14. The black grid indicates part of the ROMS/SWAN grid (each square is 30 km across, corresponding to 50x50 gridpoints in the high resolution simulations). Blue points mark the unstructured grid used in the ADCIRC regional model of tides.

4.4.2 Tidal forcing

One of the most important forcing for bottom currents over the SAMP study area is from tides. Hence, two separate modeling investigations were conducted for this important aspect of coastal hydrodynamics in the SAMP area. This allowed for cross-validation between those independent approaches, with the additional experimental validation (discussed later) using data from SAMP's field program. The first modeling of tides was performed as part of ASA's subcontract, using their in-house code HYDROMAP. A detailed report of this work is provided in Appendix A. The second modeling of tides was done as part of ROMS simulations, first only using tidal forcing, then using all the other environmental forcing (waves and wind) together with tides.

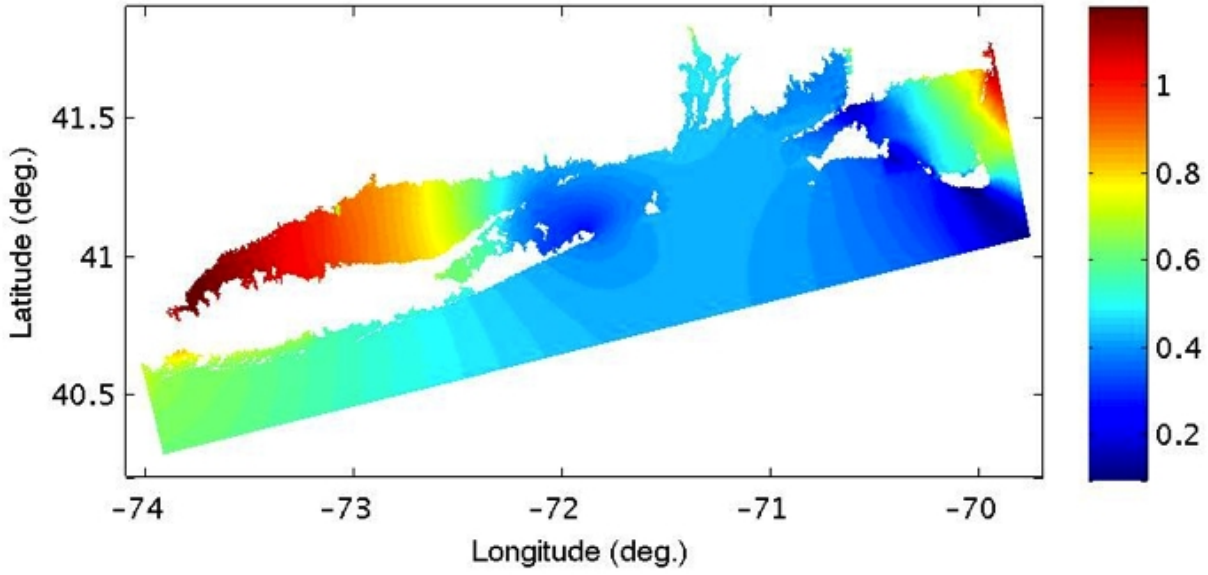

Figure 15. M_2 tidal amplitude (m) from ADCIRC tidal database as interpolated onto the ROMS grid.

To force tides in the ROMS model, we use the Western North Atlantic, Caribbean and Gulf of Mexico Tidal Database (Mukai et al. 2002), which includes the M_2, S_2, N_2, K_2, O_1, K_1, Q_1, M_4, M_6, and steady tidal constituents. This database is based on simulation results from the coastal circulation model ADCIRC (Fig. 14), which itself is forced along the open boundary with the Le Provost et al. (1998) tidal database FES95.2, formed from satellite altimetry. This ADCIRC tidal forcing was independently validated against measured tidal amplitudes and phases for 7 different components, at several stations close to the SAMP area (i.e., at Woods Hole, MA, Nantucket Island, MA, Block Island, RI, and Montauk, NY; for details see Mukai et al., 2002). Note that

the M_2 tidal constituent (Figs. 15, 16) is most significant around BI. For all the stations used for validation by Mukai et al. along the Atlantic Coast, an error of 2.7% for the amplitude and 2.5 deg for the phase was found for the M_2 component.

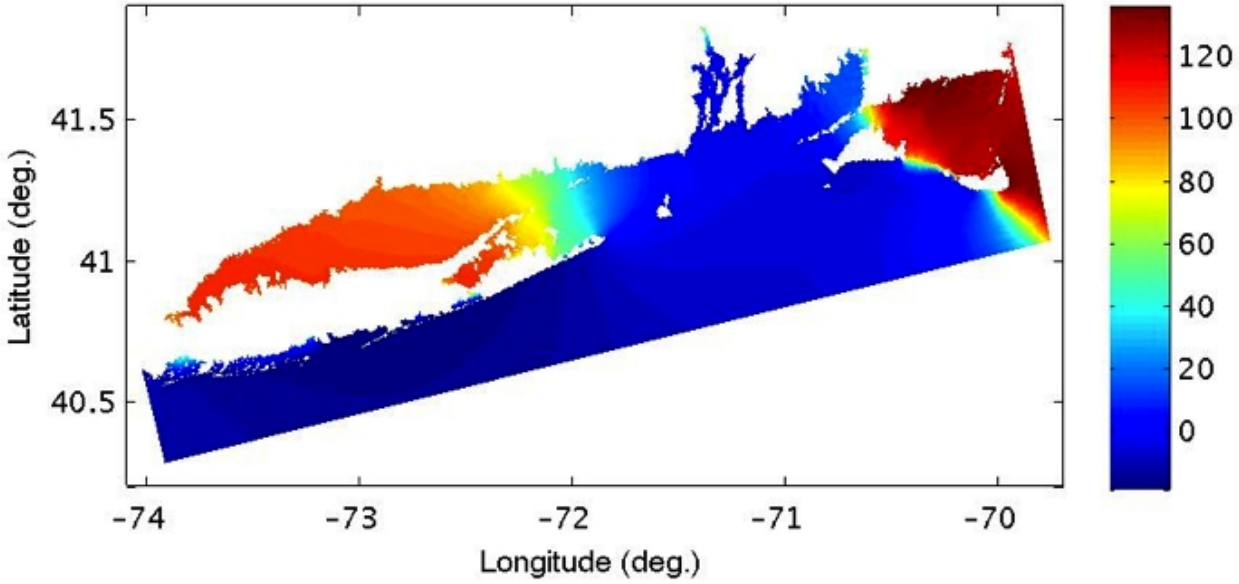

Figure 16. M_2 tidal phase (degrees from GMT) from ADCIRC tidal database as interpolated onto the ROMS grid.

For tidal simulations using ROMS, velocity and sea surface height from the ADCIRC tidal database are applied as numerical forcing along the boundary of our ROMS grid, using both the Flather (1976) radiation condition as well as the Chapman (1985) boundary condition. Nudging is also applied to the grid points closest to the boundary, to force the ROMS's solution at the boundary to tend towards that of the tidal boundary condition. In order to use the ADCIRC results to initialize simulations in the ROMS/SWAN grid, the tidal amplitude and phase of each constituent were linearly interpolated onto the new grid (Figs. 15, 16). For points of the ROMS grid that are outside the ADCIRC grid, values were filled in with the average of the nearest grid points that did fall within the tidal database.

4.4.3 Wave Forcing

For the complete ROMS runs, wave forcing is applied together with tidal and other forcing, by coupling ROMS to the SWAN model (Simulating Waves Nearshore; Booij et al., 1999). SWAN is a third-generation, non-stationary (time-varying), phase-averaged model that solves for the wave action density conservation (including wind forcing terms, wave breaking and bottom friction dissipation, and nonlinear quadruplet wave-wave interactions). SWAN simulations were

performed in a grid identical to that used for ROMS (Fig. 9). Information exchanged between SWAN and ROMS includes wave direction, significant wave height, average wavelength, wave period, bathymetry, free-surface height, vertically integrated momentum, and bottom roughness.

The boundary conditions for SWAN is set using a similar but larger scale operational ocean wave prediction model, NOAA's WAVEWATCH III. NOAA keeps records of significant wave height, peak period, and peak wave direction. To apply these as both initial and boundary conditions in SWAN, a JONSWAP wave energy spectrum $S(\omega)$ (Hasselmann et al., 1973) is assumed at each grid point, based on the WAVEWATCH III parameters defined as the significant wave height H_s, the peak wave period, $T_p = 2\pi/\omega_p$, and the peak wave direction, θ_p:

$$\begin{aligned} S(\omega,\theta) &= S(\omega)D(\theta) \\ D(\theta) &= \frac{2}{\pi}\cos^2(\theta-\theta_p) \end{aligned} \tag{3}$$

where:

$$\begin{aligned} S(\omega) &= \frac{\alpha g^2}{\omega^5}\exp\left[-\frac{5}{4}\left(\frac{\omega_p}{\omega}\right)^4\right]\gamma^r \\ r &= \exp\left[-\frac{(\omega-\omega_p)^2}{2\sigma_0^2\omega_p^2}\right] \end{aligned} \tag{4}$$

and

$$\begin{aligned} \sigma_0 &= \begin{cases} 0.07 & \omega < \omega_p \\ 0.09 & \omega \geq \omega_p \end{cases} \\ \gamma &= 3.3 \end{aligned} \tag{5}$$

the average peakedness factor, and α is the equilibrium-range (or Phillips) parameter. Note, a coarser resolution (4 minute or about 5.6 km east-west and 7.4 km north-south) grid is used for WAVEWATCH III (Fig. 17). A process similar to that used for tides is used to fill-in data for points on the ROMS grid that fall outside the WAVEWATCH III grid. In order to verify whether WAVEWATCH III data represents a good boundary condition to the SWAN simulations, the WAVEWATCH III data is compared to the wave data recorded at the five stations mentioned

earlier (Table 1, Fig. 10). This is done in Figs. 18—22 and we see that, at least qualitatively, the agreement is quite good.

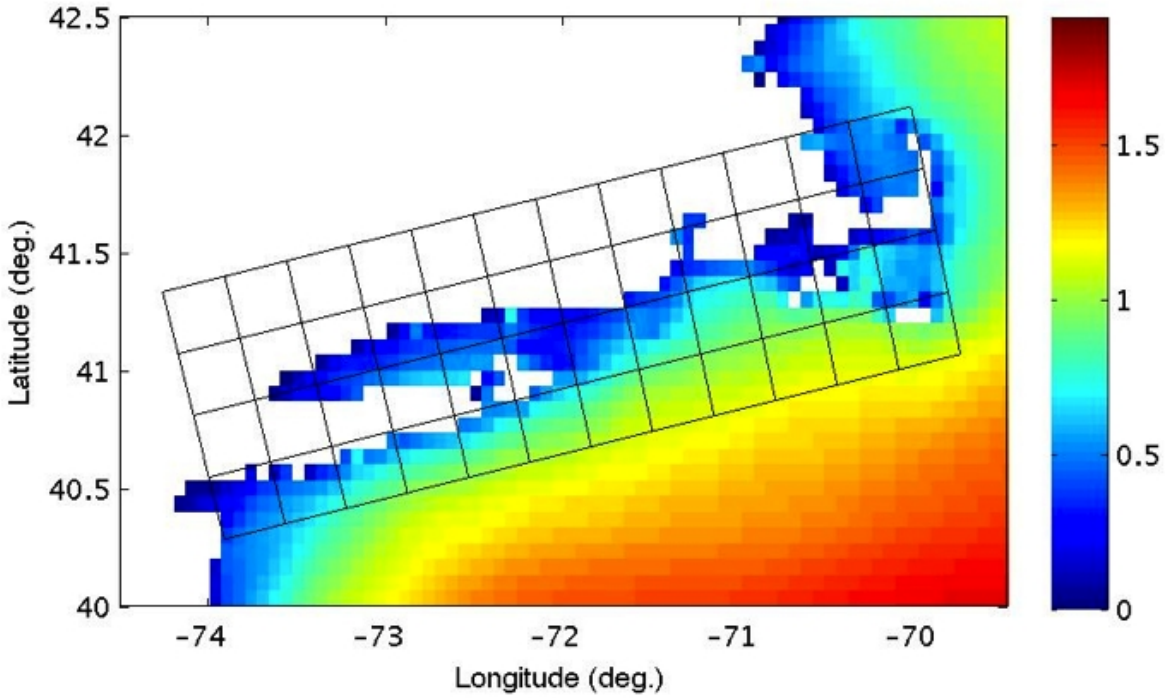

Figure 17: Significant wave height (m) predicted by WAVEWATCH III on Oct. 1st, 2009 at 000 GMT, and ROMS/SWAN domain (black grid; each square is 30 km across, corresponding to 50x50 grid points in the 600 m resolution simulations, in comparison to the 4 min. or about 5.6 km east-west and 7.4 km north-south resolution of the WAVEWATCH III results).

4.4.4 Wind Forcing

For the complete ROMS runs, wind forcing was applied as well, using results of a 5 month hindcast (October 2009 — February 2010) conducted by WeatherFlow on a SAMP subcontract. These wind simulations were performed with version 6.1 of the Regional Atmospheric Modeling System (RAMS), using 4 levels of nested grids (varying in horizontal resolution from 500 m to 12 km), the finer one being centered around Block Island. The vertical resolution was 20 m at the surface, with a stretching ratio of 1.15. The RAMS model was initialized and bounded by the North American Mesoscale (NAM) results, produced by the National Center for Environmental Prediction (NCEP), which is presently generated by the Weather Research and Forecasting Non-hydrostatic Mesoscale Model (WRF-NMM).

The time varying wind speed at 10 m computed by RAMS is used to force ROMS and SWAN (Figs. 23 and 24). Because of project time limitations, it was not possible to have RAMS output the wind stress at each point, but instead the 10 m wind is applied to SWAN, and a surface stress

is applied to the ROMS domain, assuming a neutrally stable atmosphere. Specifically, given the wind at 10 m, the surface stress is computed assuming that near the surface the velocity profile can be approximated by:

$$u = \frac{u_*}{\kappa} \log \frac{z}{z_0}$$
$$z_0 = 0.016 \frac{u_*^2}{g} \qquad (6)$$

where u is the wind velocity, u_* is the friction velocity, z is the height (e.g., 10 m), κ is the Von Karman constant (0.40), g is the acceleration due to gravity (9.81 m/s^2), and z_0 is the surface roughness, given by a Charnock's relationship as shown above.

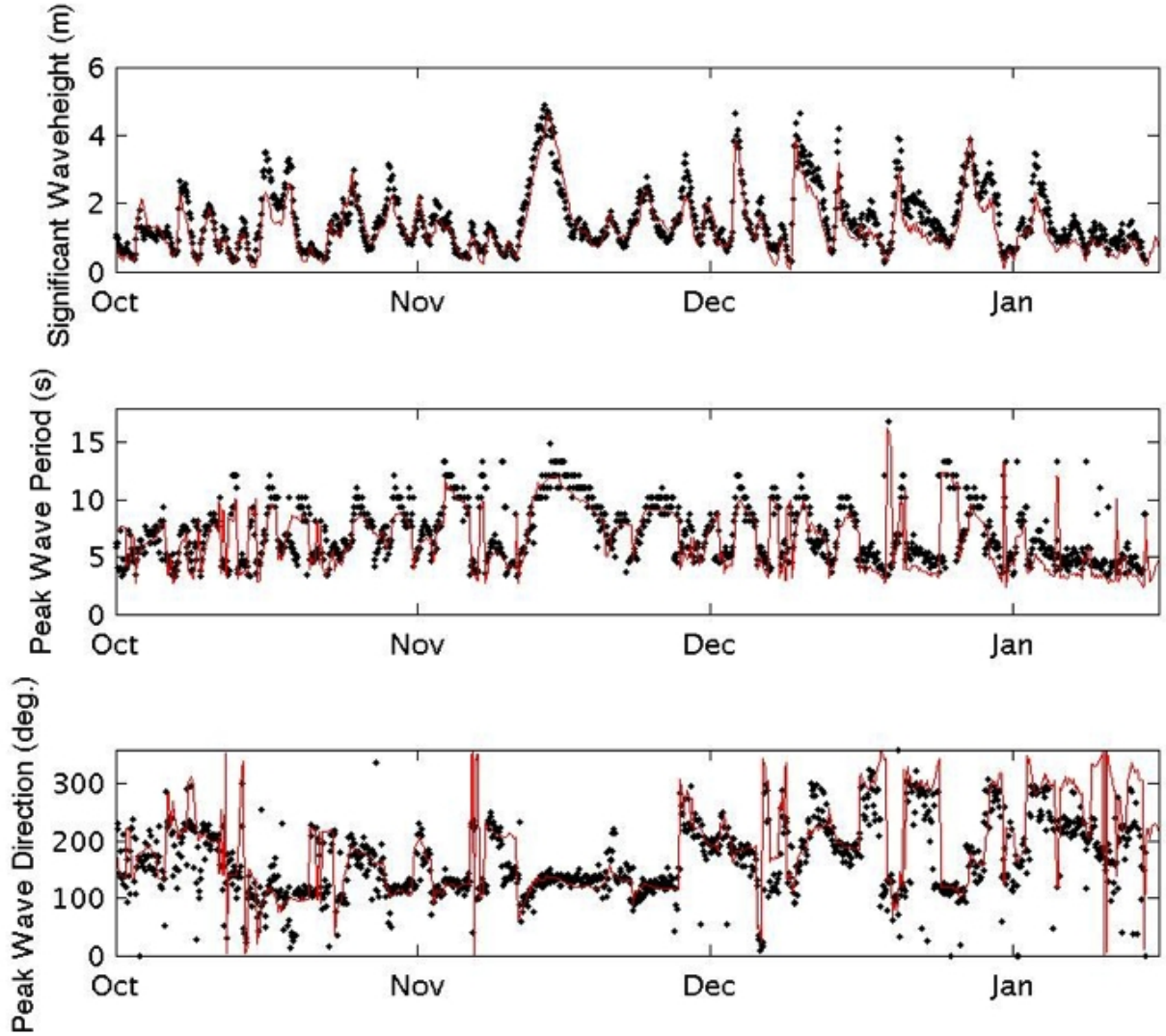

Figure 18: Significant wave height, peak period and direction measured at the PO-S buoy (41.0482° N 71.5003° W) (black dots), compared to WAVEWATCH III simulations (solid red line).

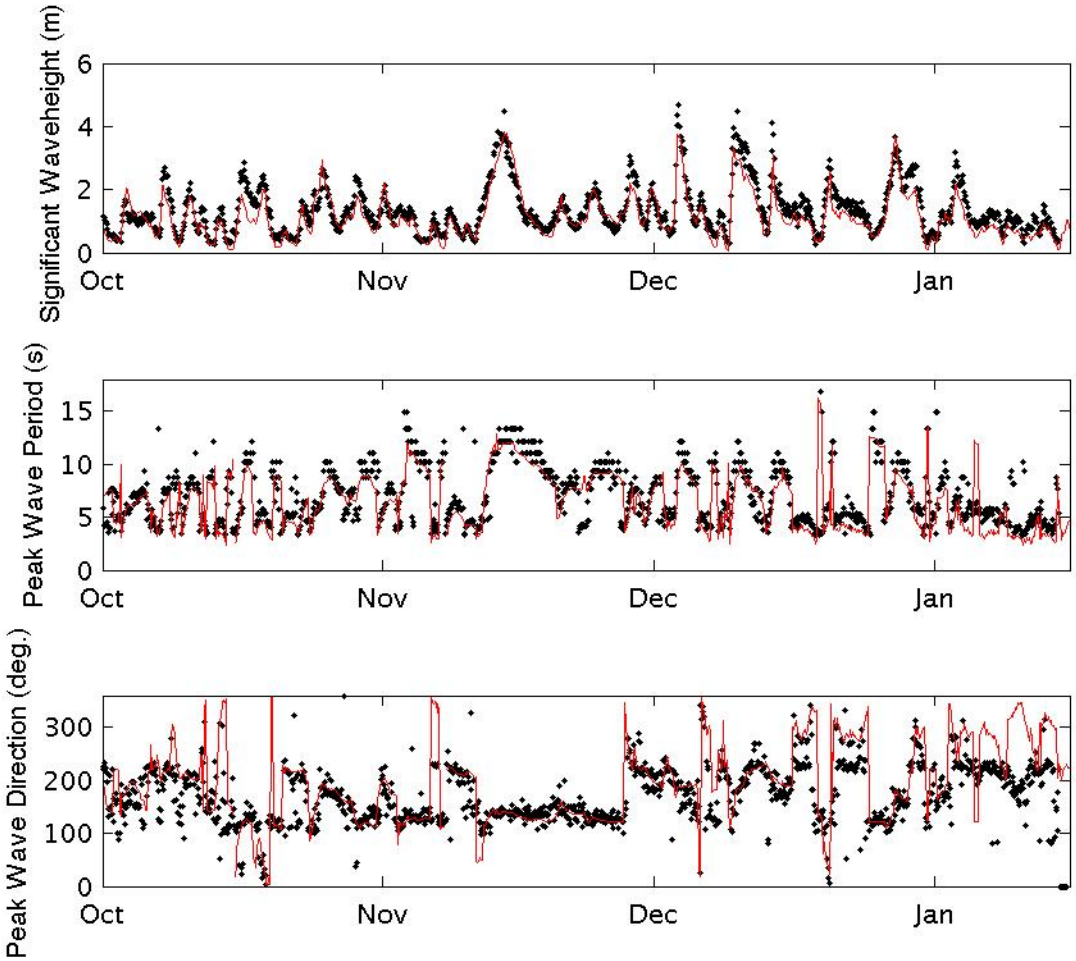

Figure 19. Same as Fig. 18 at the PO-F buoy (41.2500^{o} N 71.0917^{o} W).

The coefficient 0.016 is consistent with that used in the RAMS hindcast. Note that this ignores wind gustiness.

Since all three simulations use different parameterizations of the ocean-atmospheric boundary layer, a slight inconsistency is unavoidable. For instance, RAMS simulations include the effect of atmospheric stability (resulting from the air-sea temperature difference) in determining the surface wind stress. ROMS is able to do the same, but here we force ROMS assuming an essentially neutrally-stable atmosphere. SWAN assumes a logarithmic profile for the wind over the ocean, but accounts for the wave height, which the other two models do not.

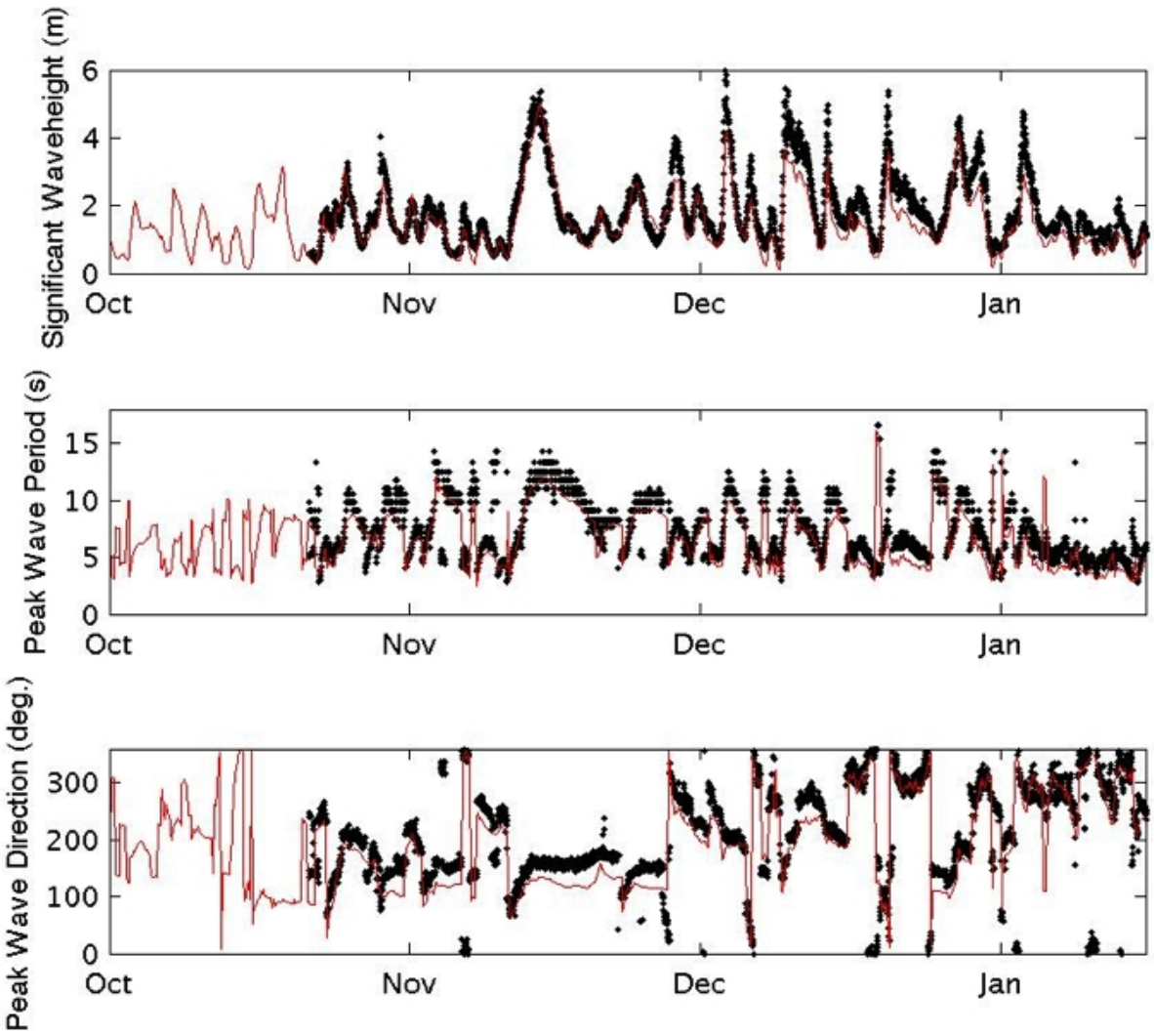

Figure 20. Same as Fig. 18 at the CDIP buoy (40.9686^{o} N 71.1261^{o} W)

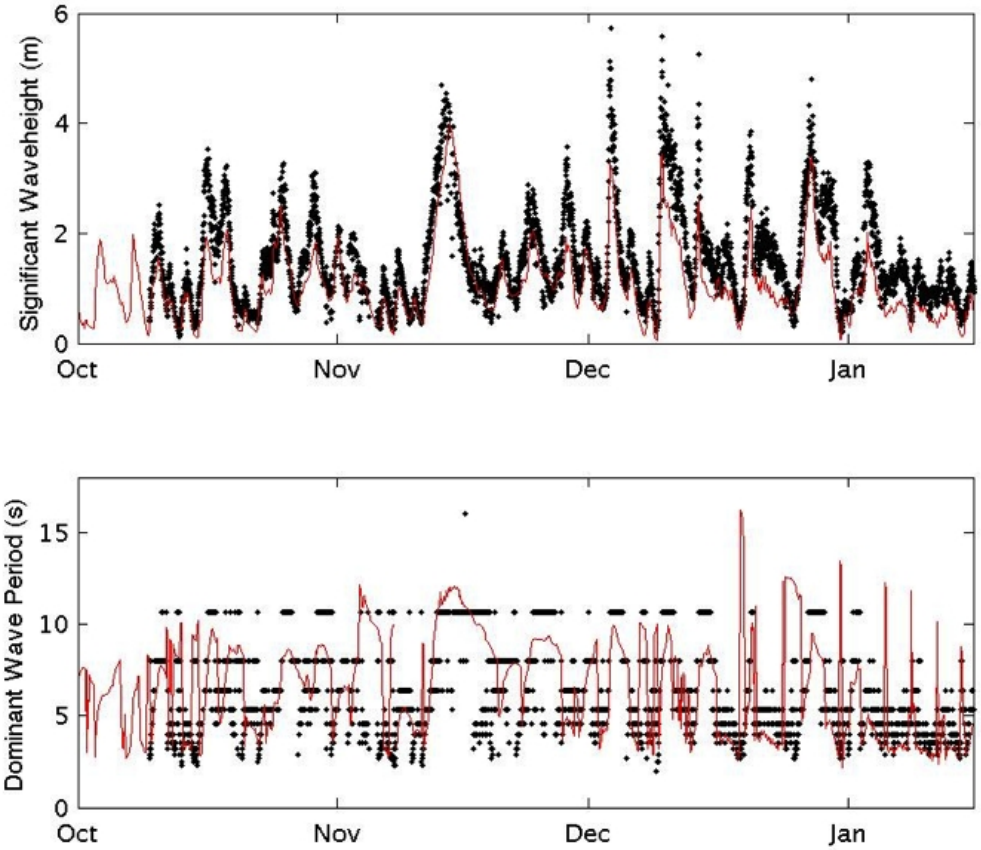

Figure 21. Same as Fig 18 at the MD-S buoy (41.1012° N 71.5672° W).

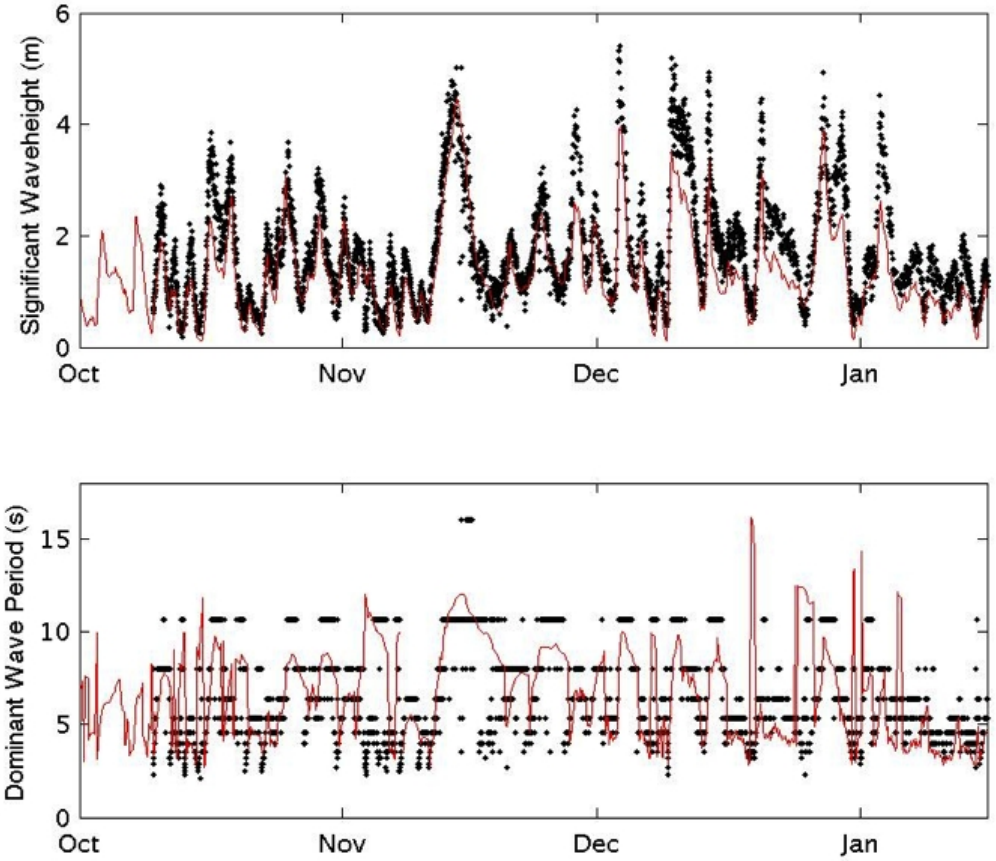

Figure 22. Same as Fig. 18 at the MD-F buoy (41.1183° N 71.0284° W).

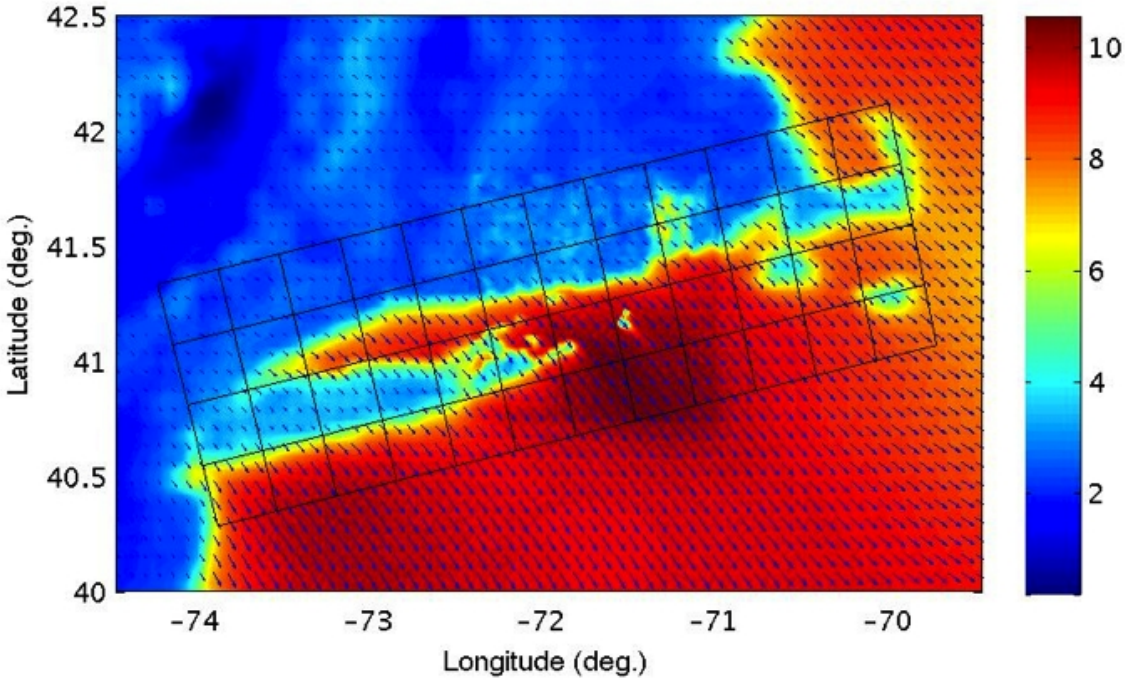

Figure 23. Wind speed at 10 m as simulated by RAMS on Oct. 26th, 2009 at 000 GMT (color in m/s). Vectors indicate wind direction, and the black grid indicates the ROMS/SWAN domain (each square is 30 km across, corresponding to 50x50 grid points in the high resolution 600 m simulations).

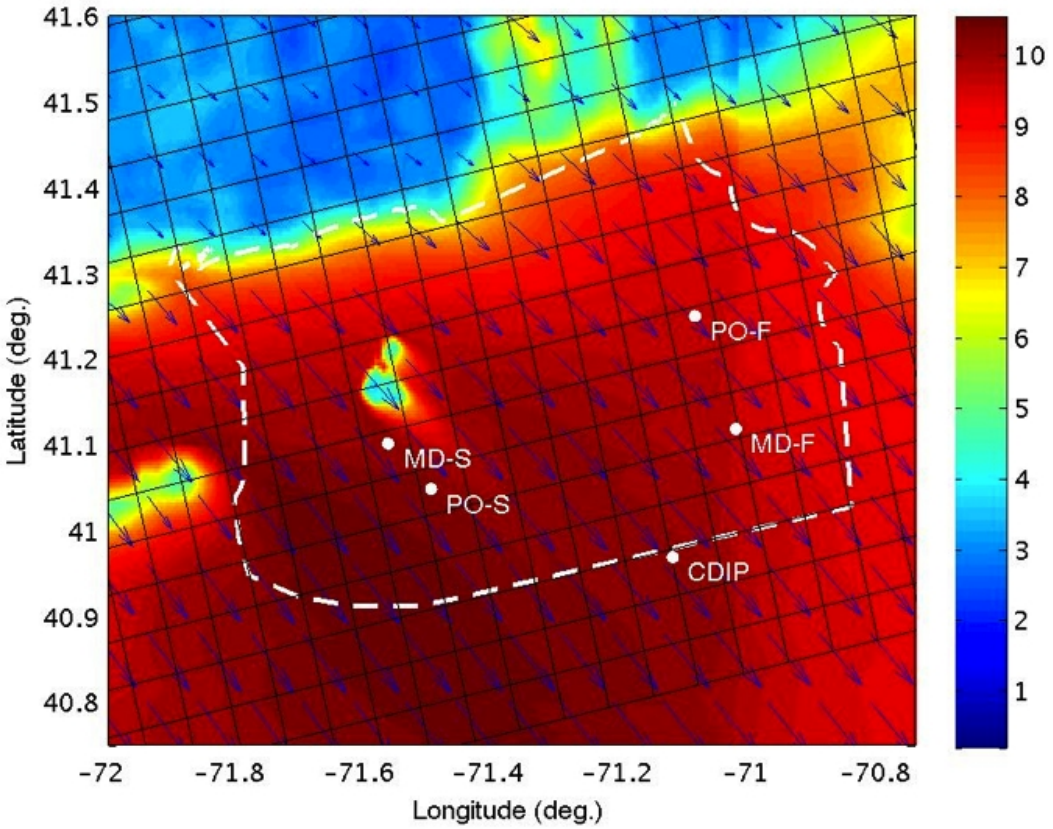

Figure 24. Zoom of Fig. 23 on SAMP area (black grid is ROMS/SWAN dimain; each square is 6 km across, corresponding to 10x10 grid points in the high resolution simulations).

4.4.5 Bottom Boundary Layer and Turbulence Closure

The bottom boundary layer stress can be significantly affected by surface waves. When considering only tides, and not waves as well, a quadratic form of seabed drag is used. In order to remain consistent with the ADCIRC tidal simulation data, we use a drag coefficient C_f = 0.0025. Because of this, we expect that the tidal velocities simulated in ROMS should be approximately as accurate as those obtained by the ADCIRC model itself, simply on a finer grid.

When a coupled ROMS/SWAN simulation is conducted, a wave-current bottom boundary layer model is applied instead, using the *ssw_bbl* formulation as described by Warner et al. (2008a). The seabed is assumed to have ripples of height and wavelength estimated using the method of Wiberg and Harris (1994): the bottom boundary layer roughness is estimated as a combination of that from grain roughness, sediment transport, and bedform roughness length; the seabed stress is predicted as a sum of that from both waves and currents, and the mean bottom stress is determined iteratively from an assumed eddy viscosity profile.

In each case, the Mellor-Yamada 2.5 closure is used for the vertical mixing scheme (1982).

Table 2. Characteristics used in ROMS sediment suspension and transport simulations (8 classes).

Sediment (phi)	Diameter (mm)	Density (kg m^{-3})	Settling vel. (mm s^{-1})	Erosion rt. (kg m^{-2} s^{-1})	Crit. shear (N m^{-2})
-2	4.0	2650	276.2	$5.0 \cdot 10^{-6}$	2.913
-1	2.0	2650	189.2	$5.0 \cdot 10^{-6}$	1.457
0	1.0	2650	122.8	$5.0 \cdot 10^{-6}$	0.612
1	0.5	2650	70.6	$5.0 \cdot 10^{-6}$	0.249
2	0.25	2650	32.7	$5.0 \cdot 10^{-6}$	0.178
3	0.125	2650	11.7	$5.0 \cdot 10^{-6}$	0.173
4	0.0625	2650	3.4	$5.0 \cdot 10^{-6}$	0.116
5	0.03125	2650	0.92	$5.0 \cdot 10^{-6}$	0.073

4.5 Sediment Modeling

Suspended sediment is modeled by ROMS, as a conservative tracer using an advection-diffusion equation with a constant vertical settling velocity term. See Warner et al. (2008a) for full details of the coupled ROMS, SWAN, and sediment transport model. In order to model a distribution of sediment diameters, 8 different sediment classes are considered, from 4 mm to 0.03125 mm.

Sediment modeling depends on a number of parameters, including settling velocity, density, critical shear strength, and many others (Table 2). Settling velocity was determined using the empirical relation of Jimenez and Madsen (2003), and the critical shear stress is set by the explicit formulation of the Shields curve as formulated by Cao et al. (2006). Because the sediment characteristics are not well-known, the erosion rate and porosity of the bed is chosen to match the study of Warner et al. (2008b), of sediment transport in Massachusetts Bay.

Although not a primary goal of this work, bedload transport is also modeled as part of ROMS simulations. When waves are not simulated, the Meyer-Peter Mueller (1948) formulation of bedload transport is used, relating the bedload transport to the excess shear stress. When SWAN is coupled to ROMS, the model of Soulsby and Damgaard (2005) is applied, which takes into account the combined wave and current effects.

In order to test the validity of the ROMS results, simulations are conducted for the period from Oct. 1, 2009 to Jan. 16, 2010. This starts at the beginning of the available RAMS hindcast data, and ends at the end of the available ADCP data. The ROMS time step for each simulation is 2 minutes, and the SWAN time step for those involving wave-coupling is 4 minutes.

4.6 Results and Applications

4.6.1 Available Buoy Data

In addition to wave parameter measurements shown earlier (Fig. 18—22), the measurements at PO-S and PO-F include the current profiles and the surface elevation. We observe significant variation in the currents at these two stations (Fig. 25, 26) at both tidal and subtidal frequencies, although the currents at PO-S are noticeably stronger than those at PO-F.

Another use of the data measured at PO-S and PO-F is to verify the simulated tidal elevation at these locations (Fig. 27, 28), using the data from the pressure sensor attached to the bottom-mounted ADCP. While numerical limitations can affect the tidal elevations from ROMS near shore (e.g., within one or two grid cells of the shoreline), both the tidal elevation and amplitudes at an offshore location such as those two stations (i.e., PO-S; PO-F) should be correct if the hydrodynamics is correctly modeled. An analysis of the results, using T_TIDE (Pawlowicz et al., 2002) provides the harmonic constituents for future comparison (Tables 3, 4). For PO-S, 84.9% of the variance measured can be attributed to the tidal predictions, and for PO-F, 82.4% of the variance measured can be attributed to the tides.

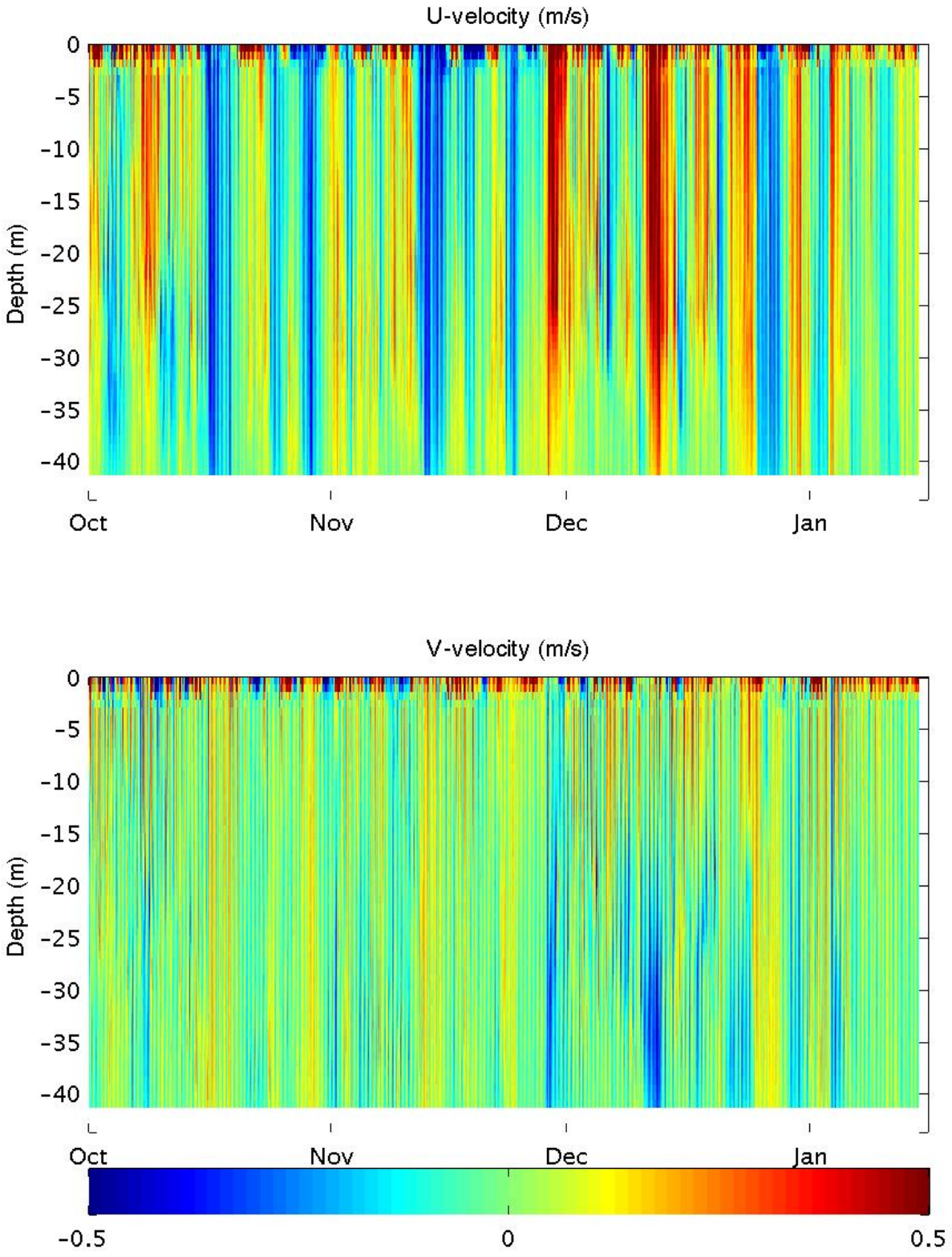

Figure 25. Current profiles for PO-S (41.0482° N 71.5003° W) measured by bottom-mounted ADCP. Note the strong diurnal signal throughout most of the water column, and that any strong vertical gradients of currents occurs near the surface.

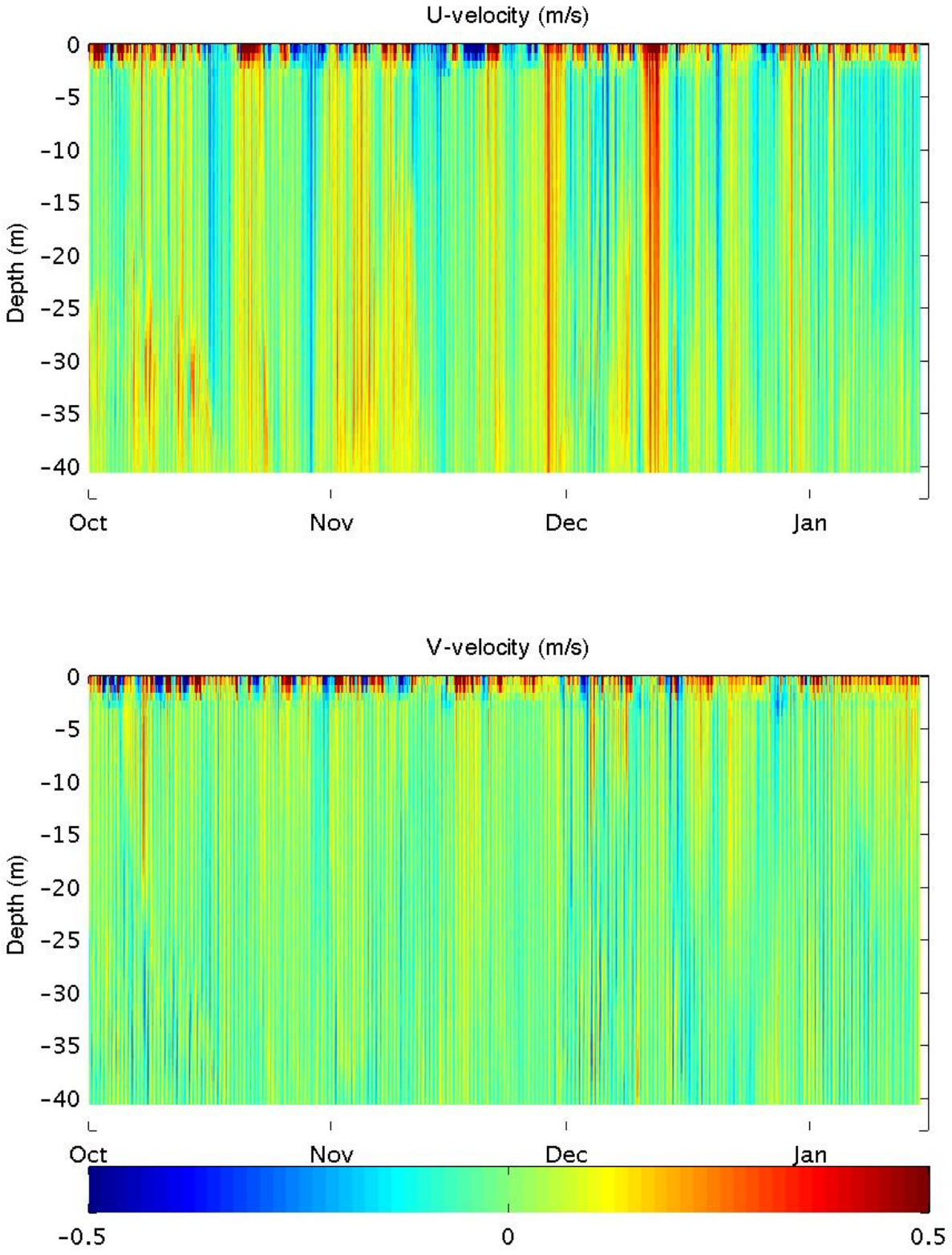

Figure 26. Current profiles for PO-F (41.2500° N 71.0917° W) measured by bottom-mounted ADCP. Note the strong diurnal signal throughout most of the water column, and that any strong vertical gradients of currents occurs near the surface.

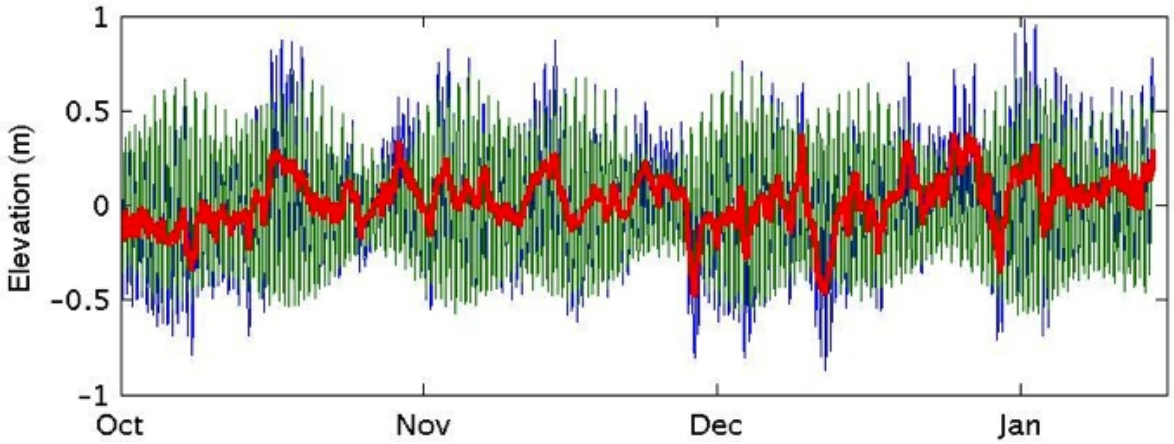

Figure 27. Surface elevation derived from pressure measured at a bottom-mounted ADCP, at the PO-S buoy (41.0482° N 71.5003° W), including original time-series (blue), tidal prediction from ROMS analysis (green), and difference between measurements and prediction (red).

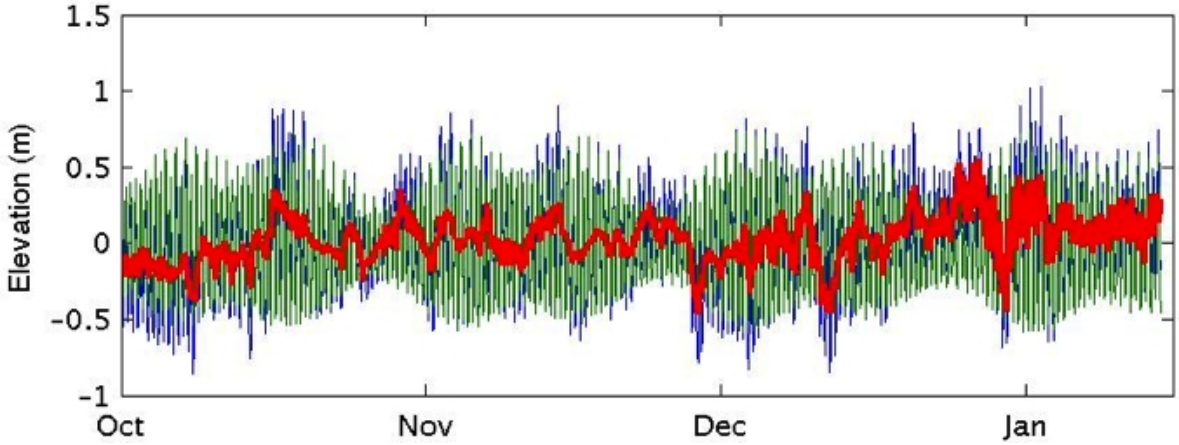

Figure 28. Same as Fig. 27 for the PO-F buoy (41.2500° N 71.0917° W).

Table 3. Amplitude and phase angle measurements for the seven most significant harmonic constituents at PO-S (41.0482° N 71.5003° W) (Fig. 26).

Constituent	Amp. (m)	Amp. Err. (m)	Phase (deg.)	Phase Err. (deg.)
O1	0.0466	0.009	193.33	10.30
K1	0.0725	0.009	166.82	6.85
N2	0.1035	0.008	350.54	4.63
M2	0.4427	0.007	3.92	0.98
S2	0.0945	0.008	18.70	4.83
M4	0.0218	0.002	16.31	6.08
M6	0.0107	0.002	201.29	11.78

Table 4. Amplitude and phase angle measurements for the seven most significant harmonic constituents at PO-F (41.2500° N 71.0917° W) (Fig. 27).

Constituent	Amp. (m)	Amp. Err. (m)	Phase (deg.)	Phase Err. (deg.)
O1	0.0478	0.010	194.82	11.92
K1	0.0684	0.010	167.20	8.77
N2	0.1114	0.013	344.74	7.52
M2	0.4517	0.013	0.92	1.70
S2	0.0976	0.012	18.23	6.82
M4	0.0335	0.004	7.41	7.35
M6	0.0057	0.002	180.12	23.10

While no measurements of the suspended sediment were made at any of the buoy locations, it is possible to apply a heuristic approach. Indeed, the ADCP backscattering data can be related to suspended sediment concentration, by assuming that near-bottom backscattering would be significantly higher when sediment is suspended. Because the ADCP deployments at PO-S and PO-F were not setup to intentionally measure suspended sediment concentration, no calibrations of the sensors were conducted. ADCP backscatter is recorded as a received signal strength indicator count, which is proportional to the backscatter intensity in decibels. The constant of proportionality can vary as much as 20% even among the different transducers of the same ADCP (Deines 1999). This, in combination with not knowing the exact grain size distribution or other details of potential suspended matter, means that it is not possible to exactly compute a suspended sediment concentration from ADCP counts, although it is an area of recent research (see e.g., Gostiaux and van Haren 2010). In general, though, a higher ADCP count corresponds to a greater amount of backscatter. Acoustic backscatter can be caused by any material suspended in the water column, including bubbles, fish, plankton, and sediment. For the three month period of interest, high ADCP counts seem to roughly correspond to periods of large wave height (Fig. 28), but there is not a similar agreement with wind speed or other measured parameters. The strong (qualitative) correlation between ADCP counts and significant wave height thus suggests that backscattering may primarily not be biological in nature but likely related to sediment suspension induced by wave bottom currents (and at over 40 m of depth, bubbles are unlikely to contribute significantly).

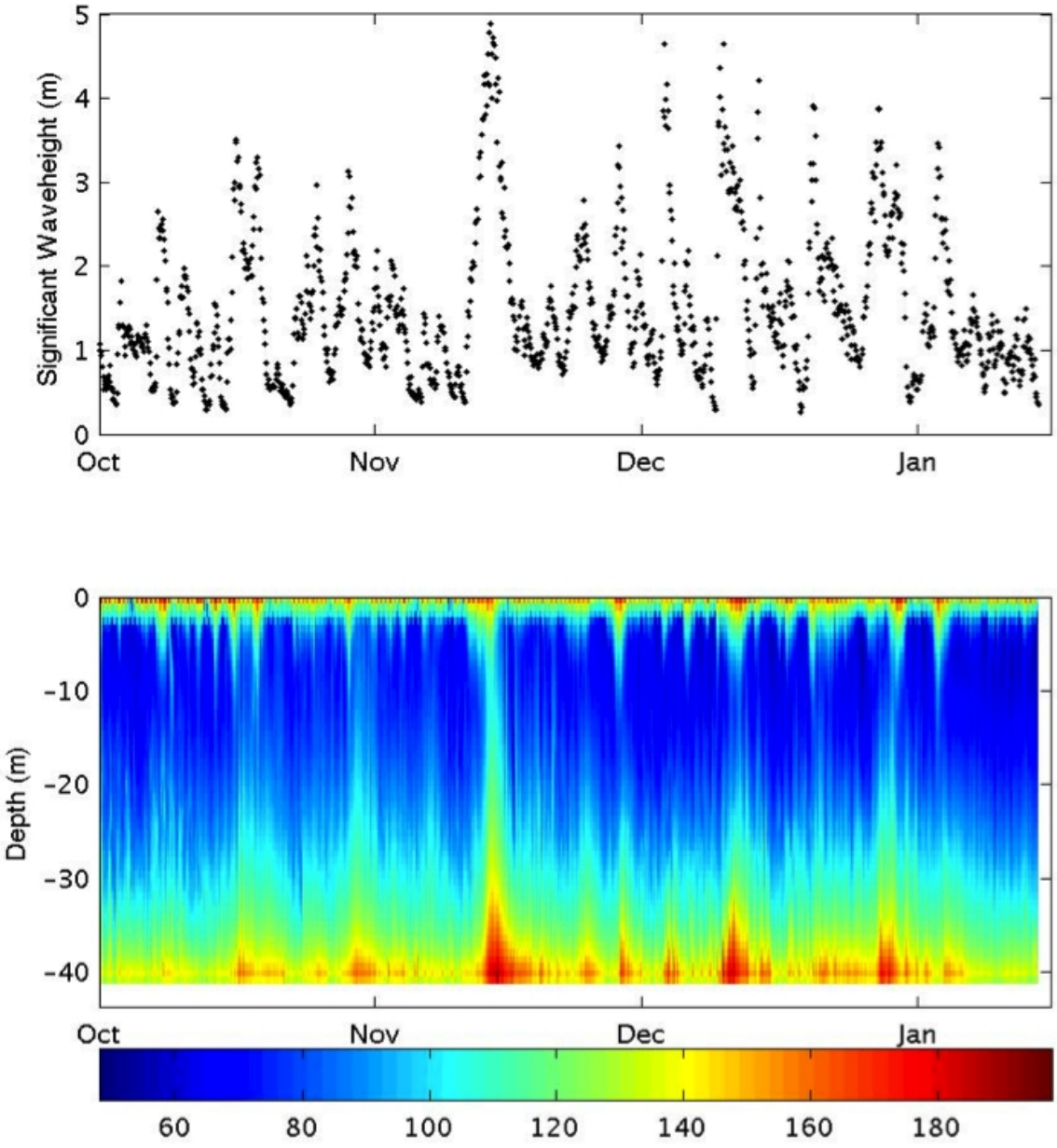

Figure 29. Comparison of the significant waveheight measured at PO-S (41.0482° N 71.5003° W; top) and the ADCP counts at the same location, indicative of backscatter intensity (bottom) for October 2009 through mid-January 2010. Note that ADCP counts near the seabed (potentially indicative of suspended sediment) is qualitatively related to the local waveheight.

4.6.2 ROMS Simulation: Forced by Tides

The most important forcing is due to tides, as it is persistent even in calm conditions, and tidal velocities can be sufficient to suspend sediment in the area. Other forcing, such as from winds, waves, primarily acts on surface velocities, except under storm conditions, and density-driven circulation is generally very weak in the area.

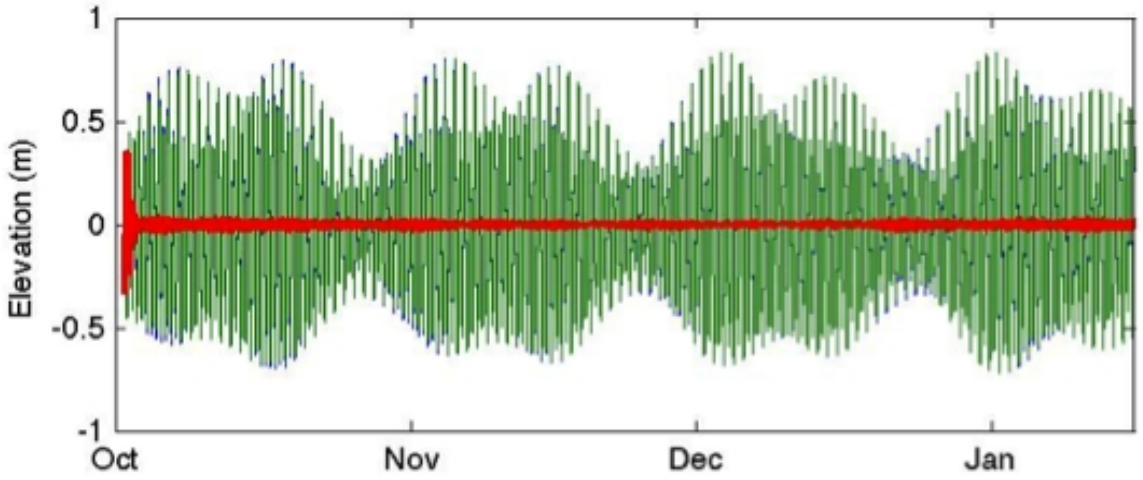

Figure 30. Surface elevation predicted by ROMS with only tidal forcing, at PO-S (41.0482° N 71.5003° W): modeled time-series (blue); predicted oscillations corresponding to tidal frequencies (e.g., M2, N2, K1, S2, etc.) (green); and differences between time-series and prediction (red). Note that the non-tidal transient of model spin-up subsides within a few days and quickly achieves a quasi-steady result.

Table 5. Amplitude and phase angle predictions for ROMS simulations with only ADCIRC tidal forcing (Fig. 29), for the 8 most significant harmonic constituents at PO-S (41.0482° N 71.5003° W).

Constituent	Amp. (m)	Amp. Err. (m)	Phase (deg.)	Phase Err. (deg.)
Q1	0.0109	0.001	181.71	4.06
O1	0.0607	0.001	183.73	0.71
K1	0.0958	0.001	169.11	0.49
N2	0.1305	0.005	0.19	2.32
M2	0.4939	0.005	21.97	0.55
S2	0.0876	0.005	28.97	2.65
M4	0.0264	0.000	324.80	0.72
M6	0.0071	0.000	199.87	3.94

In order to evaluate the performance of ROMS for predicting tides, we first consider the tidal elevation record simulated at PO-S (Fig. 29), comparing the modeled elevation record to the modeled elevation record that matches the frequency of tidal constituents. We find that the differences between the two are negligible for most of the simulation time. At the very beginning of the simulation, during model spin-up, there is a significant transient, but this subsides within a few days. By doing a similar tidal analysis as in the prior section, we find that the modeled harmonic constituents (Table 5) match the measured data (Table 3) well, for nearly all constituents. The agreement is not as good as that found between tidal measurements in the same area and the original ADCIRC database (Mukai et al. 2002), but e.g., the M2 amplitude only has an 11% error at the PO-S station.

In terms of velocity profiles, the results are relatively straightforward: with only tidal forcing at the boundaries of ROMS, and drag at the seabed, the vertical variation in velocities is minimal, with smaller tidal amplitudes at depth than at the surface (Fig. 31, 32).

While, overall, these results do not appear to be close to the measurements at PO-S and PO-F (Fig. 25, 26), if one considers only a time-series at, e.g., 20 m (Fig. 33), one obtains a different view. One can clearly see on Fig. 33 that the measured velocity has a time variability similar to that of the tidally-induced velocity, but at times the velocity can differ or be shifted significantly from the tidal velocities. Examining a shorter time period in Fig. 34, however, it seems that the north-south (*v*-component) velocity does show a better agreement between the ROMS results and the ADCP measurements, including the phase of the tidal component, but this agreement is not as good in the east-west direction (*u*-component). This suggests that the missing forcing terms in the tidal only ROMS simulations (i.e., waves and winds) should be acting most significantly along the east-west direction. This will be further discussed for the complete ROMS simulations, including all forcing terms, which are presented later in this report.

The other substantial result from this ROMS simulation, that only considers tides, is with respect to sediment processes. One can start by considering simulated suspended sediment concentrations at the PO-S buoy site (Fig. 35). Rather than considering each class of sediment independently, the sum of all suspended sediment concentrations is plotted on the figure. Most of the suspended sediment, however, is from the finer grains, and the coarsest sediment classes contribute little or none. Note that, sediment suspension seems to primarily occur at spring tides, and even then the amount of sediment suspended into the water column is not particularly large (with a maximum suspended sediment concentration of 0.0126 kg/m^3, or a volume fraction of only 4.75×10^{-6}).

After the initial model spin-up period, the pattern of mean grain diameter on the seabed achieves a quasi-steady state (Figs. 36 and 37). Note that, while little can be said quantitatively with respect to comparing these results to measured surficial sediment properties (Fig. 12), the general pattern appears to be the same. Also note that only the finest sands show any suspension in the SAMP study area, when only tidal forcing is applied, even though the sediment is disturbed with respect to its initial condition (Fig. 36, 37). The most substantial difference is east of Block Island, near PO-F and MD-F, where the measured median grain size is substantially coarser than that predicted. This region also corresponds to a shallower area (Cox Ledge; Figs. 9, 10, 13), however, suggesting that wave forcing may be the driving force in suspending

sediment in that area, whereas, in much of the rest of the ROMS domain, tidal forcing is sufficient to suspend the finer sediments.

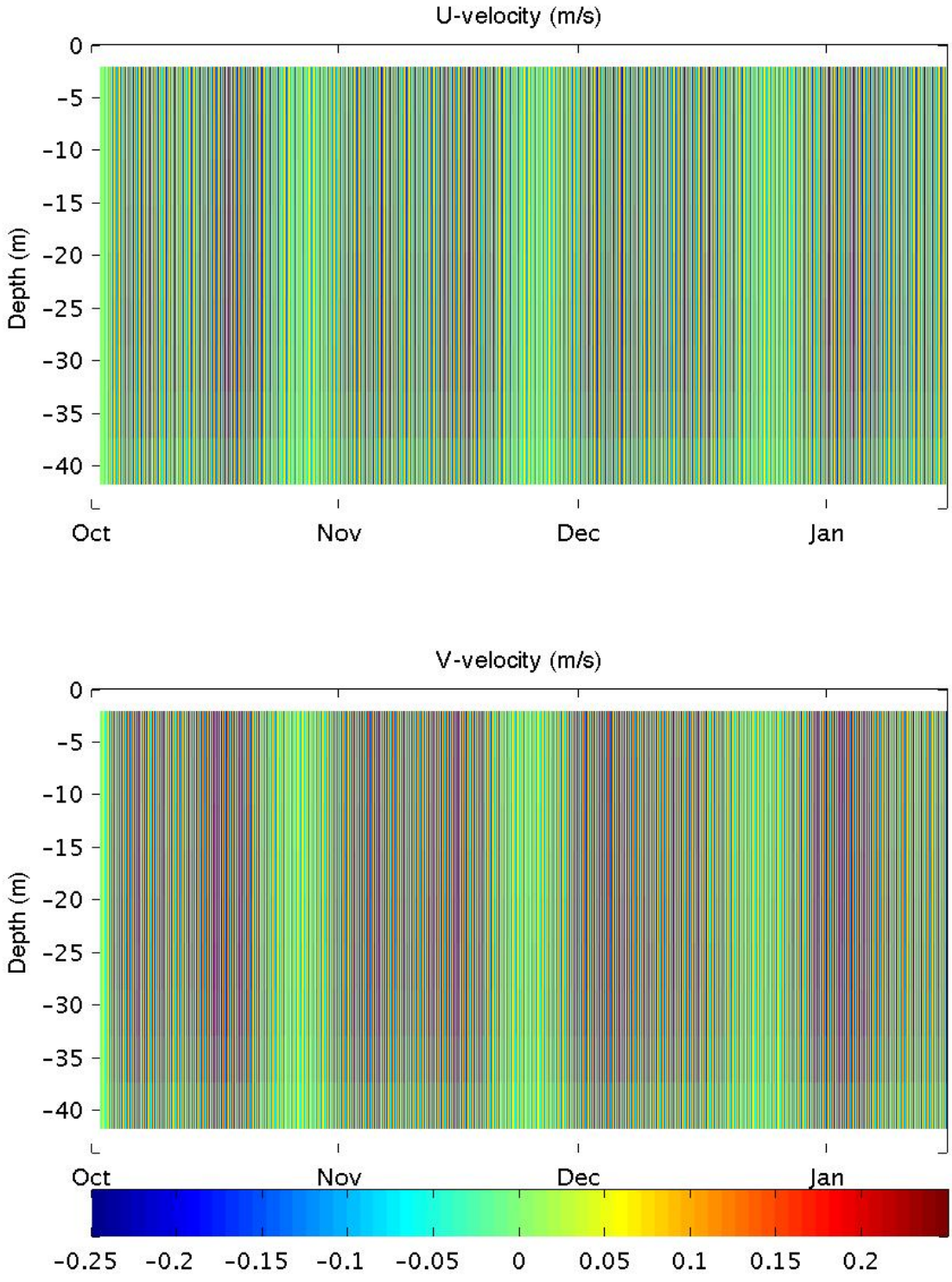

Figure 31. Current profiles (color in m/s) predicted by ROMS using only tidal forcing for PO-S (41.0482° N 71.5003° W). Note the lack of significant vertical gradients.

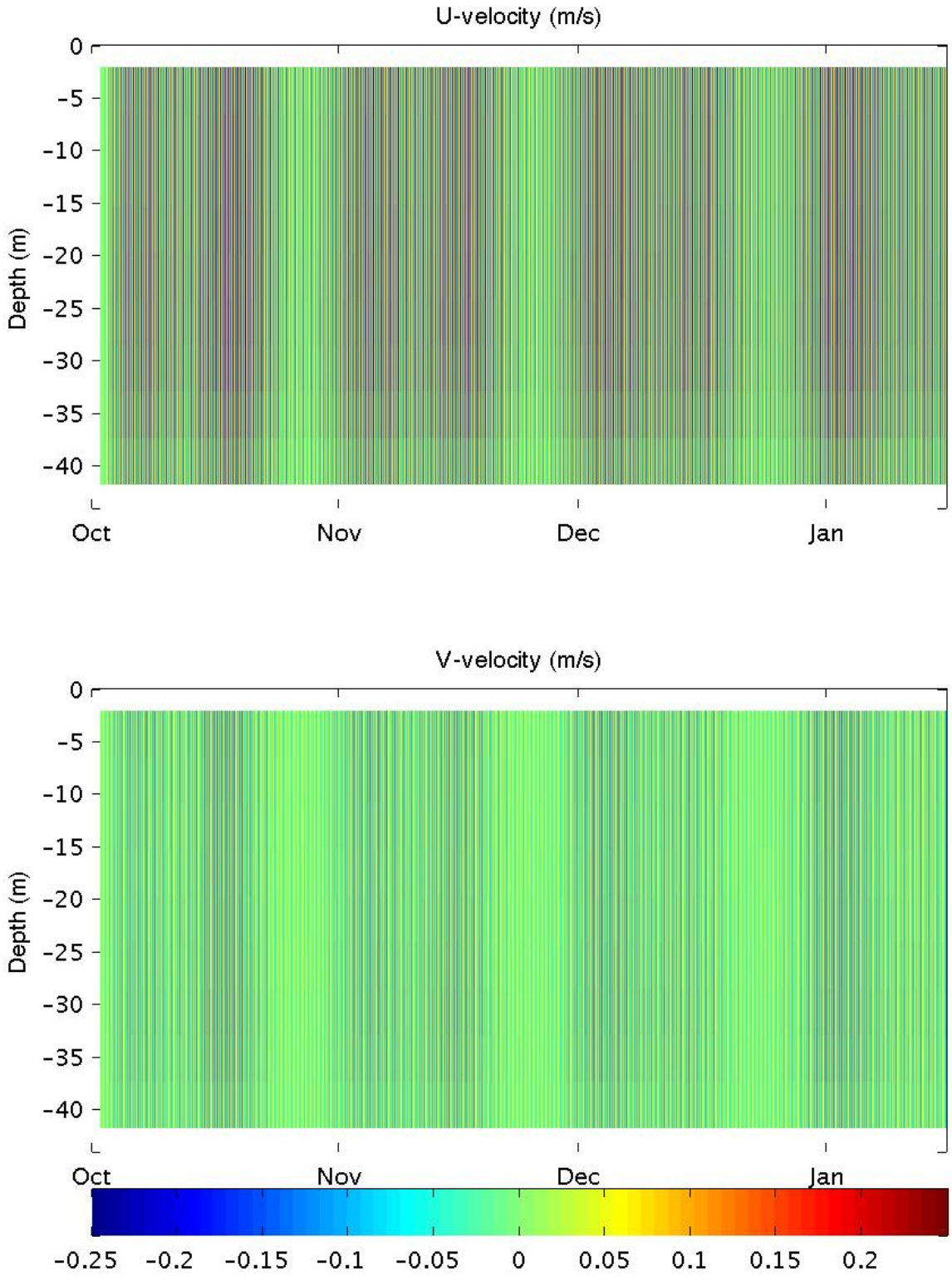

Figure 32. Current profiles (color in m/s) predicted by ROMS using only tidal forcing for PO-F (41.2500° N 71.0917° W). Note the lack of significant vertical gradients.

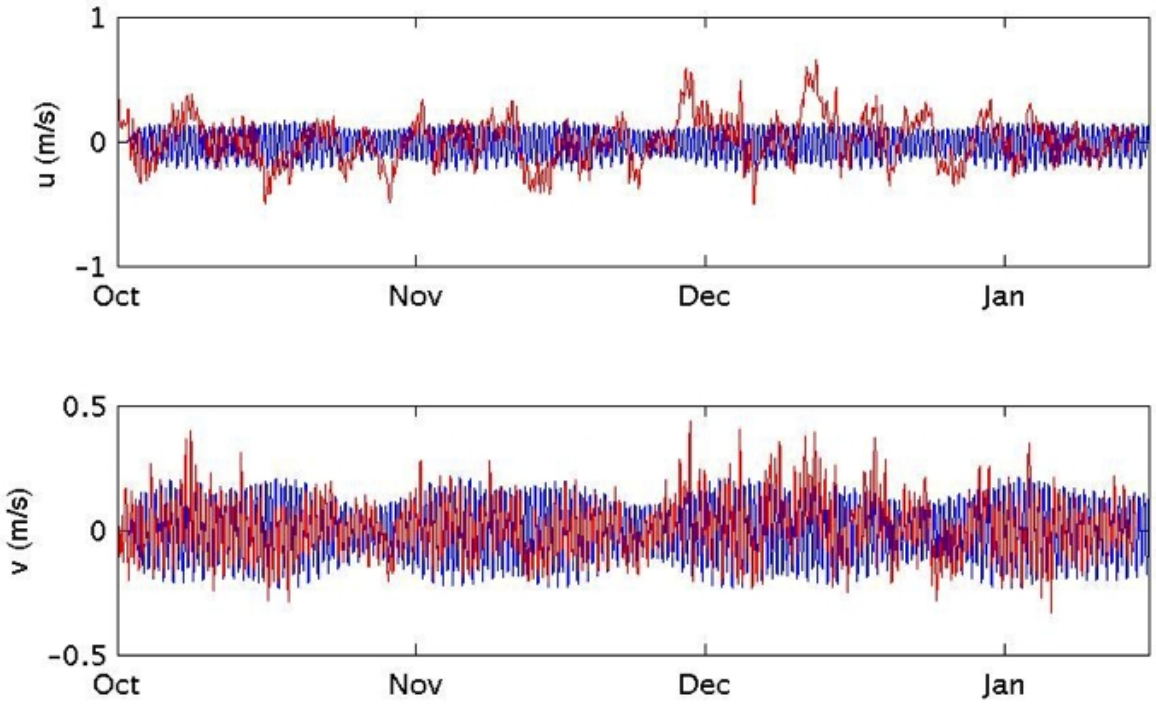

Figure 33. Time-series of current predicted by ROMS (blue) at 20 m depth, using only ADCIRC tidal forcing, for PO-S (41.0482° N 71.5003° W), and currents measured by ADCP (red) at the same location.

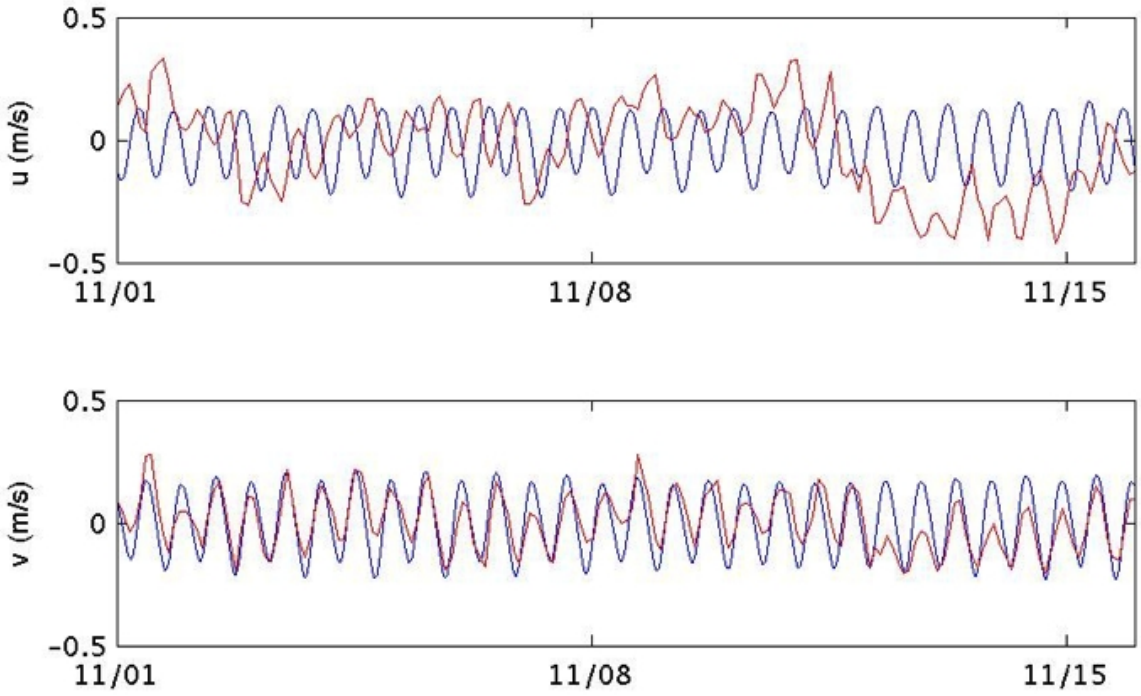

Figure 34. Zoom from Fig. 33.

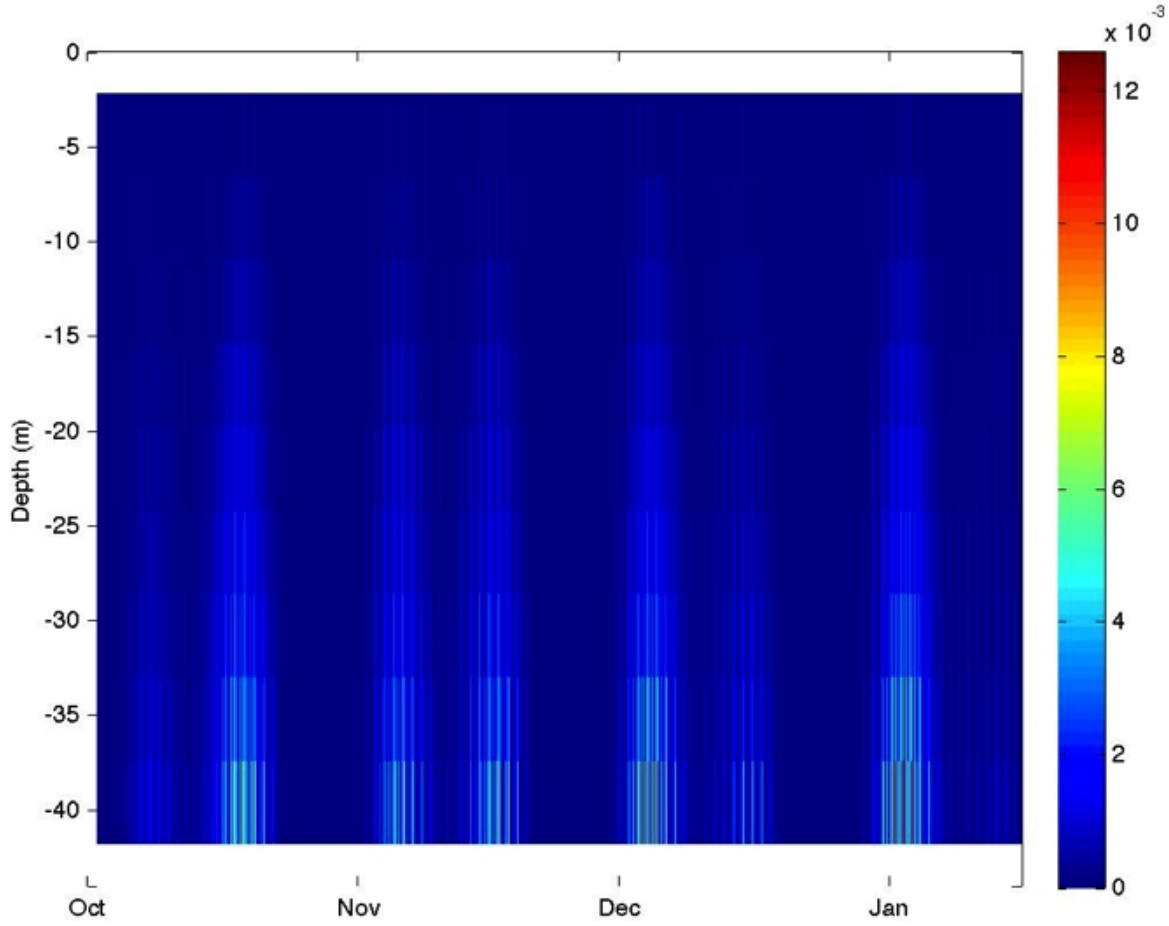

Figure 35. Suspended sediment concentration (color scale in kg/m^3; sum of all modeled grainsizes) over time, predicted by ROMS using only tidal forcing, at the PO-S station (41.0482^o N 71.5003^o W).

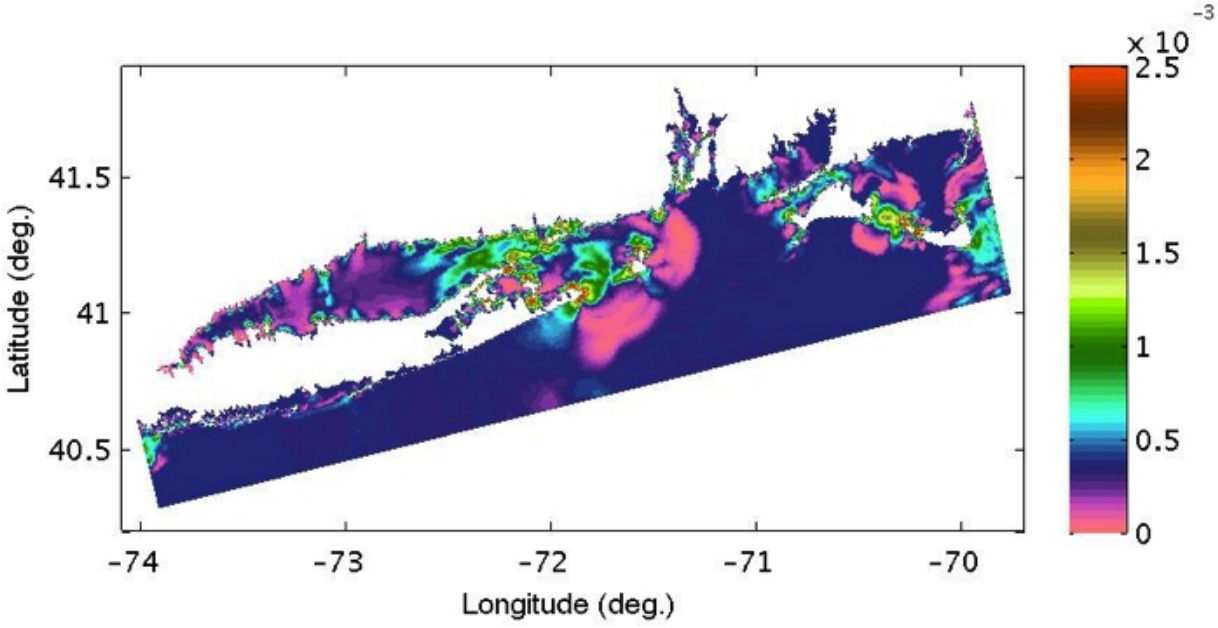

Figure 36. Median grain diameter (m) at the seabed after 107 days of simulated time with only tidal forcing.

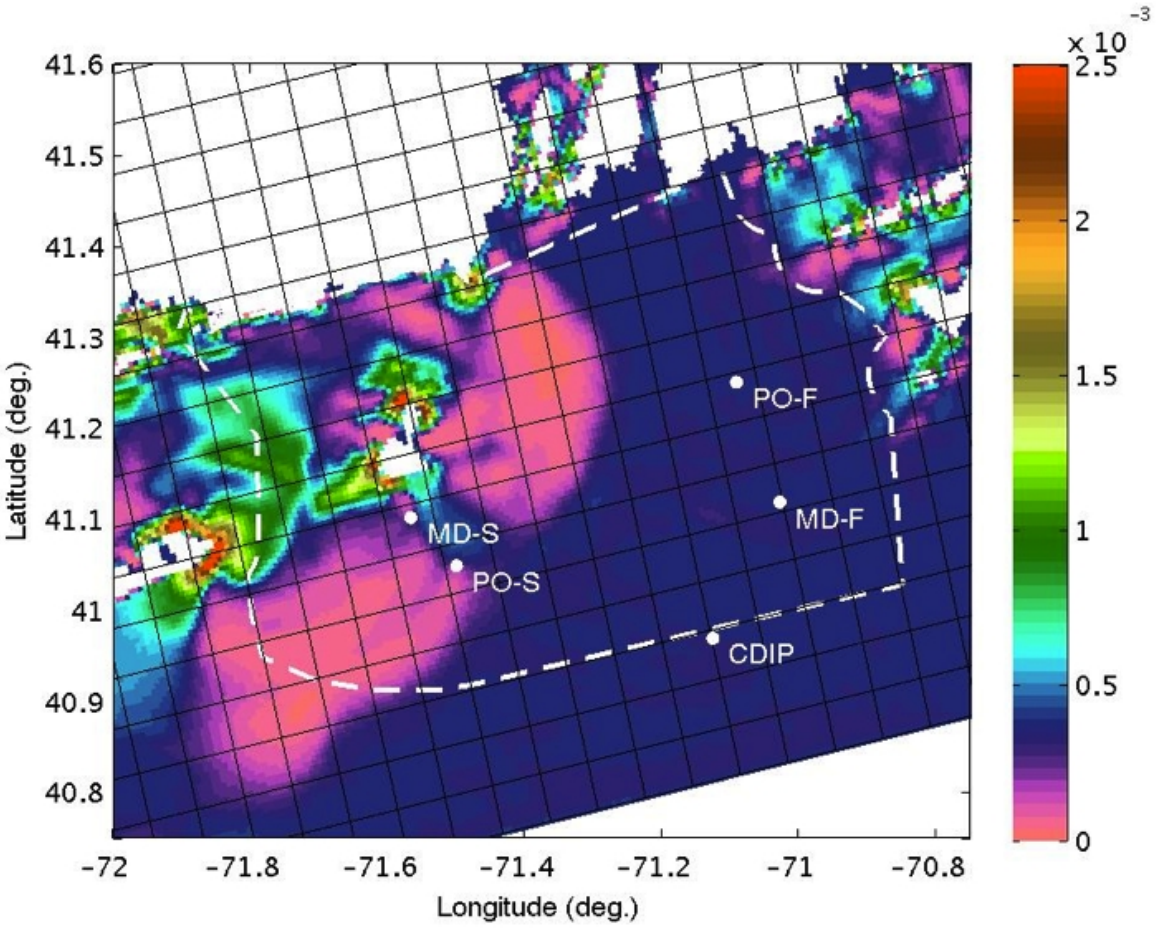

Figure 37. Median grain diameter (d_{50} in m) at the seabed after 107 days of ROMS simulations with only tidal forcing, including station locations, SAMP boundary (dashed), and model grid (black grid; each square is 6 km across, corresponding to 10x10 grid points in the high resolution simulations).

4.6.3 ROMS Simulation: Forced by Tides and Winds

After considering tidal forcing, it is instructive to consider adding in each forcing individually, next considering tidal and wind forcing.

Similar to the tidal elevation analysis for the tidally-forced simulation (Fig. 29), we can again show the model spin-up by again comparing the modeled elevation record to the modeled elevation record that matches the frequency of tidal constituents (Fig. 38). We again find that the difference between the two is small for most of the simulation time, although not as negligible as the tidally forced simulation. We can also note that the local elevation does not have as much subtidal variation as the actual observations (Fig. 27, 28).

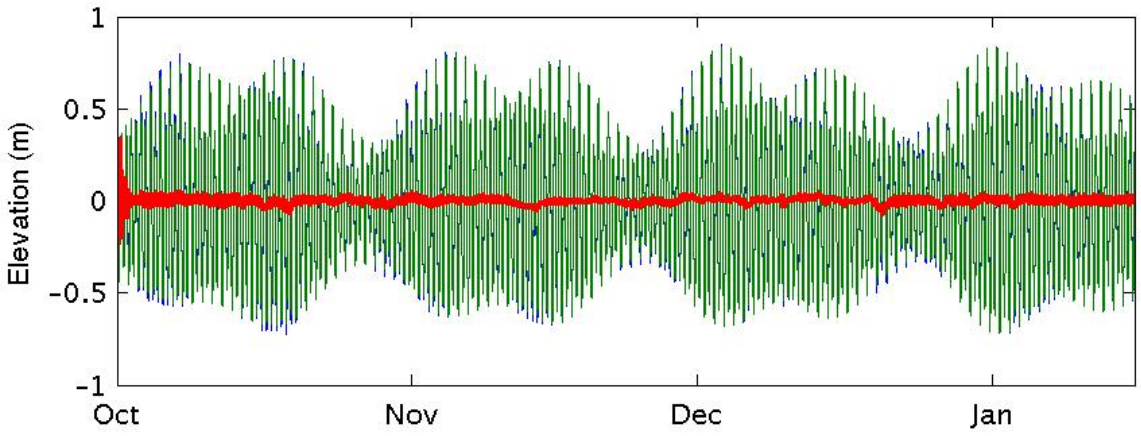

Figure 38. Surface elevation predicted by ROMS with tidal and wind forcing, at PO-S (41.0482° N 71.5003° W): modeled time-series (blue); predicted oscillations corresponding to tidal frequencies (e.g., M2, N2, K1, S2, etc.) (green); and differences between time-series and prediction (red). Note that the non-tidal transient of model spin-up subsides within a few days and quickly achieves a quasi-steady result.

In terms of velocity profiles, the results (Fig. 39, 40) qualitatively approximate the observed velocities better than before, as an additional important forcing term is included. Particularly note the strong eastward velocity mid-November at PO-S that is captured with the tidal and wind forcing and the observations, but not the only tidally-forced ROMS simulation. Again a time-series at 20 m depth can be considered at PO-S (Fig. 41, 42). Here the general variation is captured by the ROMS simulation.

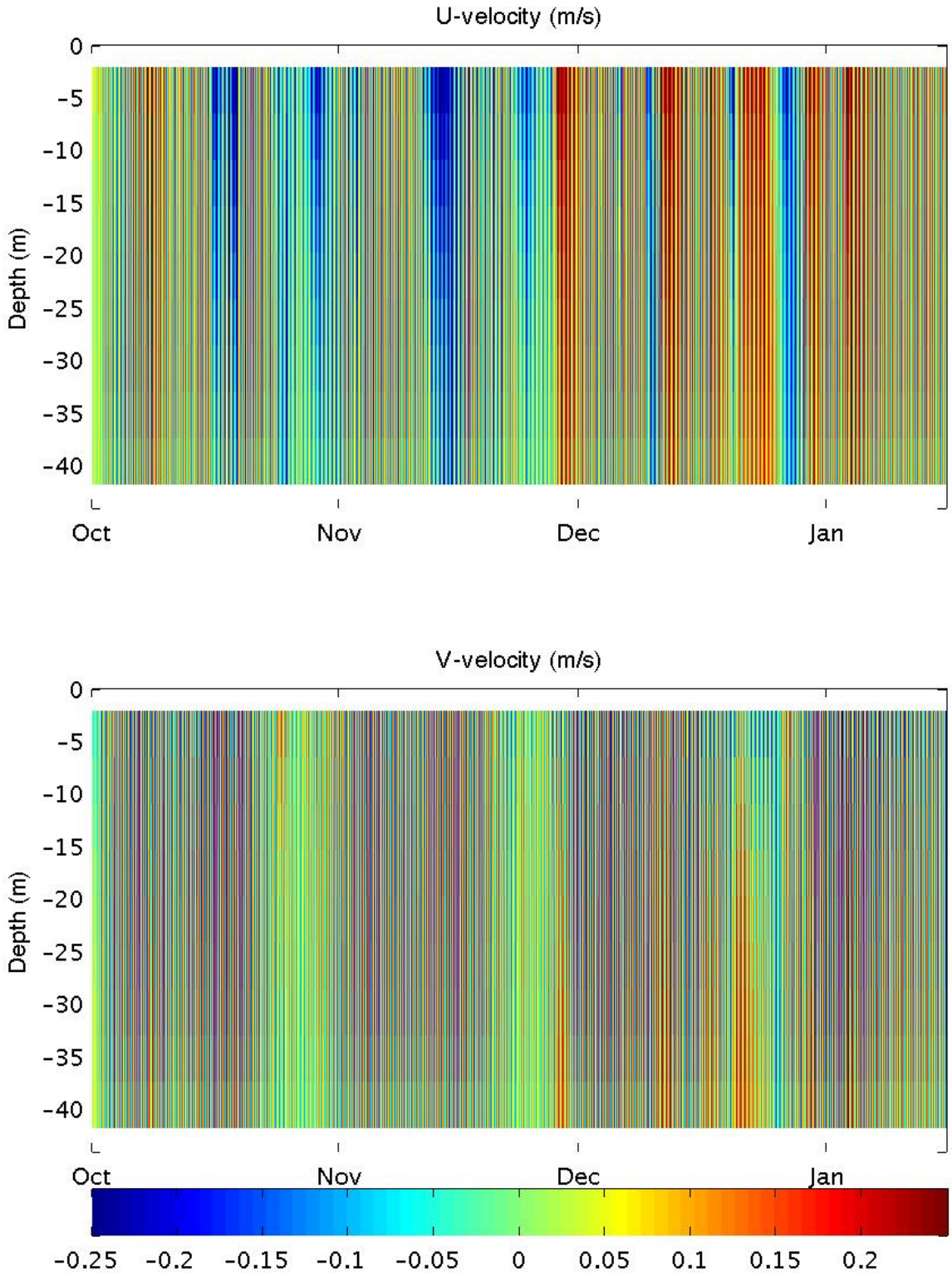

Figure 39. Current profiles (color in m/s) predicted by ROMS using tidal and wind forcing for PO-S (41.0482° N 71.5003° W).

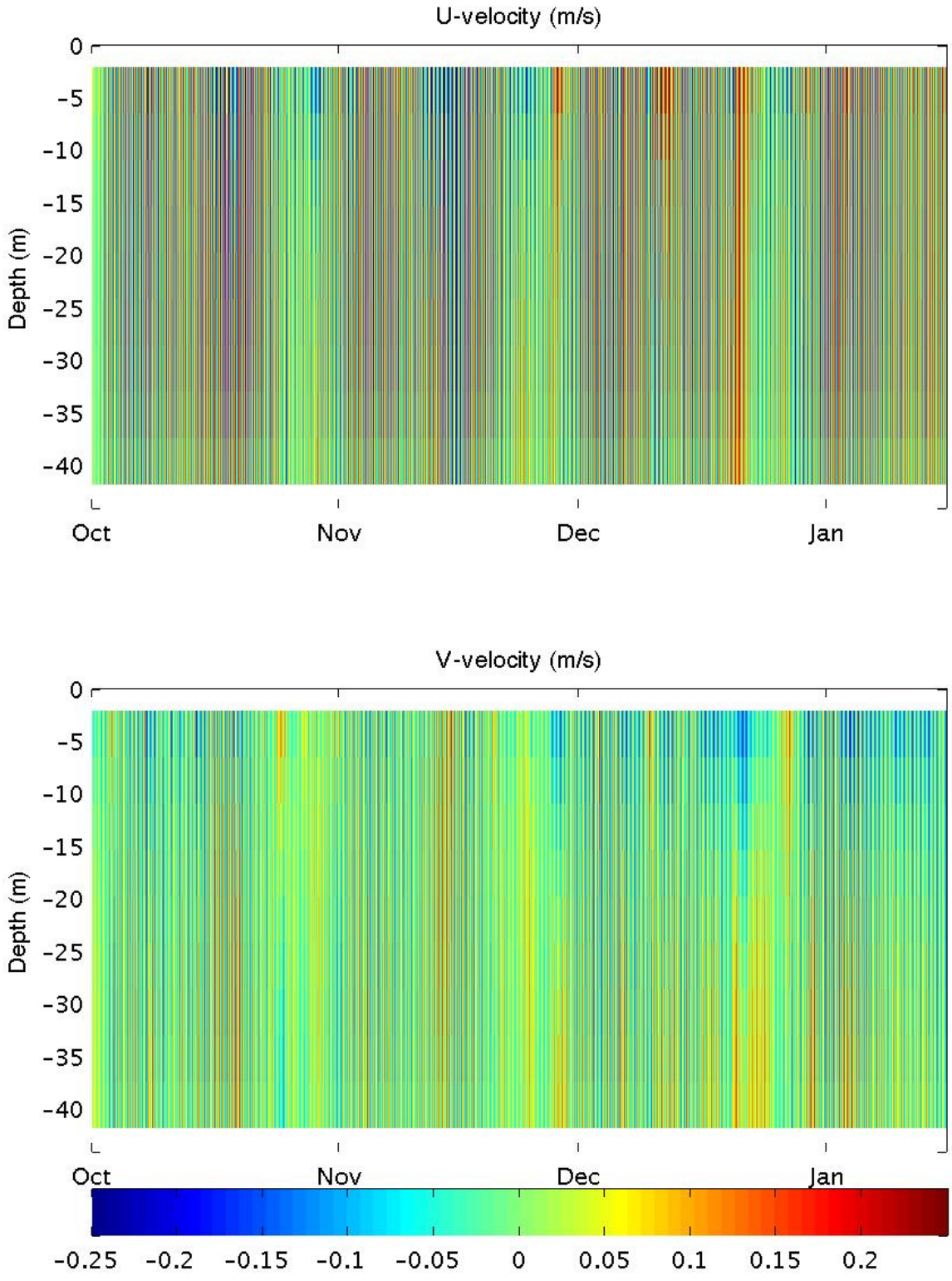

Figure 40. Current profiles (color in m/s) predicted by ROMS using tidal and wind forcing for PO-F (41.2500° N 71.0917° W.

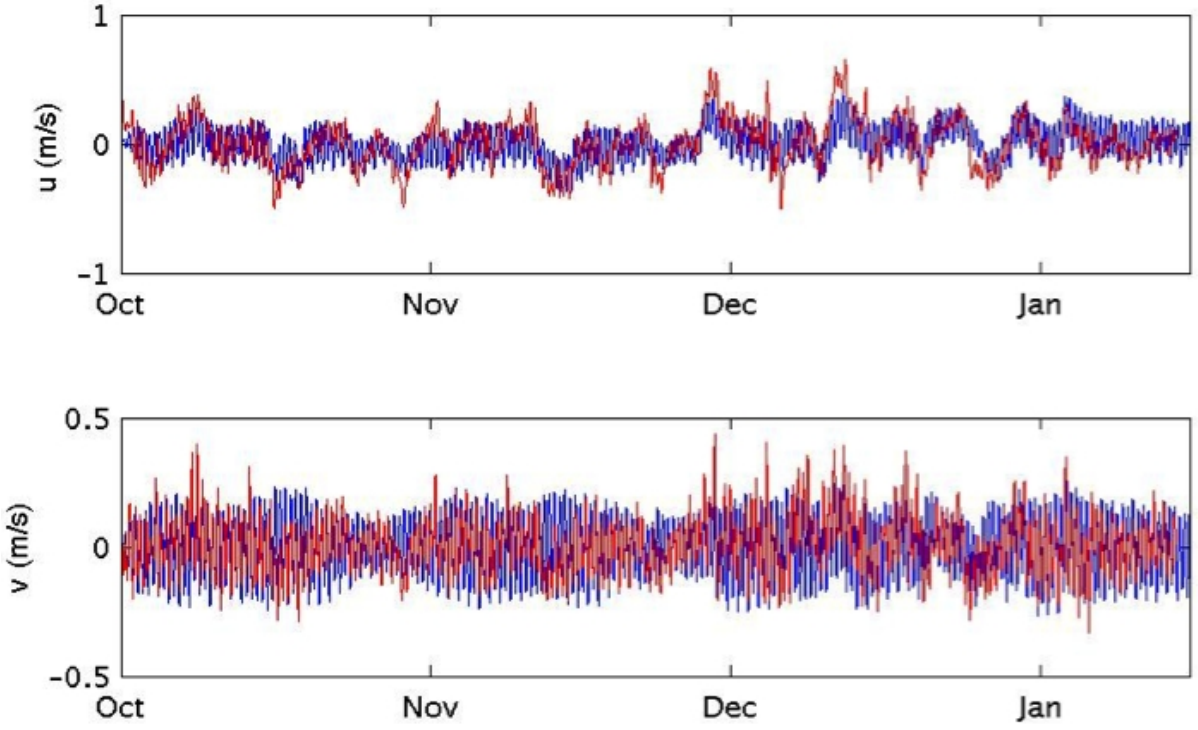

Figure 41. Time-series of current predicted by ROMS (blue) at 20 m depth, using tidal and wind forcing, for PO-S (41.0482° N 71.5003° W), and currents measured by ADCP (red) at the same location.

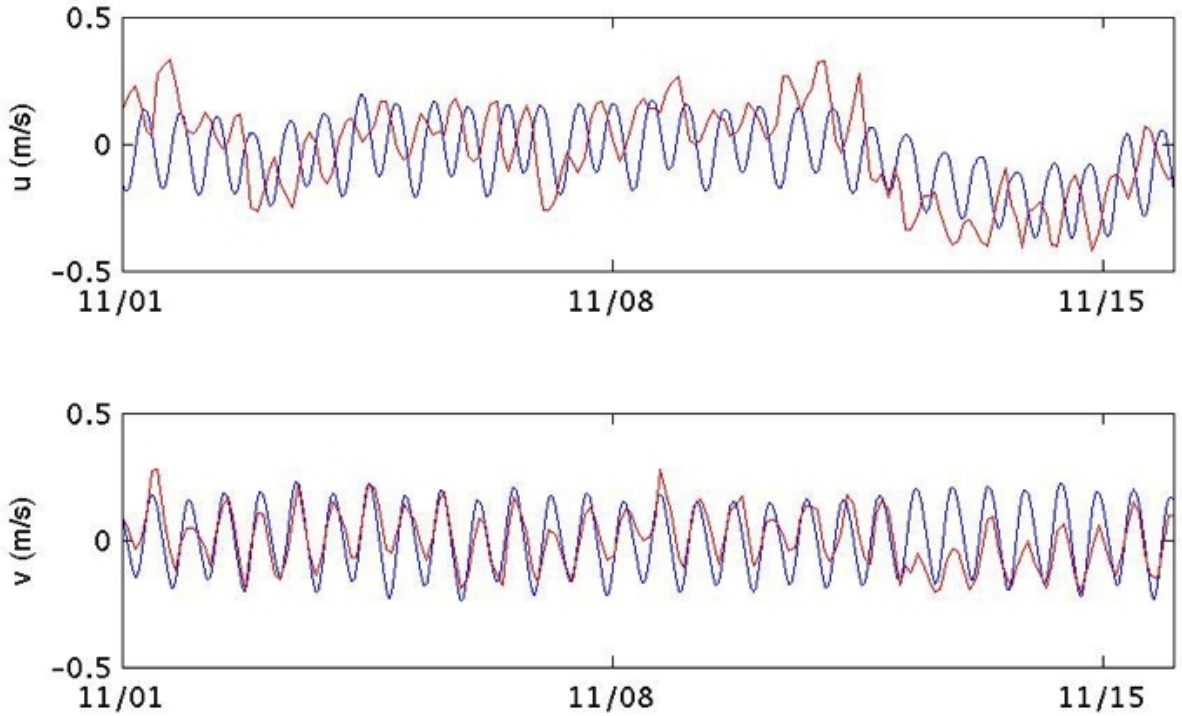

Figure 42. Zoom from Fig. 33.

Regarding suspended sediment, we find that the suspended sediment concentration at the PO-S buoy site (Fig. 43) better matches the observations than the only tidal simulation. Note that, sediment suspension seems to primarily occur at spring tides, and even then the amount of sediment suspended into the water column is not particularly large (with a maximum suspended sediment concentration of 0.0351 kg/m^3, or a volume fraction of only 1.32x10^{-5}). The largest discrepancy between the ADCP counts and the modeled SSC occurred during the mid-November storm.

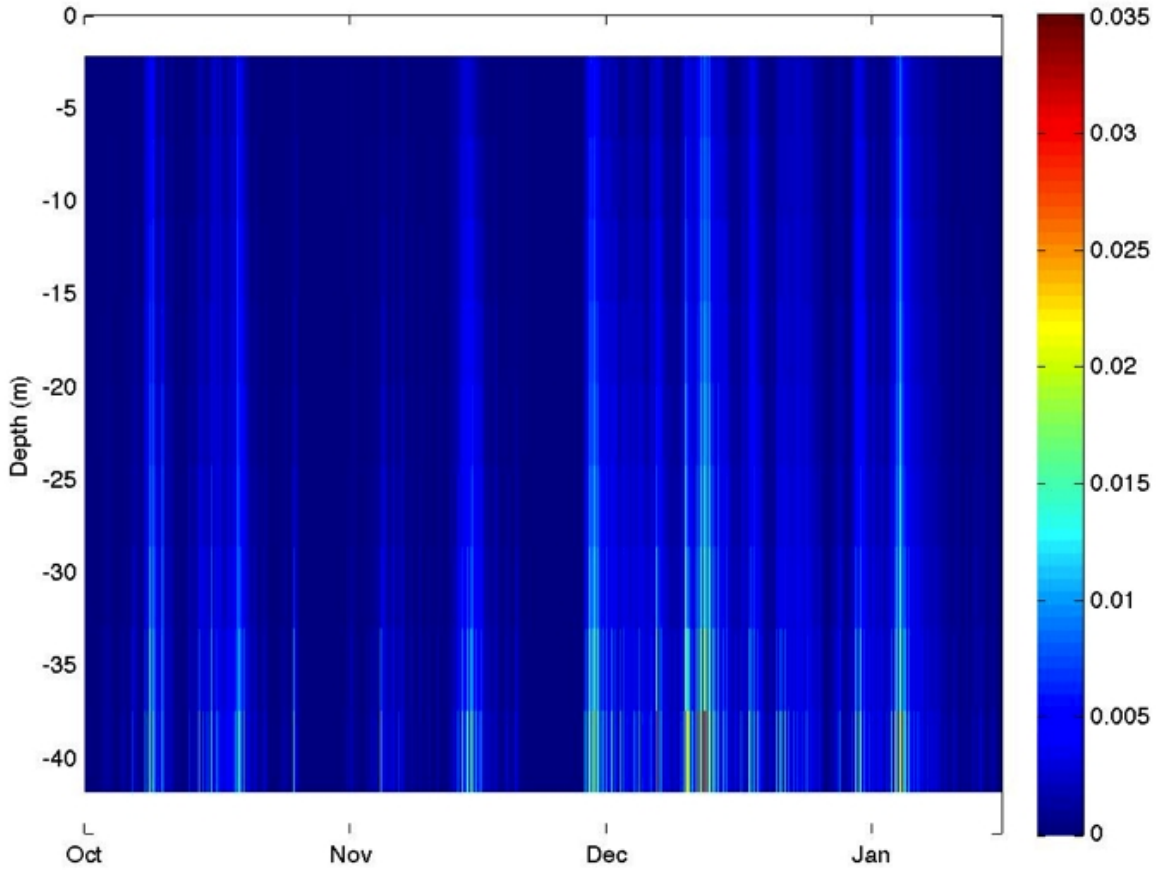

Figure 43. Suspended sediment concentration (color scale in kg/m^3; sum of all modeled grainsizes) over time, predicted by ROMS using tidal and wind forcing, at the PO-S station (41.0482^o N 71.5003^o W).

After the initial model spin-up period, the pattern of mean grain diameter on the seabed achieves a quasi-steady state (Figs. 44 and 45). Note that while little can be said quantitatively with respect to comparing these results to measured surficial sediment properties (Fig. 12), the general patterns appears to be the same, and a better agreement is found than with only tidal forcing, particularly around the shallow Cox Ledge (Figs. 9, 10, 13).

4.6.4 HYDROMAP Simulations: Forced by Tides and Winds

Appendix A provides the full report on this work, prepared by ASA, as part of their subcontract. Below is a summary of findings and then a comparison with ROMS tidal simulation results, for purpose of validation.

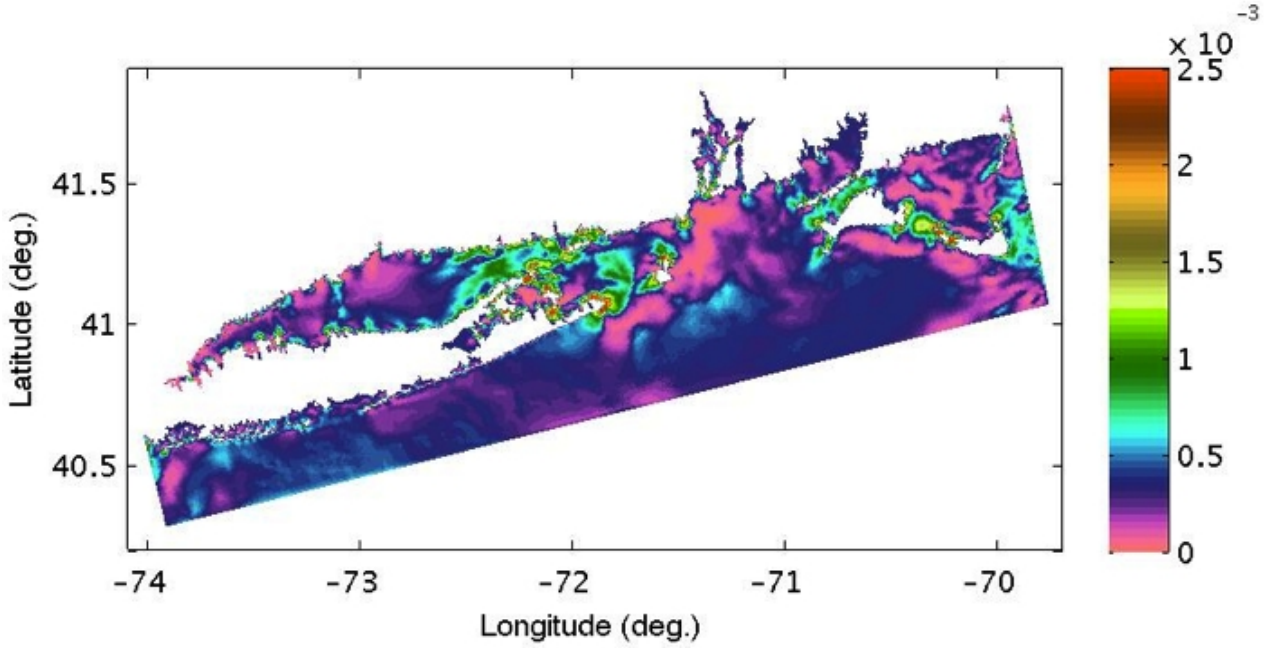

Figure 44. Median grain diameter (m) at the seabed after 107 days of simulated time with tidal and wind forcing.

Applied Science Associates, Inc. (ASA) performed a hydrodynamic modeling study focused on estimating the (mostly tide-induced) currents and circulation in the renewable energy (RE) development area with a focus on bottom stress and currents. ASA used the HYDROMAP model system, which calculates velocity vectors on a stepwise continuous variable rectangular grid system. A benefit of the model is that it allows coarse grid resolution in the areas offshore the coast of Rhode Island and finer resolution in the Block Island Sound area and renewable energy zone area of interest. The model was driven by tidal harmonic data along the open boundaries and constant wind stress at the surface. The model predictions were compared to observations collected as part of the SAMP field program, including four ADCP current meter locations and NOAA tidal elevation data at Montauk and Newport. The comparisons showed that the model not only adequately predicted the tidal forcing response in the study area, but also the longer period episodic wind driven events that are characterized by passing weather systems. The model appeared to be able to reproduce both the horizontal spatial variability in the system as well as

the vertical profile of the currents, as represented by the ADCP observations at the surface, mid and bottom of the water column.

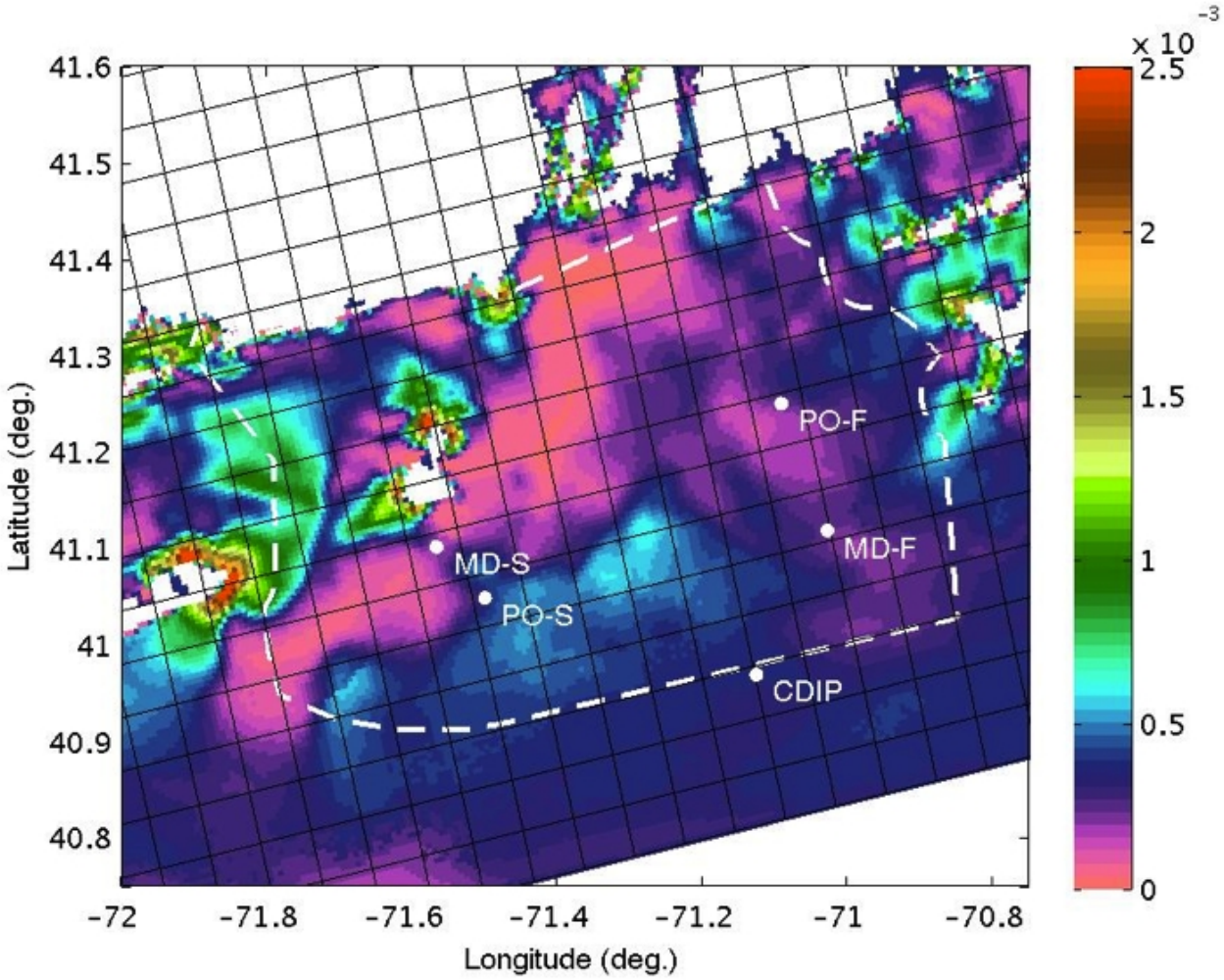

Figure 45. Median grain diameter (d_{50} in m) at the seabed after 107 days of ROMS simulations with tidal and wind forcing, including station locations, SAMP boundary (dashed), and model grid (black grid; each square is 6 km across, corresponding to 10x10 grid points in the high resolution simulations).

Both observations and model predictions confirm that the dominating tidal constituent is the M2 constituent, which represents between 50-60% of the total tidal amplitude at all stations. The amplitude predictions for all constituents tend to be higher than the observed but are generally within 20% of the observed with the exception of Montauk. The Montauk station is located in the shallows of an embayment that the mode grid does not resolve in fine detail, this may contribute to the over prediction of tidal amplitude.

Review of the current analysis indicates that the differences between model predicted and observed M2 constituent major axes are generally less than 0.02 m/s, with a maximum deviation

of 0.05 m/s in the MDF bottom current ellipse. The difference in the remaining constituents is variable, remaining less than 0.01 m/s for the majority. The M2 phase comparison between the model predictions and observations is similarly close, with the difference angle remaining less than about 10 degrees with an exception in the bottom currents at both the POS and POF stations. In general, the model predicted tidal current ellipses, driven predominantly by the M2 tidal component, show a close agreement with the observations indicating that the model captures the magnitude and the circulation patterns in the study area.

The bottom currents were further reviewed and an understanding of the bottom speed developed. The renewable energy zone follows the edge of the 3 mile state waters limit along the southern portion of the line, from the straights between Long Island and Block Island to the west, to the shipping channel exclusion zone on the east. The zone is approximately 2 km wide, and has a bulge on the east side representing the shipping channel exclusion zone. Bathymetry in the RE zone is quite variable ranging from less than 10 m, in the western portion to greater than 35 m to the east. This bathymetric range and the straights to the west produce a significant variability in the bottom current speeds as well, ranging from a high in the shallow western portions of 0.25 m/s down to a high in the eastern portions of 0.15 m/s.

4.6.5 ROMS Simulations: Forced by Tides, Winds, and Waves

Because of the limitations in modeling the observed hydrodynamics of the SAMP study area when only using a tidal forcing, as described above, additional forcing terms need to be included. When wave and realistic wind forcing terms are included, a number of significant differences are noted.

The first distinction is in the current profiles (Fig. 46), which are not nearly as vertically homogeneous as the earlier tidal simulations. One can then see that (unlike Fig. 31), and more similar to the observed data (Fig. 25), there is at times significant vertical variation in the velocity field. The addition of the wave forcing, in combination with a bottom boundary layer model (*ssw_bbl*), which takes into account the added seabed stress induced by surface waves, results in more sediment being suspended (Fig. 47).

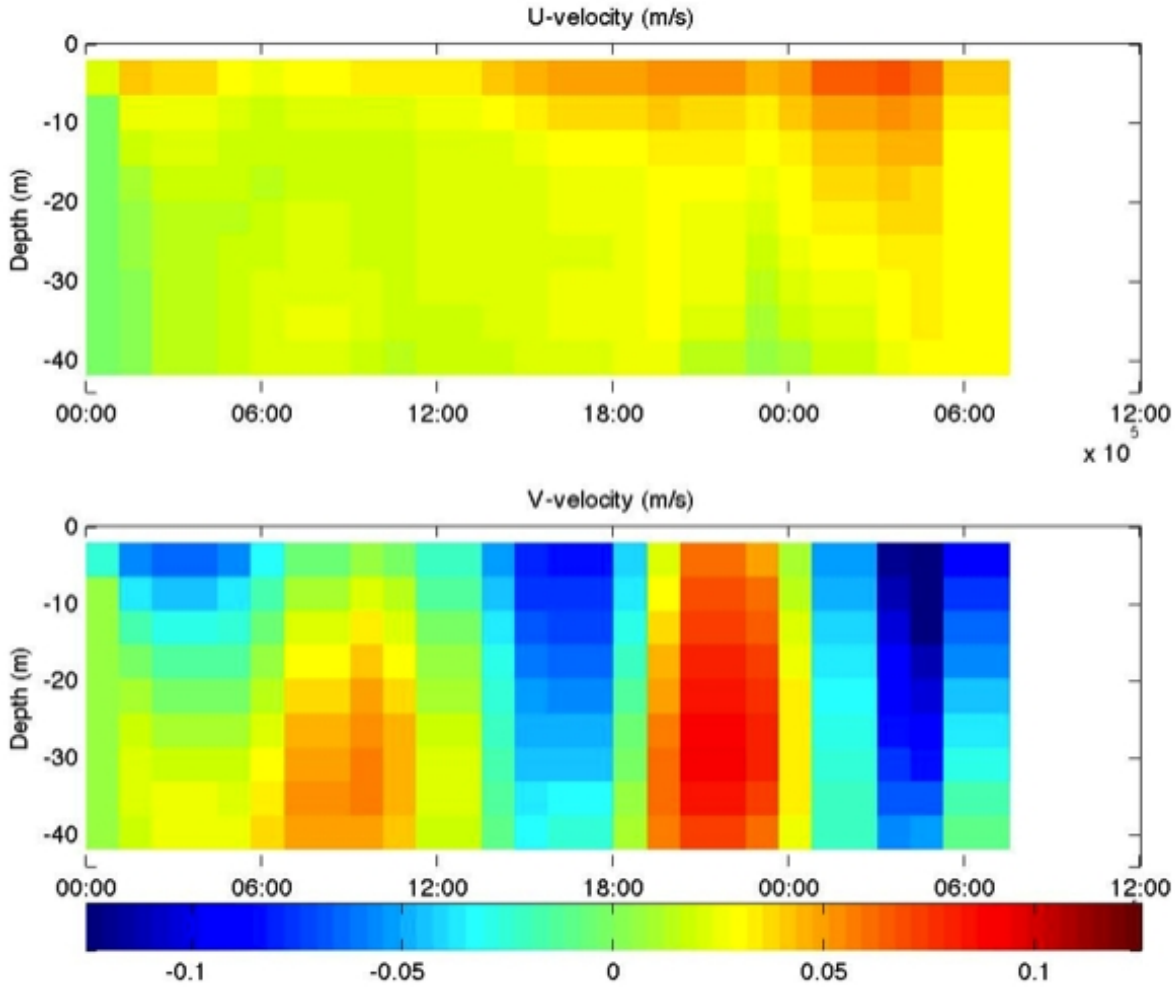

Figure 46. Current profiles (color in m/s) predicted at the start of a coupled ROMS/SWAN simulation using tidal, wave, and wind forcing for PO-S (41.0482° N 71.5003° W). Note, the vertical structure of the currents, in contrast to the ROMS simulations, which only considered tides.

One of the best records of the sediment characteristics in the SAMP area is the map of median grain size (Fig. 12). The tidal ROMS simulations mentioned earlier (Figs. 34, 35) qualitatively show many, but not all, of the same features as the observed map. In general, however, the coupled ROMS/SWAN simulations are able to obtain a better agreement (Figs. 48, 49). One of the most substantial differences is that the coupled ROMS/SWAN simulations show coarser sediment in the eastern half of the SAMP area (around PO-F and MD-F). This is likely caused by the added seabed stress due to waves in the shallower waters in that area (see Fig. 13).

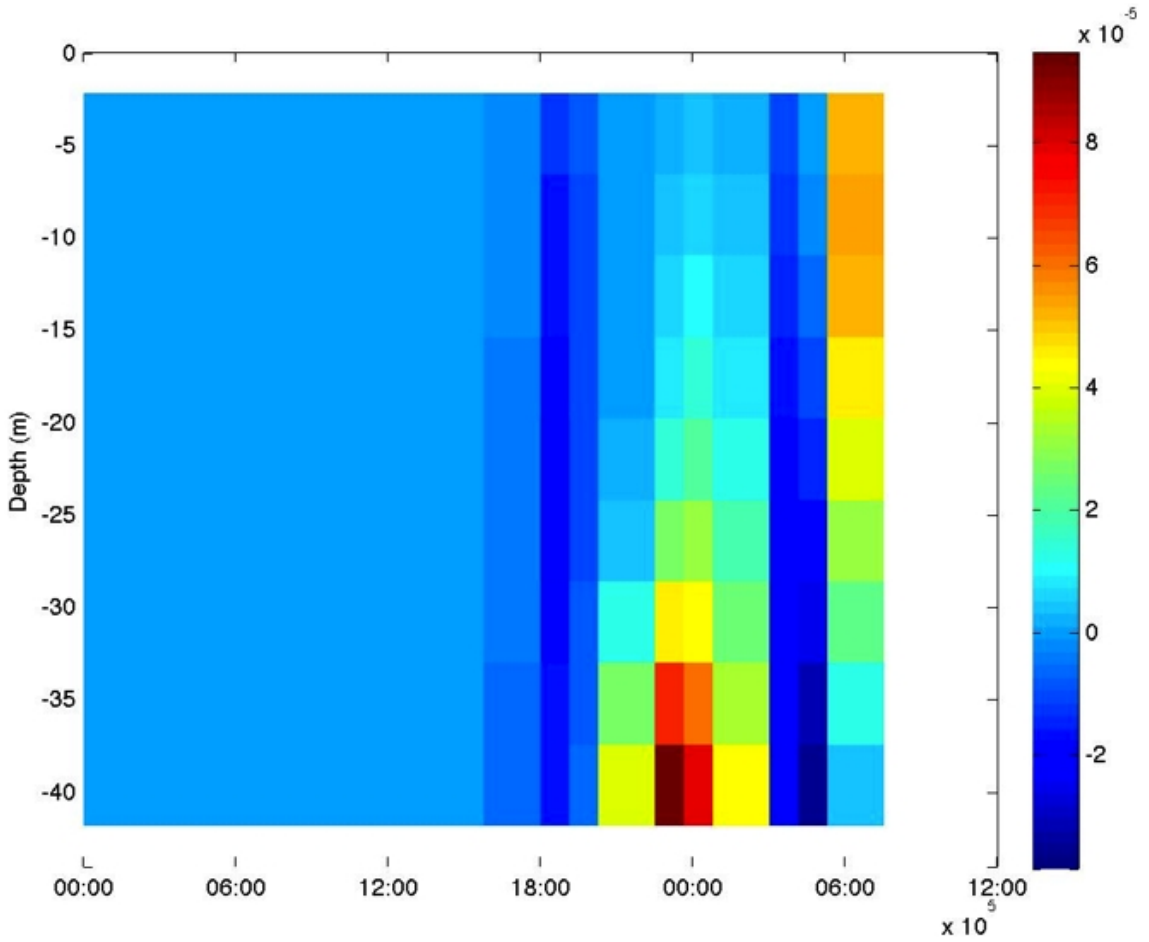

Figure 47. Suspended sediment concentration (color scale in kg/m^3; sum of all modeled grain sizes) over time, predicted at the start of a coupled ROMS/SWAN simulation using tidal, wave, and wind forcing at the PO-S station (41.0482^o N 71.5003^o W).

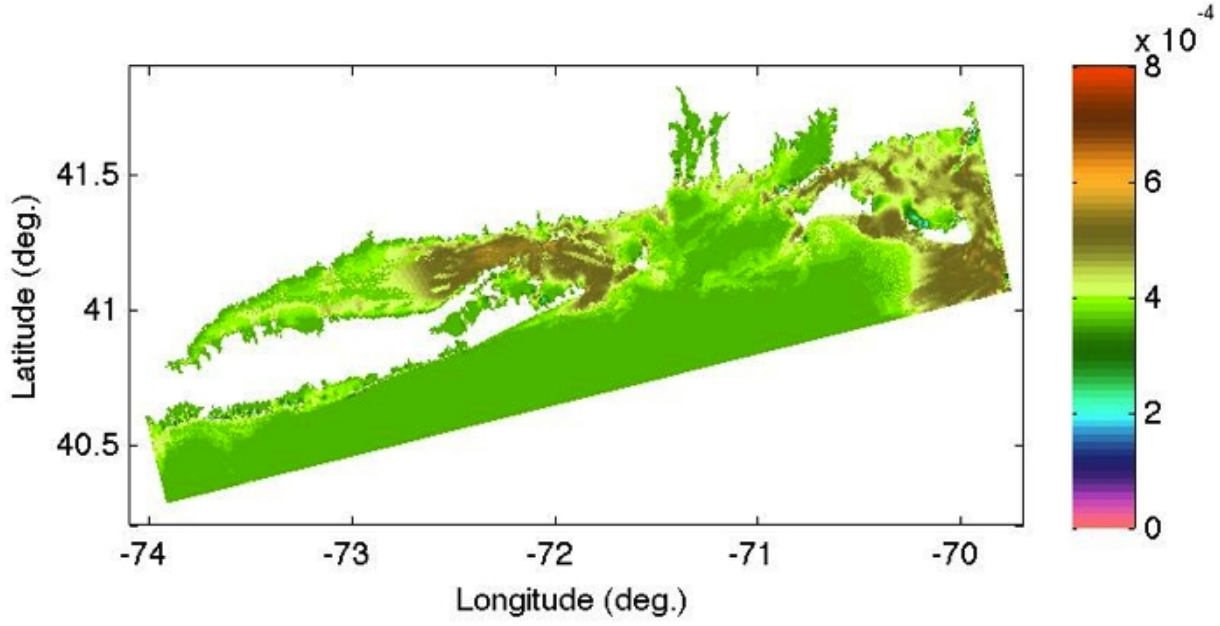

Figure 48. Median grain diameter (m) at the seabed after 1 day of simulated time with tide, wave, and wind forcing.

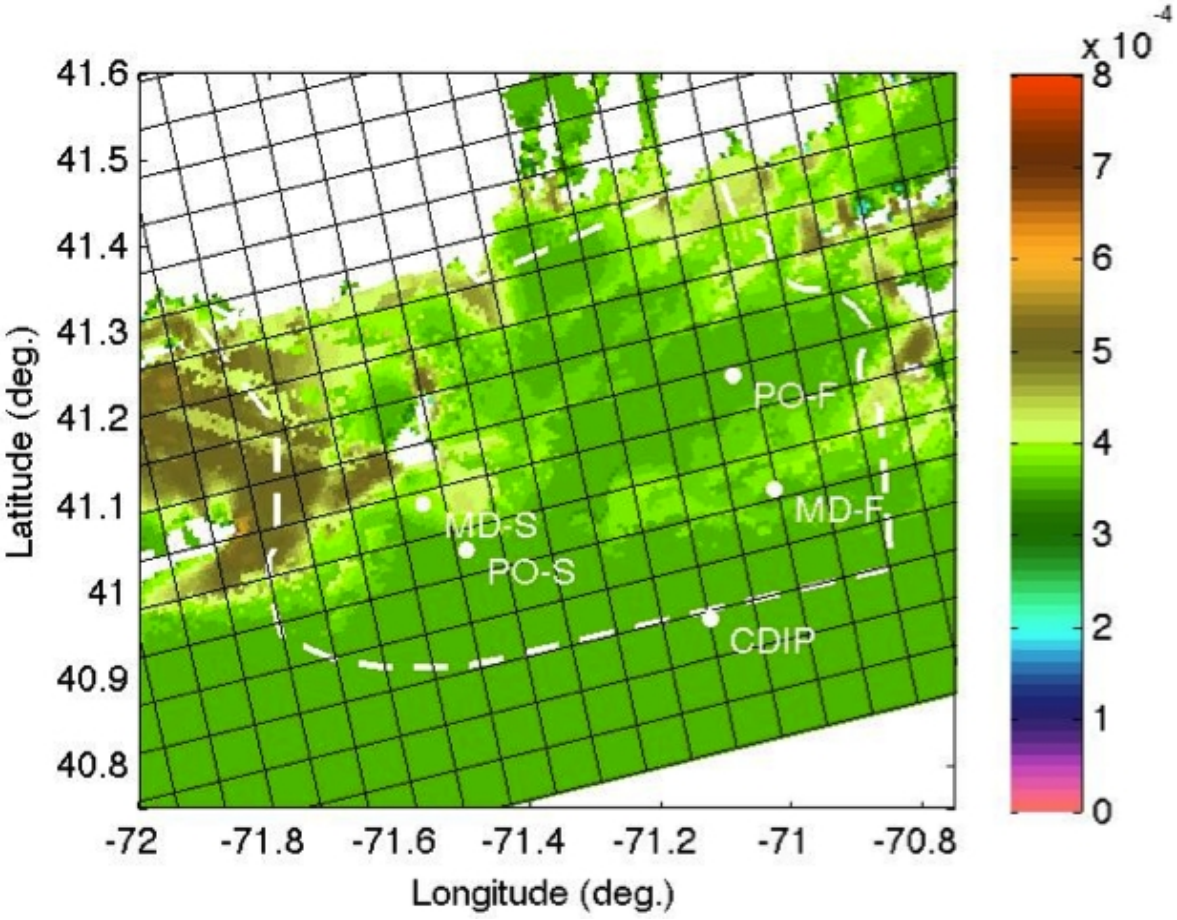

Figure 49. Median grain diameter (d_{50} in m) at the seabed, after 1 day of coupled ROMS/SWAN simulations with tidal, wave, and wind forcing, including station locations, SAMP boundary (dashed), and model grid (black grid; each square is 6 km across, corresponding to 10x10 grid points in the high resolution simulations).

5 Discussion

5.1 Implications of buoy measurements

The vertical profiles in Figs. 25 and 26 clearly show that there is a distinct layer in the upper 5 m. While the large measured surface layer velocities may be in error due to side lobe reflection of the ADCP signal off of the surface, note that there is minimal vertical variation for much of the time over the rest of the water column. One suggestion might be that this is a layer, which is distinct due to density differences, and while the current ROMS simulations do not include density-driven circulation, Codiga and Ullman (2010) analyzed FVCOM simulations of the southern New England shelf for 2006 in the fall, and found stratification was most significant deeper (i.e., at 20 m). Neglecting inter-annual variations in stratification, this suggests that density is not a fundamental driving force of the currents in the area in the autumn.

Overall, the buoy data suggests several things about the hydrodynamics of the area. On time-scales of weeks, at least in the fall, density-driven circulation is not critical to the understanding of the SAMP study area hydrodynamics. The ever-present tidal currents are of the same magnitude as the instantaneous currents, and their effects can be seen throughout the water column, but they are likely not the dominant force for suspending sediment. The latter appears to result from episodes of large (and long) storm waves.

5.2 Velocity profiles in ROMS simulations and ADCP data

In general, the observed ADCP velocity profiles (Fig. 25, 26) can be described as lacking significant vertical variation (except perhaps at the very surface or bottom of the water column, where noise interferes with quality measurements), and seemingly being tidally dominated except at various storm events.

All of the ROMS simulations show similar velocity magnitudes, although clearly tidal forcing alone is not sufficient to capture the variations in velocity (Fig. 34). When additional forcings are included, however, qualitatively the simulated velocity variation matches observations well (e.g., Fig. 41).

5.3 Comparison of ROMS and HYDROMAP tidal simulations

In general, the results of ROMS and HYDROMAP are found to be in good agreement. For example, the M2 amplitude (the dominant tidal forcing component) at station PO-S was predicted by ROMS to be 0.494 m, and HYDROMAP predicting 0.478 m. Similar errors were found in both magnitude and phase angle of the tidal constituents.

A number of significant differences, however, exist between how ROMS and HYDROMAP were set-up, beyond the differences in numerical methods, including the forcing terms, the grid, and the focus, which explains why those two sets of tidal simulations may differ in some details. For ROMS, simulations discussed above only considered a tidal forcing from the ADCIRC data base of tidal constituent data along the east coast of North America, whereas the HYDROMAP set-up used the TPXO global tidal model data. The HYDROMAP set-up also included the effects of winds and was thus able to show better agreement with the current profiles – this deficiency in the ROMS setup is alleviated in simulations reported in the next section, where wave and wind forcing is applied to ROMS in addition to tidal forcing, but as well it is difficult

to separate the effects of waves and wind from the available data, because of the correlation between high waves and strong winds. One limitation of the HYDROMAP wind forcing was that it involved using a spatially uniform, albeit time-varying, wind field, obtained from measurements made at a single buoy. It is not clear how significant the spatial variation of the wind field is, but it is worth noting nevertheless, because the computational domains are large enough (e.g., the ROMS domain is 360 km across), that significant variations in the wind field are present. In ROMS simulations reported in the next section, by contrast, we use the full wind field hindcast using RAMS, varying over both space and time.

In terms of gridding, HYDROMAP used a nested grid, which increased in resolution around Block Island, down to 125 x 125 m cells. This is nearly 5 times higher a resolution than in the ROMS simulations. It would require significant computational resources to conduct multiple ROMS simulations over such time periods, using a uniform 125 m grid, so the nested approach is advantageous here. [Although it is possible to use nested grids with ROMS, that approach was not implemented here.] Some results not mentioned in this report show possible advantages of using HYDROMAP for tides: the ROMS results for coastal tidal stations (e.g., Newport, Montauk) were substantially different from observed data, yet HYDROMAP results were closer to the observed results. This is most likely because HYDROMAP uses a nested grid and so was able to resolve the important features of nearshore bathymetry, whereas the ROMS grid had a resolution of 600 m everywhere. However, ROMS results for tidal forcing should be sufficiently accurate in the deeper waters around the tentative wind farm sites in the SAMP areas.

Although the HYDROMAP simulation was able to more easily capture the behavior of the observed velocity structure, it did not consider the effect of surface waves or compute what sediment suspension would be, which both are important effects. In addition to the importance of modeling surface waves and sediment transport, in order to obtain meaningful information about sediment suspension, both can significantly affect seabed drag.

In closing, it appears that the independent HYDROMAP simulations have served their purpose well in showing that the more complete and comprehensive, but less resolved, ROMS simulations provide sufficiently accurate results for the key component of tidal forcing (M2) in the SAMP area.

5.4 Sediment suspension in the ROMS and ROMS/SWAN simulations

There are two sets of observed data that relate directly to sediment suspension in the SAMP study area: the map of median grain size (Fig. 12) of the surficial sediments which shows the seabed conditions, and the recording of ADCP backscatter at PO-S (Fig. 29) which may relate to the suspended sediment concentration.

For the seabed grain size diameter (Fig. 12), we note that in general offshore of the SAMP study area sediments are very fine with little variation. Around the SAMP study area, there are areas of coarser sediment (in excess of 2 mm diameter) at the mouth of Long Island Sound to the west, near Martha's Vineyard to the east, and around Block Island there are large variations between very fine and very coarse sediments. As well, there are very coarse sediments on Cox's Ledge, which is east of Block Island, where the water is shallow.

In the ROMS simulations with only tidal forcing, we observe many of these features around Block Island and Long Island Sound. [The lack of a quantitative match is not necessarily detrimental to the simulations, but rather the initial conditions, whereby using a uniform distribution of sediment classes with exponentially varying grain size will result in an abnormally low median value.] In order to get significant sediment transport in the eastern half of the SAMP study area, the wind forcing is required (Fig. 45), although with only tides and wind forcing, the region of coarser grain size is much smaller than in the observed (Fig. 12). In the ROMS/SWAN simulation with all three forcings (tides, waves and winds), the median grain size is most realistic, with coarser sand at the mouth of Long Island Sound, as well as on Cox's Ledge, with significant variation around all of the SAMP study area.

Regarding suspended sediment, ADCP backscatter suggests that sediment is suspended the most when the local waveheight is highest, most notably at events in mid-November, and in several smaller storms in December. When only tidal forcing is considered (Fig. 35), sediment suspension occurs primarily at the spring tides, not lining up very well with the ADCP backscatter measurements. When winds are included (Fig. 43), higher suspended sediment concentrations are predicted, although the large storm event in mid-November is does not result is as much sediment suspension as that in December, since the distinguishing feature between the two is the significant wave height, so a wave model coupling is required to better match the observations.

6 Conclusions

Results are presented for simulations of the hydrodynamics and sediment suspension in the ocean SAMP study area. In order to validate the models against observations, a period of three and a half months (October 2009 to mid-January 2010) was selected. A selection of tidal, wind, and wave forcings were considered, ignoring density-driven circulation. The Regional Ocean Modeling System (ROMS) was the primary modeling tool for conducting these simulations, but ROMS results were also compared to HYDROMAP simulations conducted by ASA for tidal and space-uniform wind forcing, and coupled ROMS/SWAN simulations were used to model coupled ocean-wave processes. Data was primarily compared against ADCP measurements of the currents obtained at four different buoys as part of the SAMP field program, as well as significant wave height.

Improvements to the numerical modeling could be made by increasing horizontal resolution, as well as tuning the vertical stretching parameters to better capture the surface and bottom boundary layer processes. Future work could better test result sensitivity to boundary conditions and the turbulence closure scheme, ensuring that the amount of suspended sediment is approximately correct. It may be possible to include effects of density-driven circulation, but as this work shows, at least for the Fall season, density-driven circulation does not appear necessary to explain many aspects of sediment suspension. Improvements could also be made on the measurement side, in particular by attempting to make a meaningful estimate of suspended sediment concentrations, from records of ADCP counts.

ROMS simulations with only tidal forcing were able to predict the tide elevation and currents in the SAMP study area, with good agreement with observations (and with higher-resolution HYDROMAP simulations). These simulations, forced only by tides, were also able to model sediment transport over the computational domain, and an initially uniform grain size distribution was shown to evolve to one qualitatively approximating the observed grain size distribution on the seabed. Comparing model results with observations, however, highlighted the importance of non-tidal currents in the area and of adding the other forcing terms from waves and wind.

HYDROMAP simulations of the area, for tidal and (uniform) wind forcing, using nested grids with a much higher resolution in some areas (down to 125 m), were used for comparison with ROMS tidal simulations. HYDROMAP results showed similar agreement with observed tidal elevations. In addition, obtained current profiles matched the ADCP observations better than the

initial ROMS simulations, which only considered tides, stressing the importance of wind forcing. The HYDROMAP results had several significant limitations, though, most significantly in neglecting waves and all sediment transport, and using a spatially uniform wind. They however served their purpose well in validating the coarser resolution (uniform 600 m grid) ROMS simulations of the key tidal components (e.g., M2) in the SAMP area.

Coupled ROMS/SWAN simulations in the SAMP area were conducted with tidal, wave, and wind forcing. The main difference seen between the ROMS/SWAN results and the earlier ROMS and HYDROMAP simulations is the improved agreement with available data regarding sediment grain size at the seabed. Although the 600 m resolution of the ROMS/SWAN grid does not show details as well as the HYDROMAP results, these coupled results show good agreement with available data regarding the hydrodynamics and seabed properties for the area.

7. References

Apsley, D.D. and I.P. Castro 1997. Flow and dispersion over hills: Comparison between numerical predictions and experimental data. *J. Wind Eng. Ind. Aerodyn.* 67: 375-386.

Asher, T.G., A.R. Grilli, S.T. Grilli and M.L. Spaulding 2010. Analysis of extreme wave climates in Rhode Island waters south of Block Island, Ocean Engineering, University of Rhode Island, Narragansett, RI, 37 pp.

Battelle 2003. *Alternative site screening report: Rhode Island region long-term dredged material disposal site evaluation project*. Tech. Report.

Blass, M., C. Dong, P. Marchesiello, J.C. McWilliams, and K.D. Stolzenbach 2007. Sediment-transport modeling on Southern California shelves: A ROMS case study. *Continental Shelf Res.* 27: 832-853.

Blumberg, A.F. and G.L. Mellor 1987. Three-dimensional Coastal Ocean Models, chapter A. Description of a three-dimensional coastal ocean circulation model. American Geophysical Union, pps. 1-16.

Booij, N., R.C. Ris, L.H. Holthuijsen 1999. A third-generation wave model for coastal regions. Part I – Model description and validation. *J. Geophys. Res.* 104: 7649-7666.

Cao, Z., G. Pender, and J. Meng 2006. Explicit formulation of the Shields diagram for incipient motion of sediment. *J. Hydr. Engng.* 132(10): 1097-1099.

Chapman, D.C. 1985. Numerical treatment of cross-shelf open boundaries in a barotropic coastal ocean model. *J. Phys. Oceanogr.* 15: 1060—1075.

Chow, F.K. and R.L. Street 2009. Evaluation of turbulence closure models for large-eddy simulation over complex terrain: Flow over Askervein Hill. *J. Appl. Meteor. Clim.* 48: 1050-1065.

Codiga, D.L. and D.A. Aurin 2007. Residual circulation in eastern Long Island Sound: Observed transverse-vertical structure and exchange transport. *Continental Shelf Res.* 27:103-116.

Codiga, D.L. and A.E. Houk 2002. *Current profile time series from the FRONT moored array, technique report*. Technical report, Department of Marine Science, University of Connecticut.

Codiga, D.L. and D.S. Ullman 2010. *Characterizing the physical oceanography of coastal waters off Rhode Island, Part I: Literature review, available observations, and a representative model simulation*. University of Rhode Island. Prepared for the Rhode Island Ocean Special Area Management Plan 2010.

Deines, K.L. 1999. Backscatter estimation using broadband acoustic Doppler current profilers. *Proc. Sixth Working Conf. on Current Measurement.* San Diego, CA, *IEEE*: 249-253.

Ding, L. and R.L. Street 2003. Numerical study of the wake structure behind a three-dimensional hill. *J. Atmos. Sci.* 60: 1678-1690.

Divins, D.L. and D. Metzger 2003. *National Geophysical Data Center coastal relief model*.

Edwards, C.A., T.A. Fake, and P.S. Bogden 2004. Spring-summer frontogenesis at the mouth of Block Island Sound: 1. A numerical investigation into tidal and buoyancy-forced motion. *J. Geophys. Res.* 109: C12021.

Eidsvik, K.J. 2005. A system for wind power estimation in mountainous terrain. Prediction of Askervein Hill data. *Wind Energy* 8: 237-249.

Emery, W.J. and R.E. Thompson 2001. *Data Analysis Methods in Oceanography.* Elsevier.

Fedorovich, E., E.T.M. Nieuwstadth, and R. Kaiser 2001. Numerical and laboratory study of a horizontally evolving convective boundary layer. Part I: Transition regimes and development of the mixed layer. *J. Atmos. Sci.* 58: 70-86.

Flather, R.A. 1976. A tidal model of the northwest European continental shelf. *Memoire de la Société Royale des Sciences de Liège 6ème série.* 10: 141-164.

Gostiaux, L. and H. van Haren 2010. Extracting meaningful information from uncalibrated backscattered echo intensity data. *J. Atmos. Oceanic Tech.* 27:943-949.

Hasselmann, K. and D. Olbers 1973. Measurements of wind-wave growth and swell decay during the Joint North Sea Wave Project (JONSWAP). *Erganzung zur Deut. Hydrog. Z. Reihe A* (8) 12: 1-95.

Hastings, M.E., L.J. Poppe, and J.C. Hathaway 2000. *USGS east-coast sediment analysis: procedures, database, and georeferenced displays*. Chapter 2: surficial sediment database. USGS open-file report 00-358.

He, R. and J.L. Wilkin 2006. Barotropic tides on the southeast New England shelf: A view from a hybrid data assimilative modeling approach. *J. Geophys. Res.* 111:C08002.

Jimenez, J.A. and O.S. Madsen 2003. A simple formula to estimate settling velocity of natural sediments. *J. Waterway, Port, Coastal and Ocean Engng.* 129(2): 70-78.

Lane, T.P., R.D. Sharman, R.G. Frehlich and J.M. Brown 2006. Numerical simulations of the wake of Kauai. *J. Appl. Meteor. Clim.* 45: 1313-1331.

Le Provost, C., F. Lyard, J.M. Molines, M.L. Genco, and F. Rabilloud 1998. A hydrodynamic ocean tide model improved by assimilating a satellite altimeter-derived data set. *J. Geophys. Res.* 103(C3): 5513-5529.

Lynch, D.R., C.E. Naimie, and C.G. Hannah 1998. Hindcasting the Georges Bank circulation, Part I: detiding. *Continental Shelf Res.* 18: 607-639.

Malkus, J.S., and A. E. Bunker 1952. Observational studies of the air flow over Nantucket island during the summer of 1950. *Papers in Physical Oceanography and Meteorology*, XII, No. 2, Massachusetts Institute of Technology and Woods Hole Oceanographic Institution, 50 pp.

Marshall, J.C., A. Adcroft, C. Hill, L. Perelman, and C. Heisey 1997. A finite-volume, incompressible Navier Stokes model for studies of the ocean on parallel computers. *J. Geophys. Res.* 102: 5753-5766.

Matthews, S., J. M. Hacker, J. Colle, J. Hare, C. N. Long, and R. M. Reynolds 2007. Modification of the atmospheric boundary layer by a small island: Observations from Nauru. *Mon. Wea. Rev.* 135: 891–905, doi:10.1175/MWR3319.1.

Mau, J.-C., D.-P. Wang, D.S. Ullman, and D.L. Codiga 2006. Comparisons of observed (HF radar, ADCP) and model barotropic tidal currents in the New York Bight and Block Island Sound. *Estuarine Coastal and Shelf Sci.* 72: 129-137.

Mellor, G.L. and T. Yamada 1982. Development of a turbulence closure model for geophysical fluid problems. *Rev. Geophys. Space Phys.* 20: 851-875.

Meyer-Peter, E. and R. Mueller 1948. Formulas for bedload transport. In: *Report on the second meeting of the International Association Hydraulic Structure Research.* Stockholm, Sweden: 39—64.

Moeng, C.-H., J. Dudhia, J. Klemp, and P. Sullivan 2007. Examining two-way grid nesting for large eddy simulation of the PBL using the WRF model. *Mon. Weather Rev.* 135: 2295-2311.

Moody, J.A., B. Butman, R.C. Beardsley, W.S. Brown, P. Daifuku, J.D. Irish, D.A. Mayer, H.O. Mofield, B. Petrie, S. Ramp, P. Smith, and W.R. Wright 1984. *Atlas of tidal elevation and current observations on the Northeast*. American Continental Shelf and Slope. United States Geological Survey.

Mukai, A.Y., J.J. Westerink, R.A. Luettich, Jr., and D. Mark 2002. *Eastcoast 2001, a tidal constituent database for western North Atlantic, Gulf of Mexico, and Caribbean Sea*. Tech. Report. ERDC/CHL TR-02-24. Coastal and Hydraulics Laboratory, US Army Corps of Engineers.

Oey, L.-Y., H.T. Manning, and K.W. Young 1995. *Quantitative Skill 1 Assessment for Coastal Ocean Models, chapter A*. A plume and wind driven circulation model of the New York Bight. American Geophysics Union, pps. 329-347.

Pawlowicz, R., B. Beardsley, and S. Lentz 2002. Classical tidal harmonic analysis including error estimates in MATLAB using T_TIDE. *Computers and Geosci.* 28: 929-937.

Prospathopoulos, J., and S.G. Voutsinas 2006. Implementation issues in 3D wind flow predictions over complex terrain. *J. Sol. Energy Eng.* 128: 539-553.

RAMS 2010. Regional Atmospheric Modeling System Technical Manual, Weather Flow.

Reid, J.M., J.A. Reid, C.J. Jenkins, M.E. Hastings, S.J. Williams, and L.J. Poppe 2005. *usSEABED: Atlantic coast offshore surficial sediment data release*. US Geological Survey Data Series 118, version 1.0.

Shchepetkin, A.F. and J.C. McWilliams 2005. Regional Ocean Model System: a split-explicit ocean model with a free-surface and topography-following vertical coordinate. *Ocean Modelling* 9: 347-404.

Shapiro, R. 1975. Linear filtering. *Mathematics of Comput.* 29: 1094-1097.

Shaw, W.J., J.K. Lundquist and S.J. Schreck 2009. Research needs for wind resource characterization. *Bull. Amer. Meteor. Soc.* 90: 535-538, doi:10.1175/2008BAMS2729.1.

Shearman, R.K. and S. J. Lentz 2004. Observatinos of tidal variability on the New England Shelf. *J. Geophys. Res.* 109: C06010.

Silva Lopes, A., J.M.L.M. Palma, and F.A. Castro 2007. Simulation of the Askervein flow. Part 2: Large-eddy simulations. *Bound.-Layer Meteor*. 125: 85-108.

Smith, R.B., and V. Grubišic 1993. Aerial observations of Hawaii's wake. *J. Atmos. Sci.* 50: 3728-3750.

Smith, R.B., A. C. Gleason, P.A. Gluhosky, and V. Grubišic 1997. The wake of St. Vincent. *J. Atmos. Sci.* 54: 606–623.

Song, Y. and D.B. Haidvogel 1994. A semi-implicit ocean circulation model using a generalized topography-following coordinate system. *J. Comp. Phys.* 115(1): 228-244.

Soulsby, R.L. and J.S. Damgaard 2005. Bedload sediment transport in coastal waters. *Coastal Engng.* 52: 673-689.

Spaulding, M.L., M. Bell, J. Titlow, L. Decker , A.R. Grilli, R. Sharma and D. Mendelsohn 2010a. Meteorological Model based Wind Resource Assessment in the Vicinity of Block Island. *SAMP Report.* Ocean Engineering, University of Rhode Island, Narragansett, RI, 34 pp.

Spaulding, M.L., M. Bell, Jay Titlow, R. Sharma, A.R. Grilli, A. Crosby and L. Decker and Daniel Mendelsohn 2010b. Wind Resource Assessment in the Vicinity of a Small, Low Relief Coastal Island. *SAMP Report.* Ocean Engineering, University of Rhode Island, Narragansett, RI, 45 pp.

Thomson, R.E., J.F.R. Gower, and N.W. Bowker 1977. Vortex streets in the wake of the Aleutian Islands. *Mon. Wea. Rev*. 105: 873-884.

Ullman, D.S. and D.L. Codiga 2004. Seasonal variation of a coastal jet in the Long Island Sound outflow region based on HF radar and Doppler current observations. *J. Geophys. Res.* 109: C07S06.

Walmsley, J.L. and P.A. Taylor 1996. Boundary-layer flow over topography: Impacts of the Askervein study. *Bound.-Layer Meteor*. 78: 291-320.

Warner, J.C., C.R. Sherwood, R.P. Signell, C.K. Harris, and H.G. Arango 2008a. Development of a three-dimensional, regional, coupled wave, current, and sediment-transport model. *Computers and Geosc.* 34:1284-1306.

Warner, J.C., B. Butman, and P.S. Dalyander 2008b. Storm-driven sediment transport in Massachusetts Bay. *Continental Shelf Res.* 28: 257-282.

Wiberg, P.L. and C.K. Harris 1994. Ripple geometry in wave-dominated environments. *J. Geophys. Res.* 99(C1): 775-789.

WRF 2008. *A description of the Advanced Research WRF Version 3.* NCAR Technical Note TN-475+STR, 125 pp.

Appendix A:

Hydrodynamics of Block Island Sound (HYDROMAP tidal simulations) for the Rhode Island Ocean Special Area Management Plan

by

Deborah Crowley and Daniel Mendelsohn

Applied Science Asociates, Inc.

55 Village Square Drive

South Kingstown, RI 02879

June 16, 2010

Executive Summary

It has been proposed that a wind turbine farm be developed off the southeastern coast of Block Island, south of the Rhode Island mainland. The development of an offshore wind farm will necessarily require a great deal of underwater construction including drilling and setting the piles for the turbine foundations, burying electrical transmission cables and other infrastructure construction tasks. During this period additional water column suspended sediments may impact the construction areas and it is therefore of interest to understand what the current speeds and circulation patterns are in the development area. To that end, Applied Science Associates, Inc. (ASA) has performed a hydrodynamic modeling study to estimate the currents and circulation in the renewable energy (RE) development area with a focus on bottom stress and currents. The results of the study will be used by URI scientists to determine the potential for sediment re-suspension and transport of suspended sediment that might results from the construction and operation of the small wind farm.

ASA used the HYDROMAP model system, which calculates velocity vectors on a stepwise continuous variable rectangular grid system. A benefit of the model is that it allows coarse grid resolution in the areas offshore the coast of Rhode Island and finer resolution in the Block Island Sound area and renewable energy zone area of interest. The model was driven by tidal harmonic data along the open boundaries and wind stress at the surface. The model predictions were compared to observations collected as part of the OSAMP, including four ADCP current meter locations and NOAA tidal elevation data at Montauk and Newport. The comparisons showed that the model not only adequately predicted the tidal forcing response in the study area, but also the longer period episodic wind driven events that are characterized by passing weather systems. The model appeared to be able to reproduce both the horizontal spatial variability in the system as well as the vertical profile of the currents, as represented by the ADCP observations at the surface, mid and bottom of the water column.

Both observations and the model predictions confirm that the dominating tidal constituent is the M2 constituent which represents between 50-60% of the total tidal amplitude at all stations. The amplitude predictions for all constituents tend to be higher than the observed but are generally within 20% of the observed with the exception of Montauk. The Montauk station is located in the shallows of an embayment that the mode grid does not resolve in fine detail, this may contribute to the over prediction of tidal amplitude.

Review of the current analysis indicates that the differences between the model predicted and observed M2 constituent major axes are generally less than 0.02 m/s with a maximum deviation of 0.05 m/s in the MDF bottom current ellipse. The difference in the remaining constituents is variable, remaining less than 0.01 m/s for the majority. The M2 phase comparison between the model predictions and observations is similarly close, with the difference angle remaining less than about 10 degrees with an exception in the bottom currents at both the POS and POF stations. In general, the model predicted tidal current ellipses, driven predominantly by the M2 tidal component, show a close agreement with the observations indicating that the model captures the magnitude and the circulation patterns in the study area.

The bottom currents were further reviewed and an understanding of the bottom speed developed. The renewable energy zone follows the edge of the 3 mile state waters limit along the southern portion of the line, from the straights between Long Island and Block Island to the west, to the shipping channel exclusion zone on the east. The zone is approximately 2 km wide, and has a bulge on the east side representing the shipping channel exclusion zone. Bathymetry in the RE zone is quite variable ranging from less than 10m, in the western portion to greater than 35m to the east. This bathymetric range and the straights to the west produce a significant variability in the bottom speeds as well, ranging from a high in the shallow western portions of 0.25 m/s down to a high in the eastern portions of 0.15 m/s.

Tabel of Contents

List of Figures

List of Tables

1 Introduction

Deepwater Wind Associates LLC has proposed to build a wind turbine farm off the southeastern coast of Block Island, south of the Rhode Island mainland. The pilot project will consist of 8-10 wind turbine generators (WTG), located in a line inside of the 3-nautical mile state waters limit and roughly following the 3-nautical mile boundary. As a part of the state of Rhode Island's evaluation of the project, the RI Coastal Resources Management Council (CRMC) is developing an Ocean Special Area Management Plan (OSAMP) for the area to evaluate and weight competing uses for the area. The result will be a final renewable energy area set aside for offshore wind development projects.

The University of Rhode Island has contracted with Applied Science Associates, Inc. to perform an analysis to estimate the currents and circulation in the renewable energy development area with a focus on bottom stress and currents. The results will be evaluated by URI scientists to determine the potential for sediment re-suspension and transport of suspended sediment that might result from the construction and operation of the small wind farm.

Currents were simulated by the ASA model, HYDROMAP, which calculates velocity vectors on a stepwise continuous variable rectangular grid system. The model allows coarse grid resolution in the areas offshore the coast of Rhode Island and finer resolution in the Block Island Sound area. The model predicts water surface elevation and currents that can be used directly in other ASA transport and distribution models for sediment and pollutant transport modeling.

This report documents the model application and predictions of the HYDROMAP model application to Block Island Sound. Section 2 describes the study area and project. Section 3 presents the HYDROMAP model used to simulate currents and its application and results. Section 4 provides a discussion and conclusions from the study and Section 6 lists references.

2 Description of the Study Area

The proposed wind energy project is to be located just less than 3 miles from the southeast coast of Block Island in an area where Block Island Sound Rhode Island Sound and the Atlantic Ocean meet (Figure 2-1). Also shown in the figure is the OSMAP proposed study area which encompasses both RI state and federal waters and the 3 nautical mile limit of the RI state waters. The SAMP area lies south of the southern coast of Rhode Island and lies west of Martha's Vineyard and east of Long Island. It is approximately 2300 km^2 (880 mi^2) in area with depths

ranging from less than 20 m (65 ft) below Mean Sea Level (MSL) to greater than 80 m (260 ft) MSL.

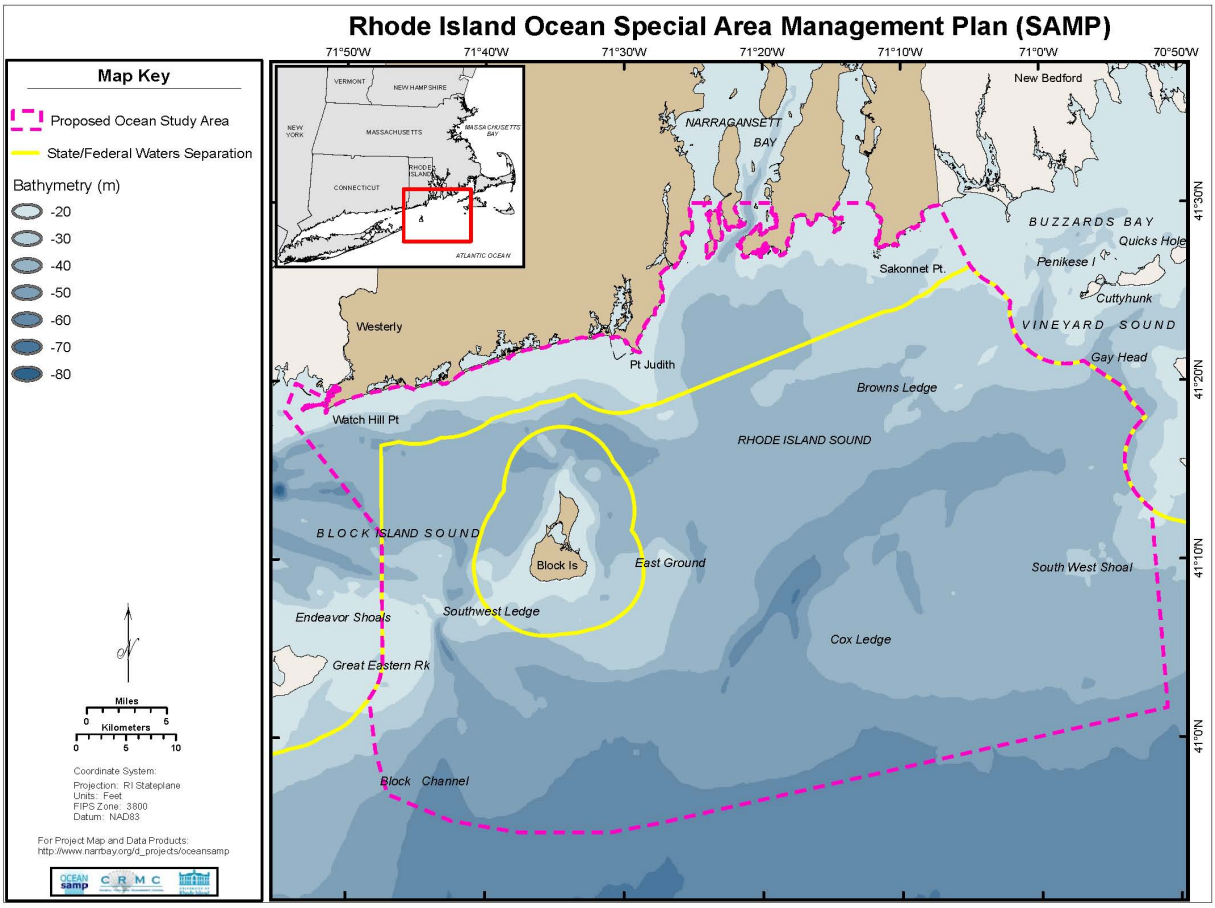

Figure 2-1 Block Island Sound study area showing the OSAMP designated area and the modeled domain between Buzzards Bay and Long Island Sound.

The proposed Renewable Energy (RE) Zone lies along the southern arc of the limit of state waters around Block Island, in a 2 kilometer wide band (Figure 2-2). The eastern edge of the RE zone is cut out to allow for the shipping lane exclusion area. The proposed pilot project wind park will consist of 8-10 wind turbine generators (WTG), in a line curving along the eastern part of the RE zone. Each WTG is to be mounted on a jacket structure with 4 piles, each of which will be driven into the seabed.

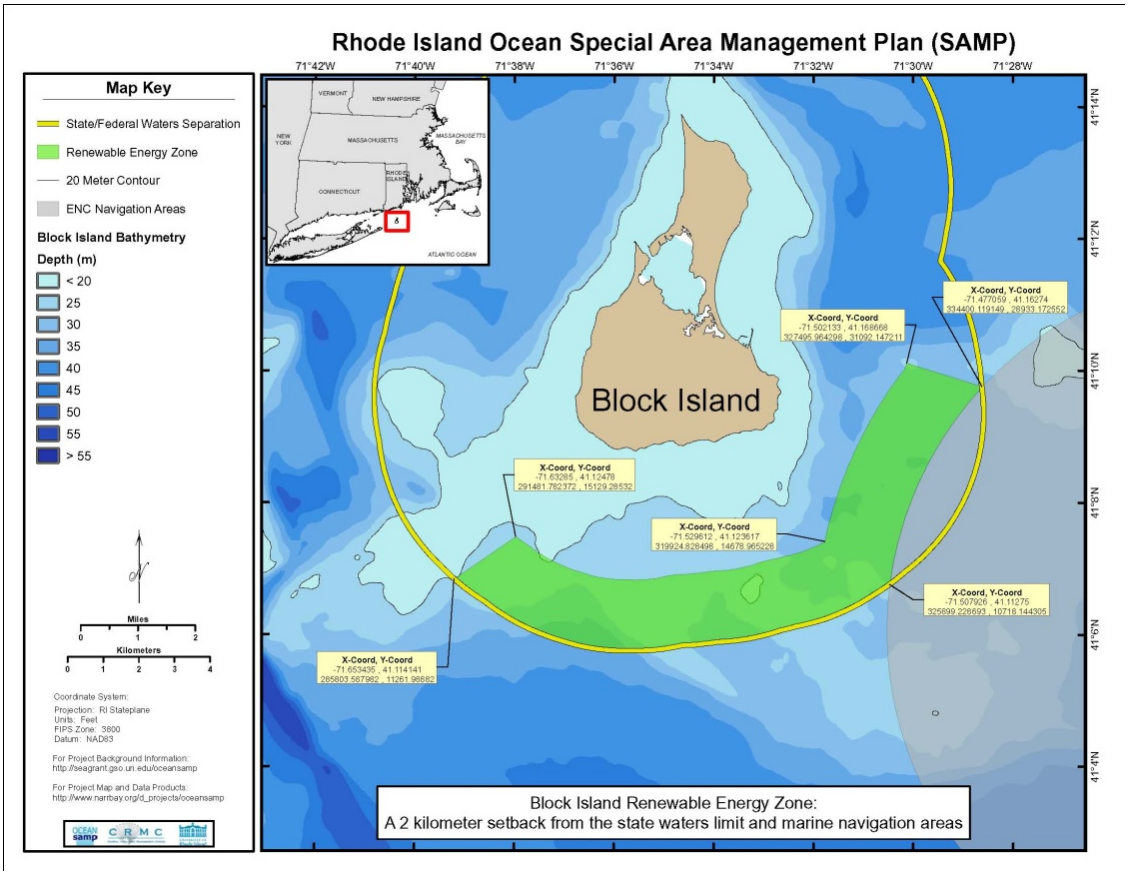

Figure 2-2 Proposed renewable energy zone in Rhode Island State waters, south of Block Island

2.1 Hydrographic Observations in the Area

As a part of the OSAMP a large field program was developed and implemented through which four offshore stations were deployed; the locations of these stations are illustrated in Figure 2 3. The offshore stations include two buoys that are fitted with both a surface current meter and a downward looking Acoustic Doppler Current Profiler (ADCP), both measuring current magnitude and direction, as well as meteorological observation equipment recording wind speed and direction. One of these buoy stations (Station MDS) is located south of Block Island on the 3 nautical mile state boundary limit and the other is located east of Block Island in federal waters (Station MDF). The remaining two offshore stations have deployed bottom mounted ADCPs measuring water pressure (surface elevation) and current magnitude and direction. These stations are located in close proximity to the buoy stations; one farther south of MDS (Station POS) and the other inshore of MDF (Station POF); these locations are also

illustrated in Figure 2-3. In addition to OSAMP deployed instrumentation there are a number of fixed stations in the study area maintained by NOAA; of these stations two were queried for surface elevation data: Montauk, NY (Station 8510560) and Newport, RI (Station 8452660), these stations are also illustrated in Figure 2-3.

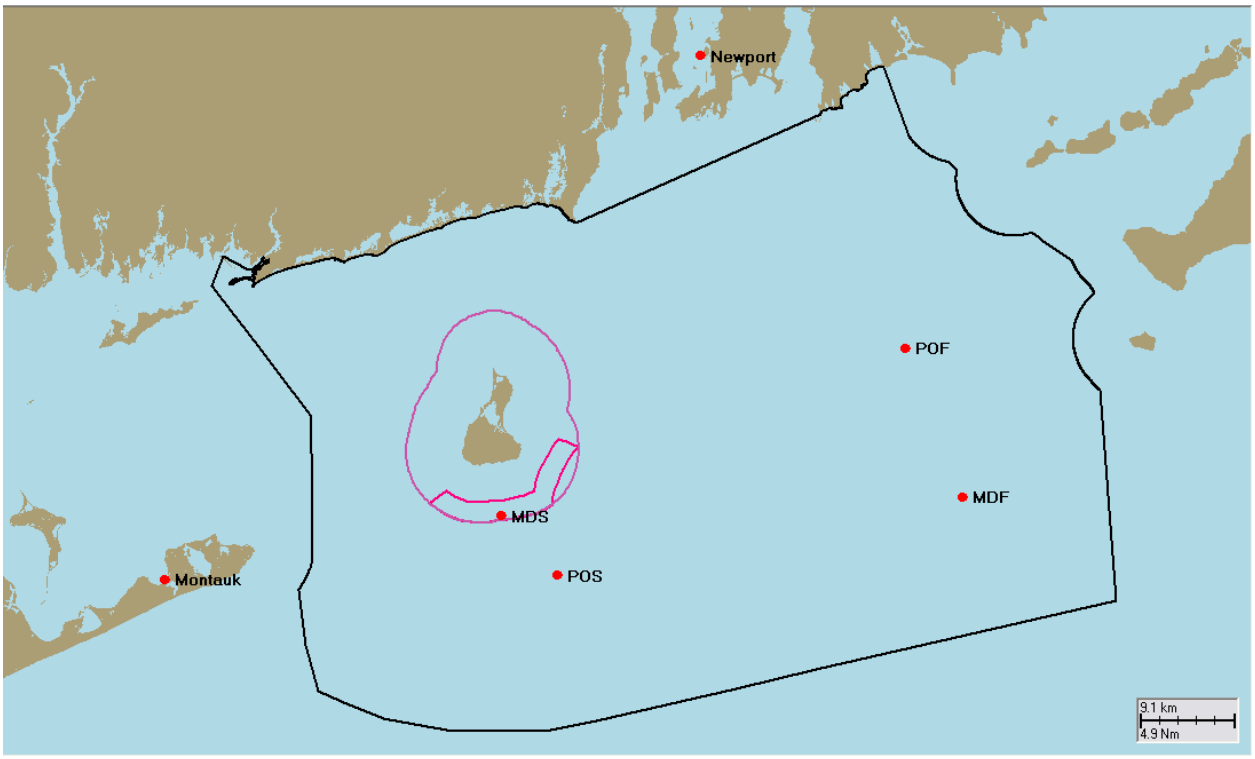

Figure 2-3 Offshore monitoring station locations for the OSMAP field program. Figure also shows the NOAA tide station locations at Newport, RI and Montauk, NY on Long Island.

2.1.1 Tidal Elevation Observations

Water surface elevation data was available from stations POS and POF as well as from NOAA observations stations at Montauk, NY (Station 8510560) and Newport, RI (Station 8452660); all locations are illustrated in Figure 2-3. Observations at stations POS and POF were recorded at two hour intervals and observations at Montauk and Newport were recorded at six minute intervals.

2.1.2 Current Observations

The previously mentioned MDS, MDF, POS and POF stations recorded ocean water currents. The MDS and MDF stations are identical in set up and instrumentation however differ from the

setup and instrumentation at POS and POF which are set up identical to each other; all station locations are illustrated in Figure 2-3.

Stations MDS and MDF included both top mounted ADCPs located 5m below the water surface and a surface current meter located 3m below the water surface. The top mounted ADCPs record the current vector components (U and V) at 1m depth intervals from 5m below the water surface to the bottom; these observations are recorded at an hourly interval. The surface current meter records the speed and direction at a depth of 3m below the water surface; these observations are recorded at an hourly interval. Observations at these stations were available from October 2009 through present (June 2010).

Stations POS and POF include bottom mounted ADCPs which record current speed and direction at 0.75m intervals from the bottom (1st bin centered at approximately 1.8m above the sea floor) to the surface; these observations are recorded on a two hour interval and observations were available from September 2009 through January 2010.

2.1.3 Wind Observations

Both MDS and MDF stations record wind speed and direction at a height of 5m above the water surface. These observations are recorded hourly and were available from October 2000 through present (June 2010).

3 HYDROMAP Hydrodynamic Model

3.1 Model Description

HYDROMAP is a globally re-locatable hydrodynamic model (Isaji, et al., 2001) capable of simulating complex circulation patterns due to tidal forcing, wind stress and fresh water flows quickly and efficiently anywhere on the globe. HYDROMAP employs a novel step-wise-continuous-variable-rectangular (SCVR) gridding strategy with up to six levels of resolution. The term step-wise continuous implies that the boundaries between successively smaller and larger grids are managed in a consistent integer step. The advantage of this approach is that large areas of widely differing spatial scales can be addressed within one consistent model application. Grids constructed by the SCVR are still "structured," so that arbitrary locations can be easily located to corresponding computational cells. This mapping facility is particularly advantageous

when outputs of the hydrodynamics model propagate to subsequent application programs (e.g. Lagrangian particle transport model [SSFATE, OILMAP]) that use another grid or grid structure.

The hydrodynamic model solves the time dependent, three-dimensional conservation equations for water mass, density, and momentum in spherical coordinates with the Boussinesq and hydrostatic assumptions applied. Model output consists of surface elevation and the three dimensional field of horizontal current velocities. The numerical solution methodology follows that of Davies (1977) and Owen (1980). The interested reader is directed to Isaji, et al. (2001), and Isaji and Spaulding (1984) for a detailed description of the model.

3.2 Model Application to the Ocean SAMP Area

3.2.1 Model Grid

The Ocean SAMP area is located in a complex topographic and bathymetric area which results in a complex current velocity structure. In order to account for this complexity the hydrodynamic model domain was extended to deep waters (~200 m [660 ft]) in the south and east directions off of Cape Cod and Nantucket, to the terminus of Long Island Sound and the New York Bight in the west direction and approximately 45 miles south, offshore of the OSAMP study area and the coasts of New York, Rhode Island and Massachusetts.

Figure 3-1 shows the computational model grid cells for the entire domain, consisting of 27,569 active water cells. At the open boundary and in the outer regions, a maximum cell size of ~2.0 km (~1.25 mi) was assigned. Cell resolution was gradually increased toward OSAMP area (Figure 3 2) with the finest resolution of ~125 m (~410 ft) applied in the Renewable Energy zone south of Block Island (Figure 3-3). The model set up allows for three dimensional model simulations, which was utilized for this study. The vertical grid is represented by Legendre polynomials, in this instance six polynomials were used to represent the vertical variability in the currents.

The bathymetry data used in the model grid was assembled from various sources: NOAA NGDC Coastal Relief Model (2010), and ETOPO2 (NGDC 2001). Figure 3-4 through Figure 3-6 show the bathymetry used in the model for the three grid views shown in Figure 3-1 through Figure 3-3).

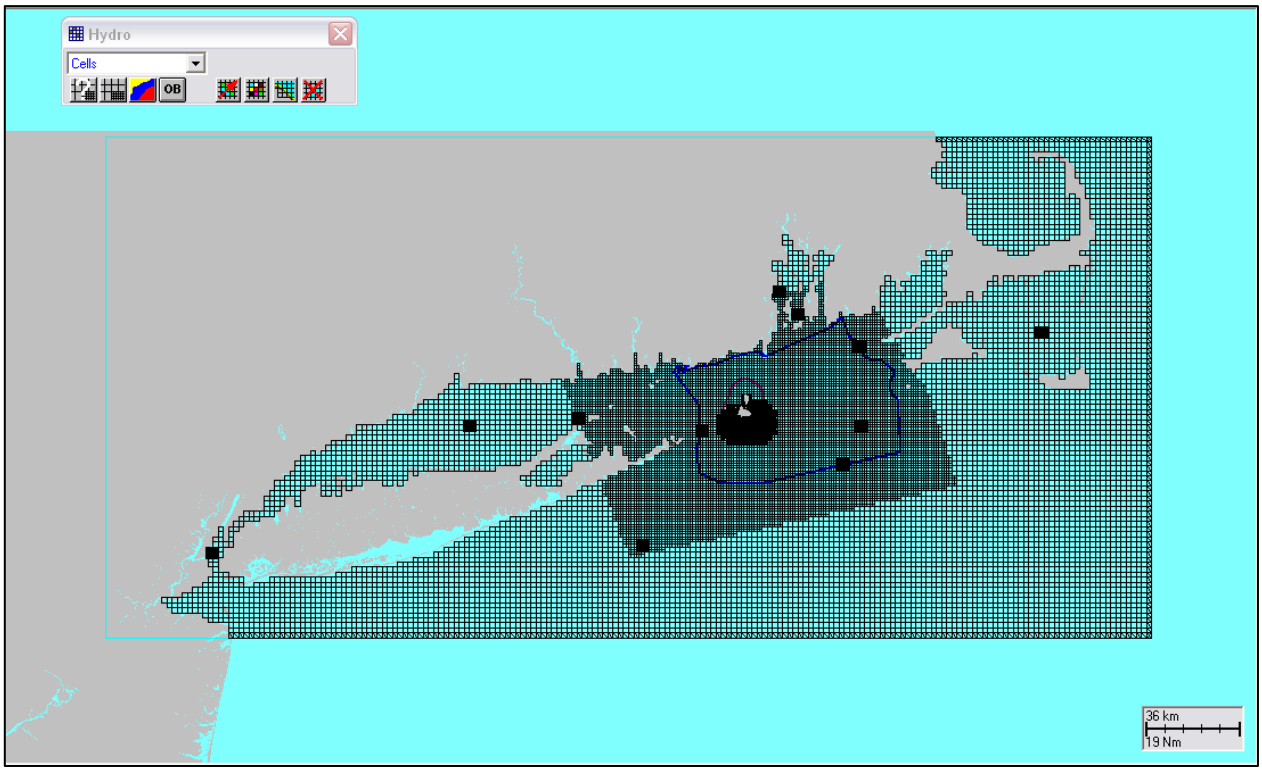

Figure 3-1 Hydrodynamic model grid cells for the entire HYDROMAP area.

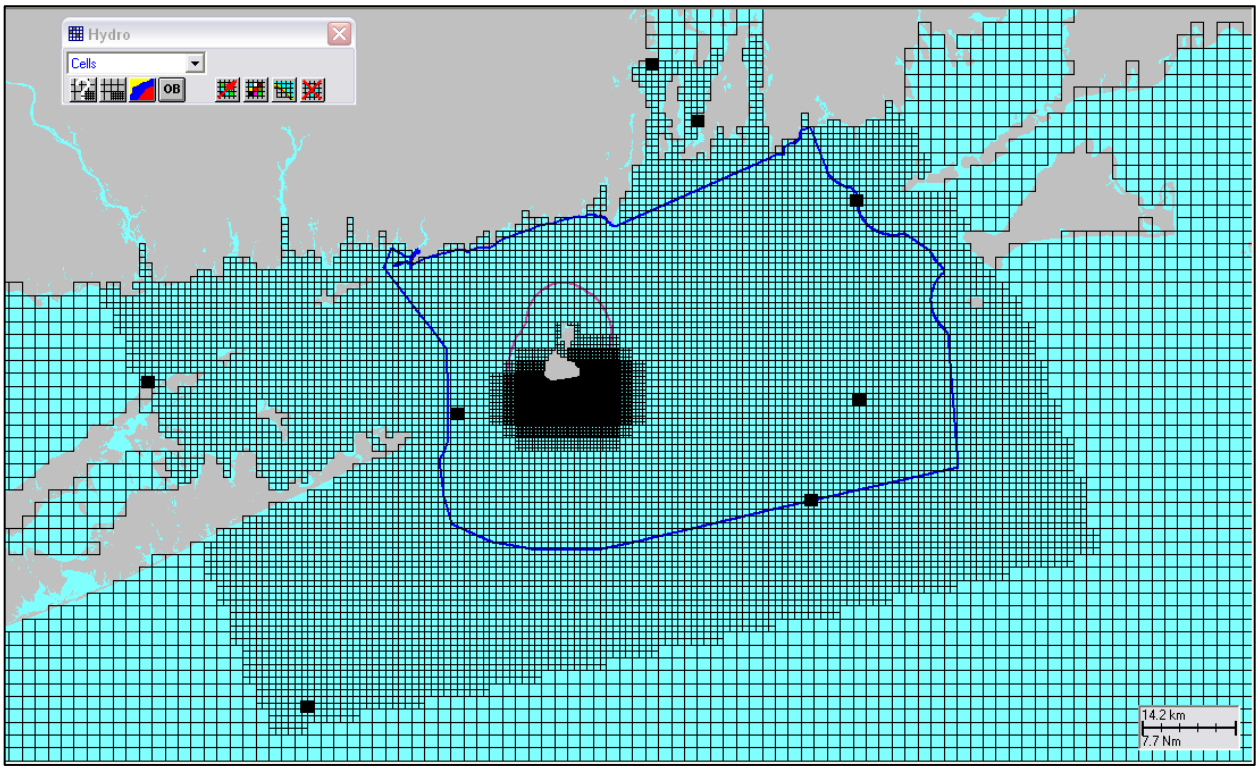

Figure 3-2 Hydrodynamic model grid cells for the OSAMP area.

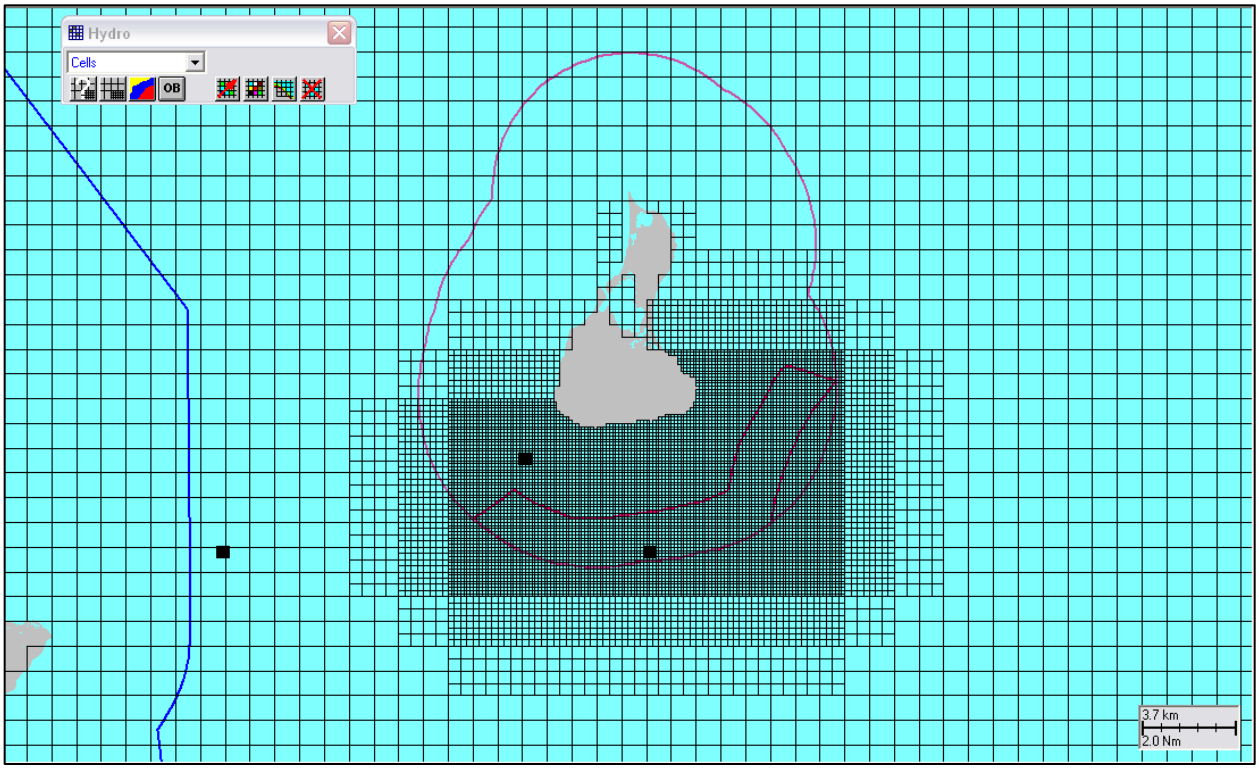

Figure 3-3 Hydrodynamic model grid cells for the Block Island Sound area.

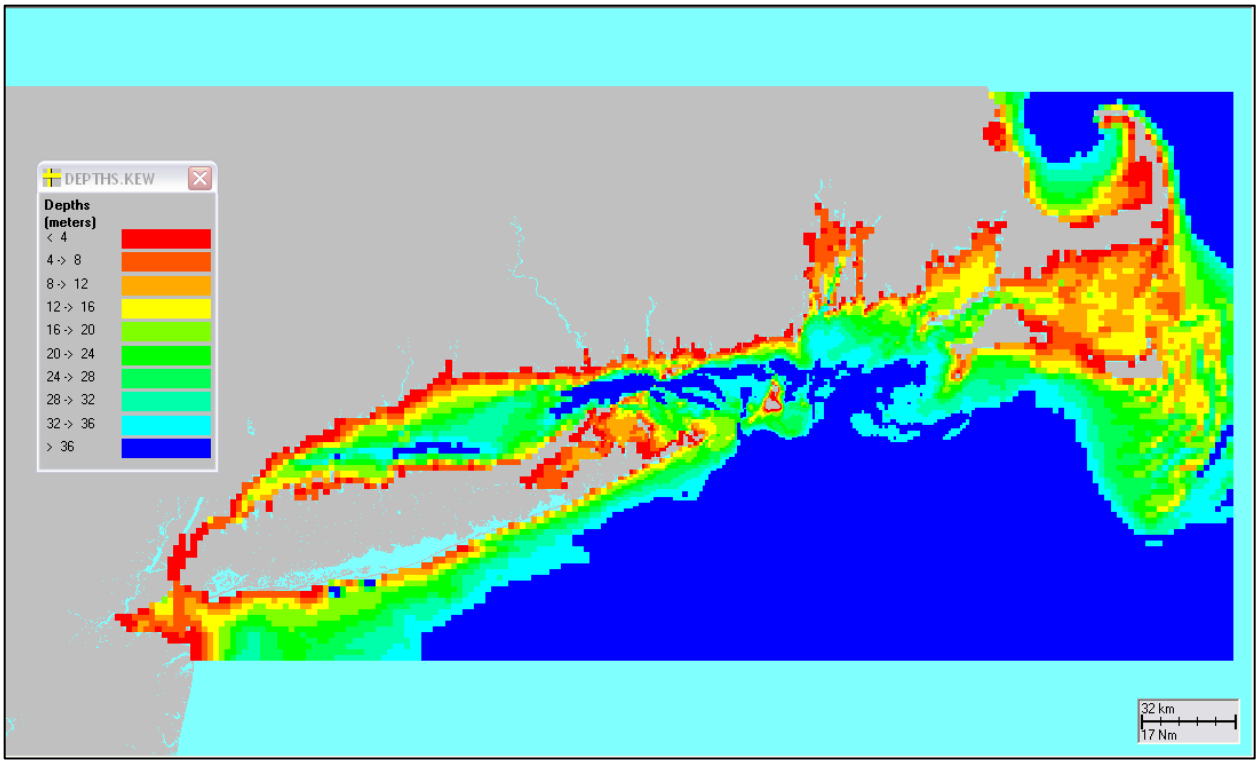

Figure 3-4 Hydrodynamic model grid depths for the entire HYDROMAP grid area.

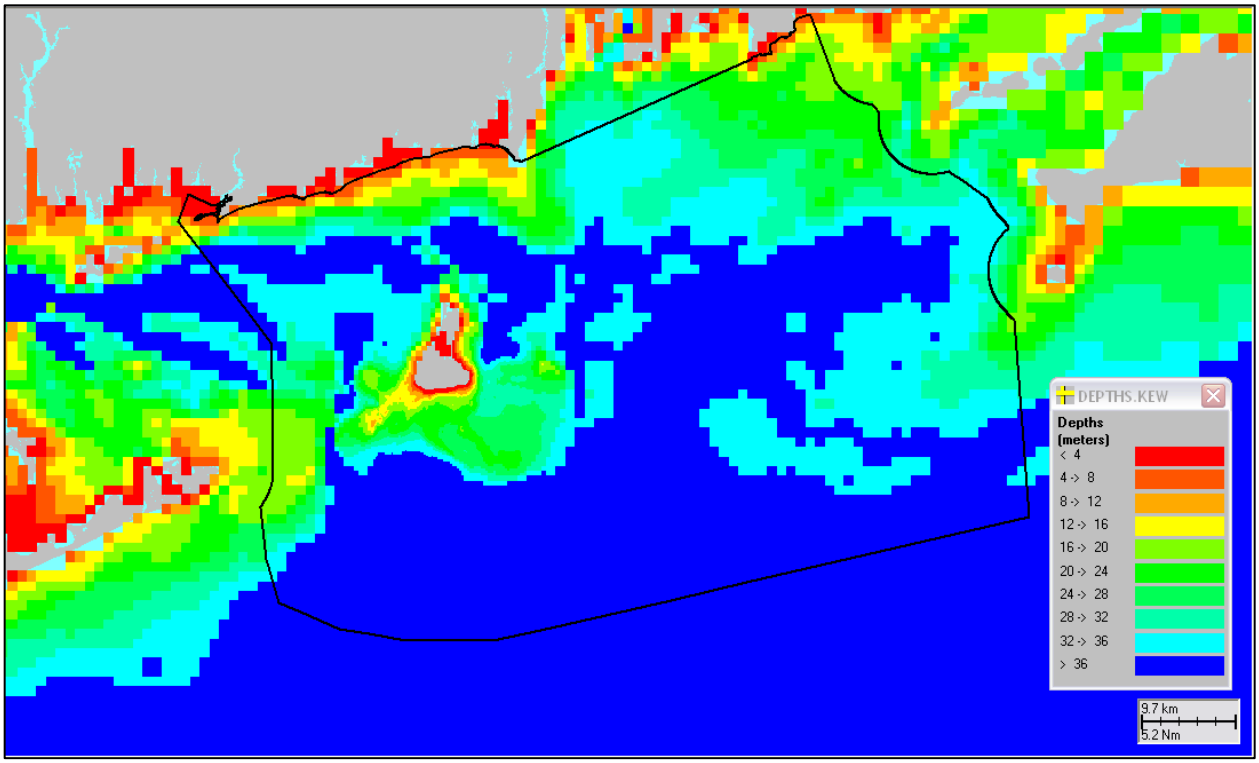

Figure 3-5 Hydrodynamic model grid depths for the OSAMP area.

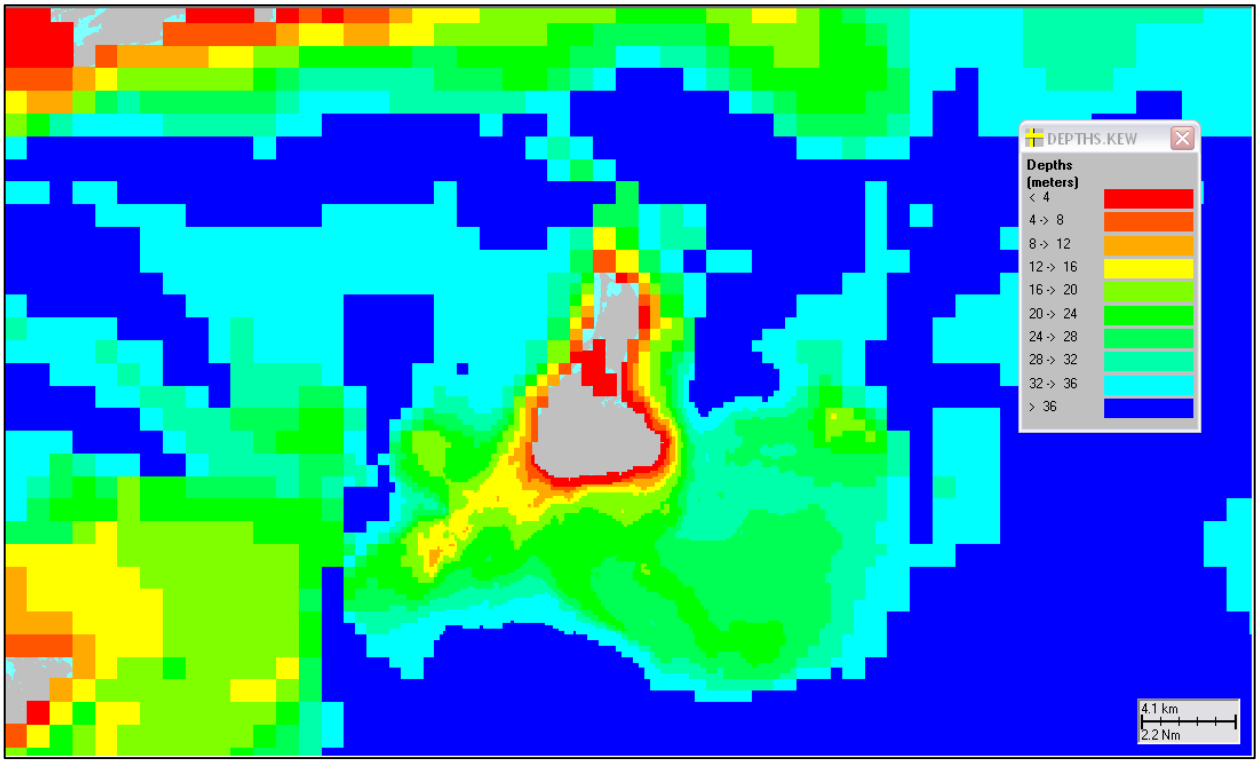

Figure 3-6 Hydrodynamic model grid depths for the Block Island Sound area.

3.2.2 Model Forcing

3.2.2.1 Tides

The water circulation in Block Island Sound is mostly tidally driven (Gordon and Spaulding, 1979). Harmonic constituent data extracted from the TPXO global tidal model was used at the model open boundaries. Each boundary cell was assigned a unique set of the harmonic constituent amplitudes and phases. An example of the M2 constituent amplitude is presented in Figure 3-7. In total, the open boundary was specified for the predominant 5 tidal constituents in the area: three semi-diurnals (M2, N2, and S2) and two diurnals (K1 and O1). HYDROMAP (Isaji et al 2001), employs a strategy that uses the harmonic construction of astronomic tidal currents where each harmonic (constituent) is simulated individually and then the real time tide is assembled using the harmonic summation of these simulated constituents.

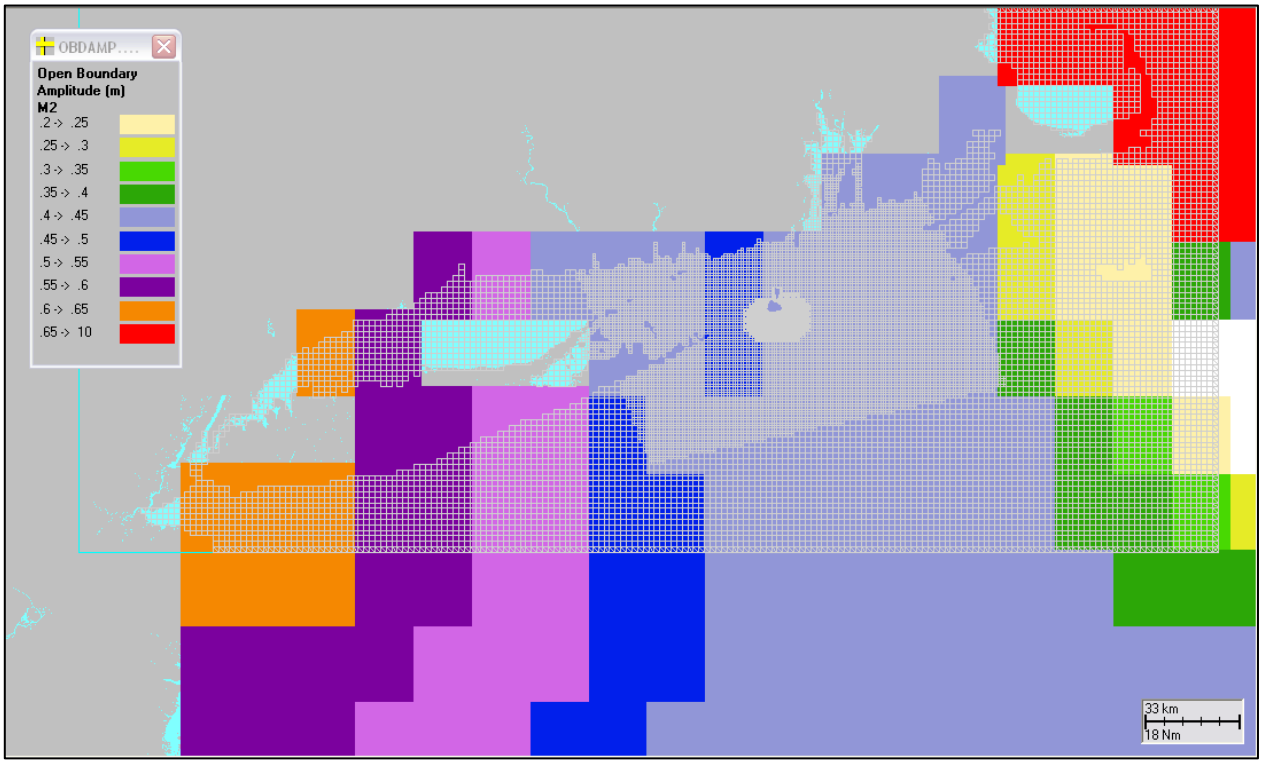

Figure 3-7 Example hydrodynamic model M2 harmonic constituent amplitudes covering the HYDROMAP grid domain.

Once calculated, this harmonic set can be used for any future time or for any simulation length. The bottom currents and shear stress can also be calculated for any future time or past time for use in hindcast assessments where the wind and wave environment and associated sediment concentrations might be known. In addition, application models that use this

hydrodynamic output, such as SSFATE for suspended sediments, can be run for any specific date or period without extra effort.

3.2.2.2 Wind Forcing

After the tides the wind on the water surface is the most important forcing in the study domain. Wind observations recorded at the MDS station were used as input for the wind forcing in the model. A time series plot of the wind vectors is presented in Figure 3-8 for the study time period.

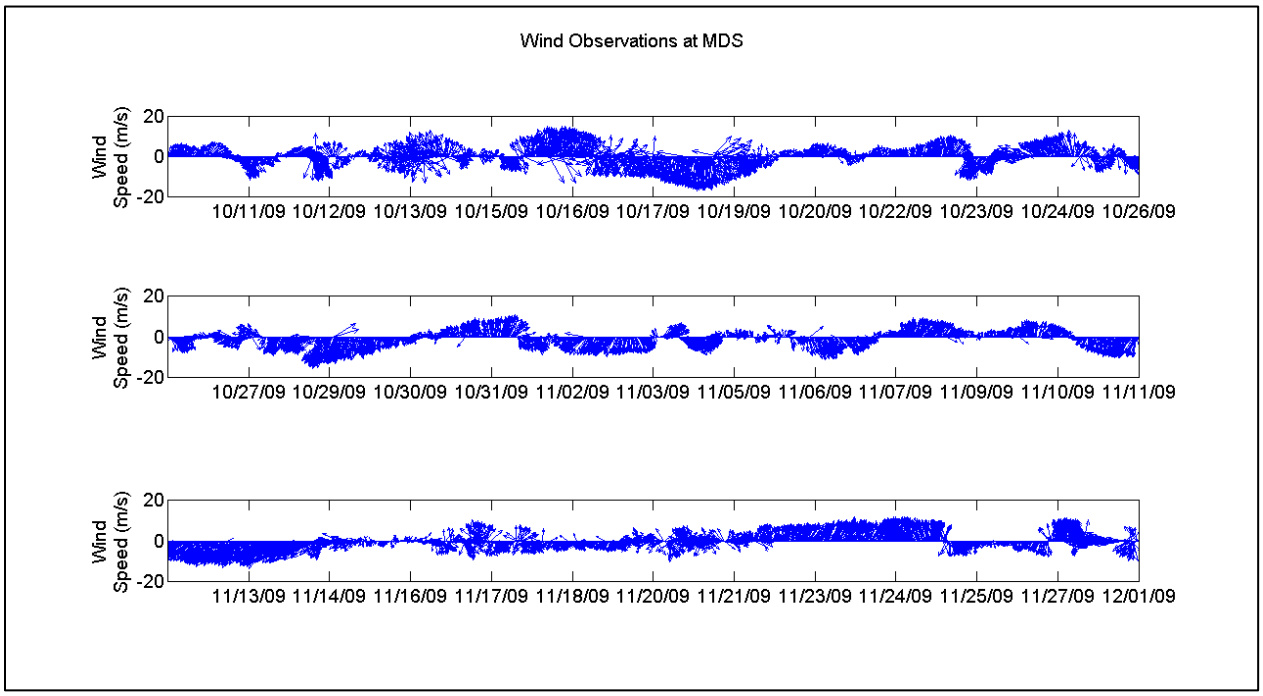

Figure 3-8 Wind time series stick plot of observations at station MDS, located south of Block Island.

3.3 HYDROMAP Model Results

The hydrodynamic model was set up and run for a time period within the field program, running from October 15, 2009 through December 3, 2009. Model predictions of surface elevation and currents were compared to observations during this time period and the following sections present both qualitative and quantitative comparisons.

3.3.1 Tides

The model predicted surface elevations were compared to observation to evaluate the model performance. Both time series comparisons and comparisons of the results of harmonic

decomposition were performed. Figure 3-9 illustrates the time series of observed and predicted surface elevations at Newport, Montauk, POS and POF. This figure shows that the model does well predicting the tidal amplitude and phase over time; the tidal amplitude at all stations is less than 1m. There are periods of time in which the observed surface elevation mean deviates from zero that the model does not capture; these events are likely due to meteorological or large scale ocean currents that are not included in the model forcing.

Table 3-1 and Table 3-3 compare the observed with the simulated harmonic constituent amplitudes and phase respectively. Both observations and the model confirm that the dominating tidal constituent is the M2 constituent which represents between 50-60% of the total tidal amplitude at all stations for both model and observed. The amplitude predictions for all constituents tend to be higher than the observed. The model predictions for the M2 tide are within 20% of the observed with the exception of Montauk. The Montauk station is located in the shallows of an embayment that the mode grid does not resolve in fine detail, this may contribute to the over prediction of tidal amplitude. The predicted amplitudes of the remaining constituents differ in higher percentages, however their contribution to the tidal signal is much smaller than the M2 and therefore even small amplitude differences result in large percentages. The phase predictions for the M2 are also good, with all but Montauk predictions within 16 degrees (33 minutes) of those observed. The remaining constituent phase predictions are all within 37 degrees of those observed.

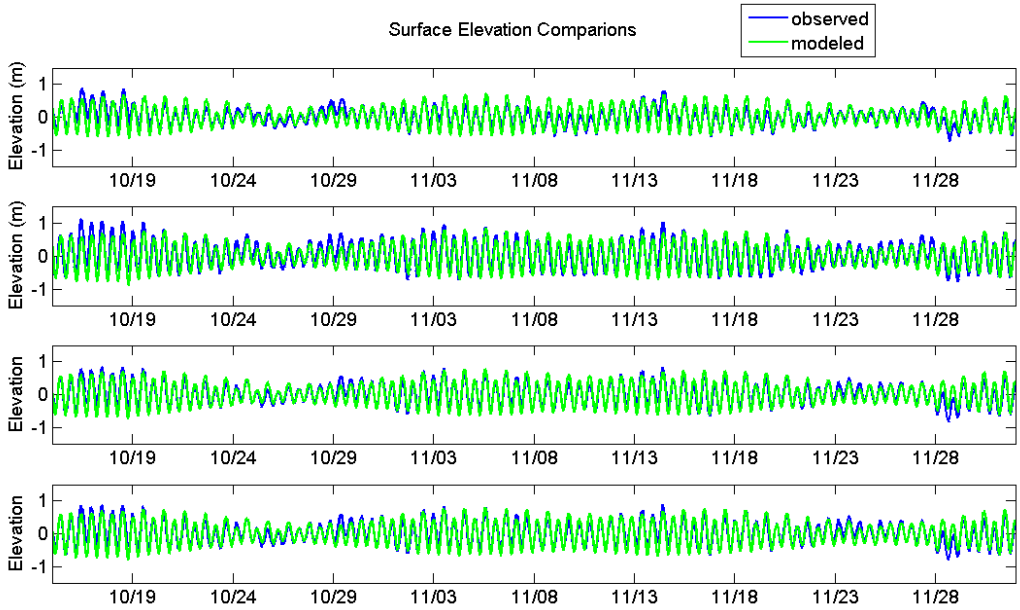

Figure 3-9 Time series comparison of tidal elevations at 4 stations in the study area including stations Montauk, Newport, POS and POF.

Table 3-1 Tidal amplitude comparison between model predictions and observations for the most significant harmonic constants at Newport, Montauk, POS and POF.

Station	Const	Amplitude (m) modeled	Amplitude (m) observed	Difference (Model - Obs)
Newport	M2	0.514	0.505	0.009
Montauk	M2	0.413	0.289	0.124
POS	M2	0.478	0.402	0.077
POF	M2	0.494	0.420	0.075
Newport	N2	0.156	0.107	0.049
Montauk	N2	0.129	0.067	0.062
POS	N2	0.147	0.085	0.061
POF	N2	0.152	0.091	0.061
Newport	S2	0.096	0.106	-0.010
Montauk	S2	0.075	0.048	0.027
POS	S2	0.092	0.085	0.007
POF	S2	0.093	0.090	0.004
Newport	K1	0.093	0.065	0.028
Montauk	K1	0.102	0.074	0.029
POS	K1	0.090	0.073	0.018
POF	K1	0.092	0.068	0.024
Newport	O1	0.063	0.048	0.015
Montauk	O1	0.069	0.047	0.021
POS	O1	0.062	0.046	0.015
POF	O1	0.063	0.049	0.014

Table 3-2 Tidal phase comparison between model predictions and observations for the most significant harmonic constants at Newport, Montauk, POS and POF.

Station	Const	Phase (deg) modeled	Phase (deg) observed	Difference (Model - Obs)	Difference (Model - Obs) minutes
Newport	M2	7	3	4	9
Montauk	M2	25	50	-25	-52
POS	M2	347	4	16	33
POF	M2	351	4	14	29
Newport	N2	353	353	-1	-1
Montauk	N2	8	31	-23	-48
POS	N2	333	351	-18	-38
POF	N2	335	353	-18	-37
Newport	S2	181	156	24	50
Montauk	S2	33	41	-8	-16
POS	S2	360	9	9	19
POF	S2	2	10	-8	-16
Newport	K1	181	156	24	50
Montauk	K1	181	166	15	32
POS	K1	171	158	13	27
POF	K1	172	159	13	26
Newport	O1	176	207	-31	-64
Montauk	O1	176	213	-37	-76
POS	O1	168	200	-32	-67
POF	O1	168	205	-37	-77

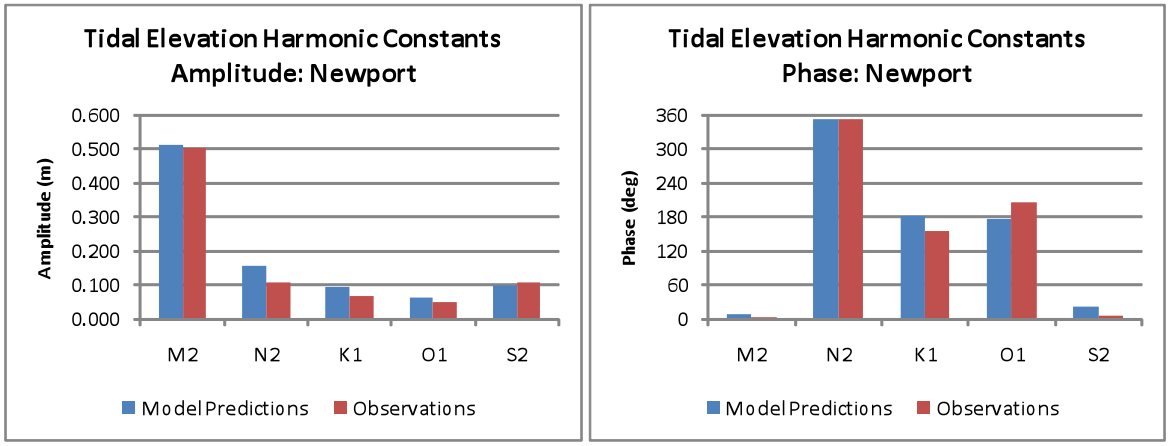

Figure 3-10 Comparison of model predicted and observed tidal harmonic constituent amplitudes and phases for Newport.

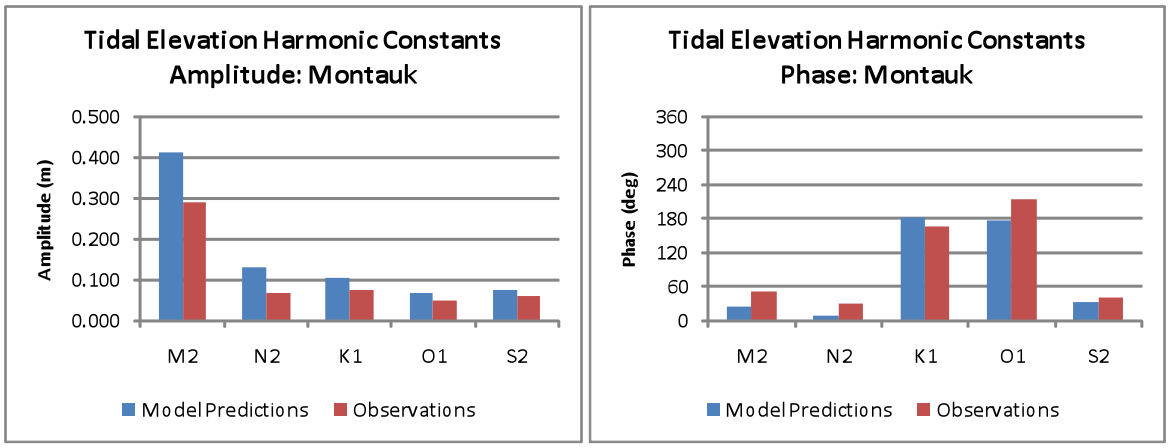

Figure 3-11 Comparison of model predicted and observed tidal harmonic constituent amplitudes and phases for Montauk.

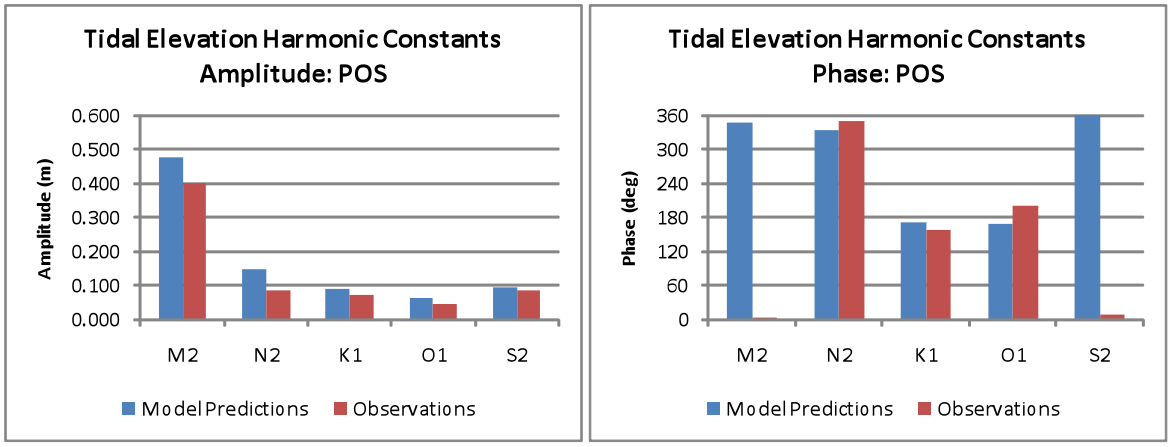

Figure 3-12 Comparison of model predicted and observed tidal harmonic constituent amplitudes and phases for Station POS.

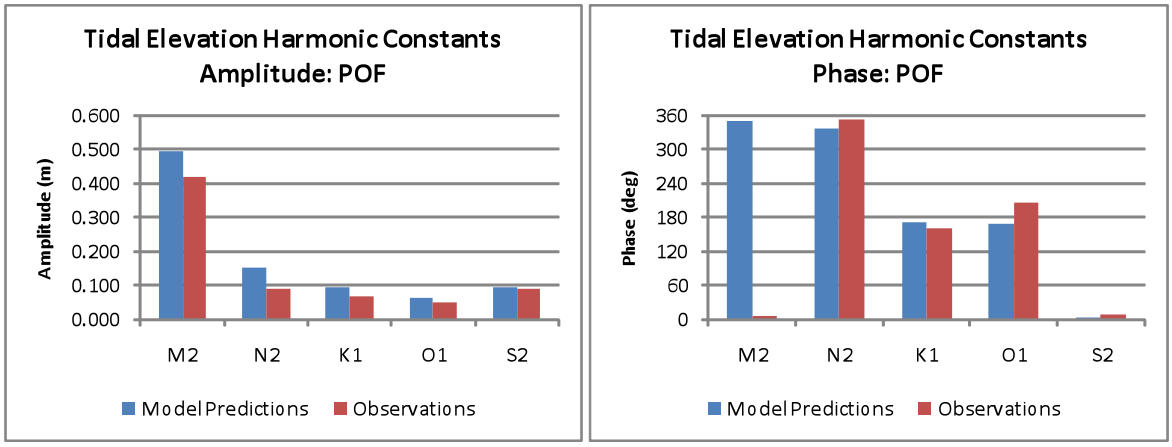

Figure 3-13 Comparison of model predicted and observed tidal harmonic constituent amplitudes and phases for Station POF.

3.2.2 Currents

The model predicted currents were compared to observation to evaluate the model performance. Time series comparisons and comparison of harmonic constituents and tidal ellipses sizes were performed for the study period.

Comparisons of observed vs. predicted currents were made at stations MDS, MDF, POS and POF; Figure 3-14 a & b through Figure 3-16 a & b show the comparison of east/west (U) and north/south (V) velocity components where blue lines represent the observations and green lines the model predictions. Reviewing the time series plots, several major features are apparent at all of the stations. In addition to the presence of the semi-diurnal component of the currents, attributable to the M2 tidal harmonic component as will be discussed below, there is a significant variability in the mean currents, clearly attributable to wind forcing. This response to the atmospheric forcing is most apparent in the U-component of the surface currents, and in the area south of Block Island (MDS and POS) where the currents may be forced to align somewhat in the east/west direction due to the presence of the island itself for wind driven events. It is also clear the model is reproducing both the regularity of the tidal forcing as well as the irregular, event driven response. These plots show that the model captured the trend of the mean current component magnitude as well as the amplitude and phase of each components signal. In addition a comparison of the three time series plots per page (representing the top, middle and bottom currents) shows that the model also represented the vertical profile well.

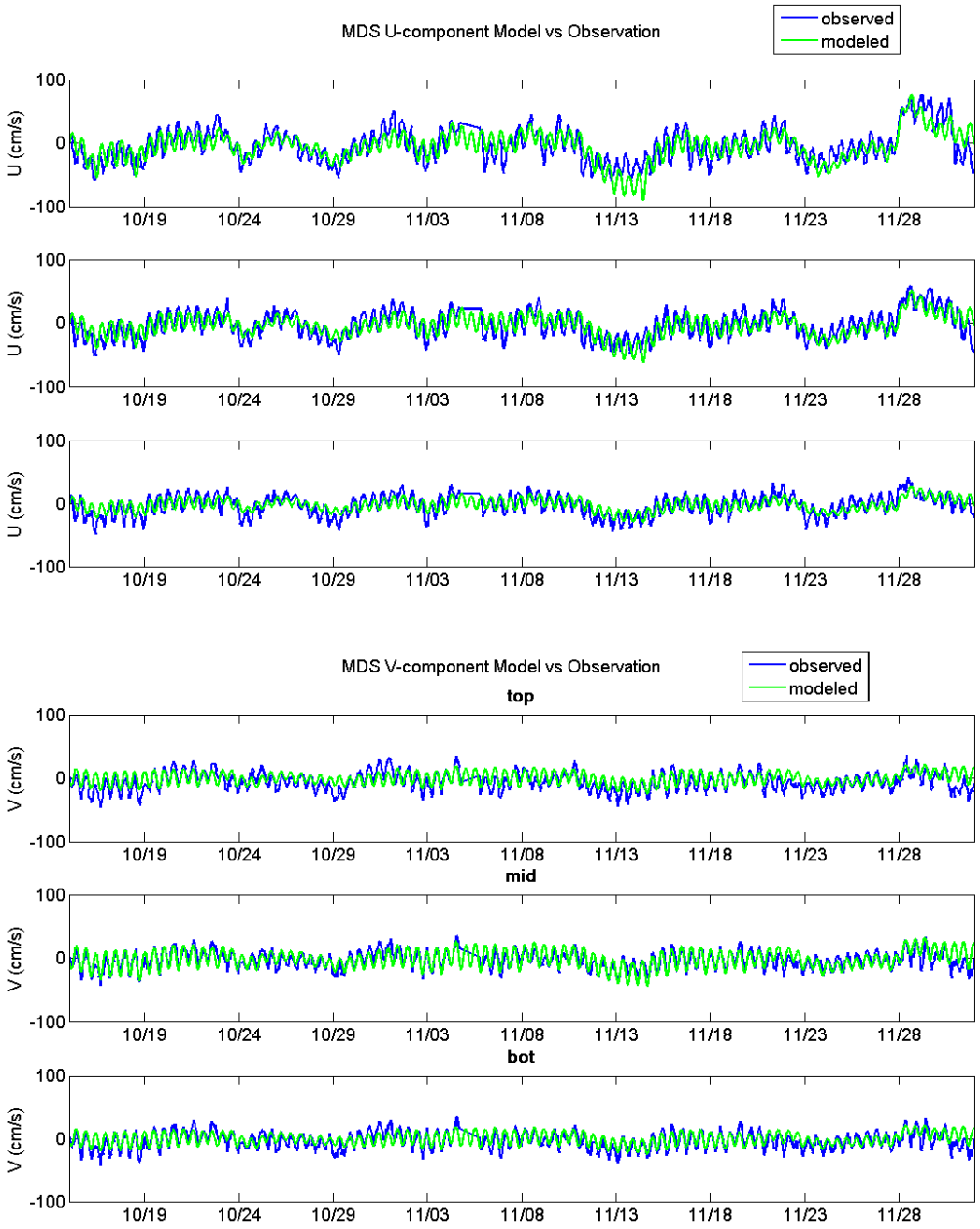

Figure 3-14 Time series comparison of model predicted and observed currents at MDS in the top, middle and bottom layers, for the: a) u-component and b) v-component.

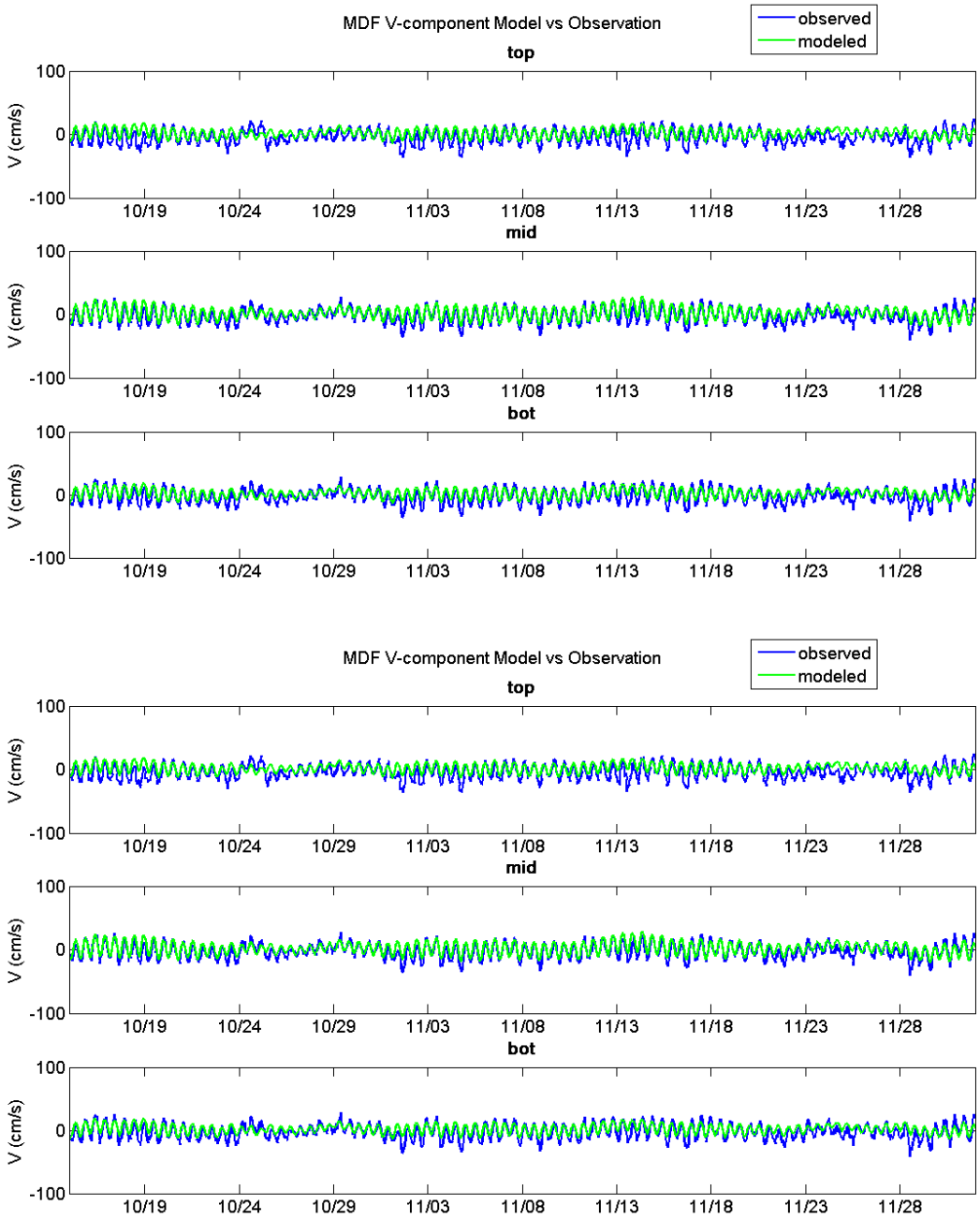

Figure 3-15 Time series comparison of model predicted and observed currents at MDF in the top, middle and bottom layers, for the: a) u-component and b) v-component.

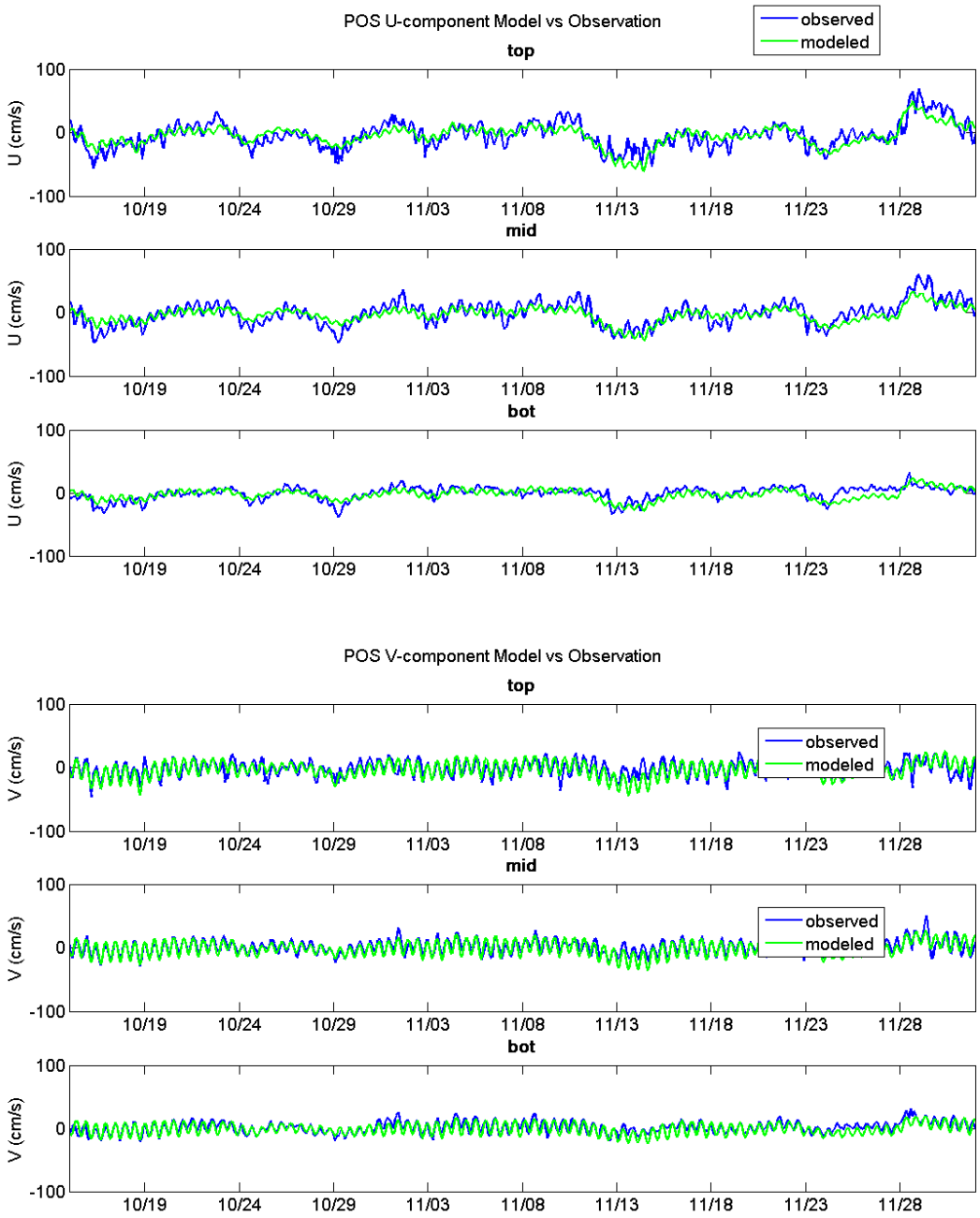

Figure 3-16 Time series comparison of model predicted and observed currents at POS in the top, middle and bottom layers, for the: a) u-component and b) v-component.

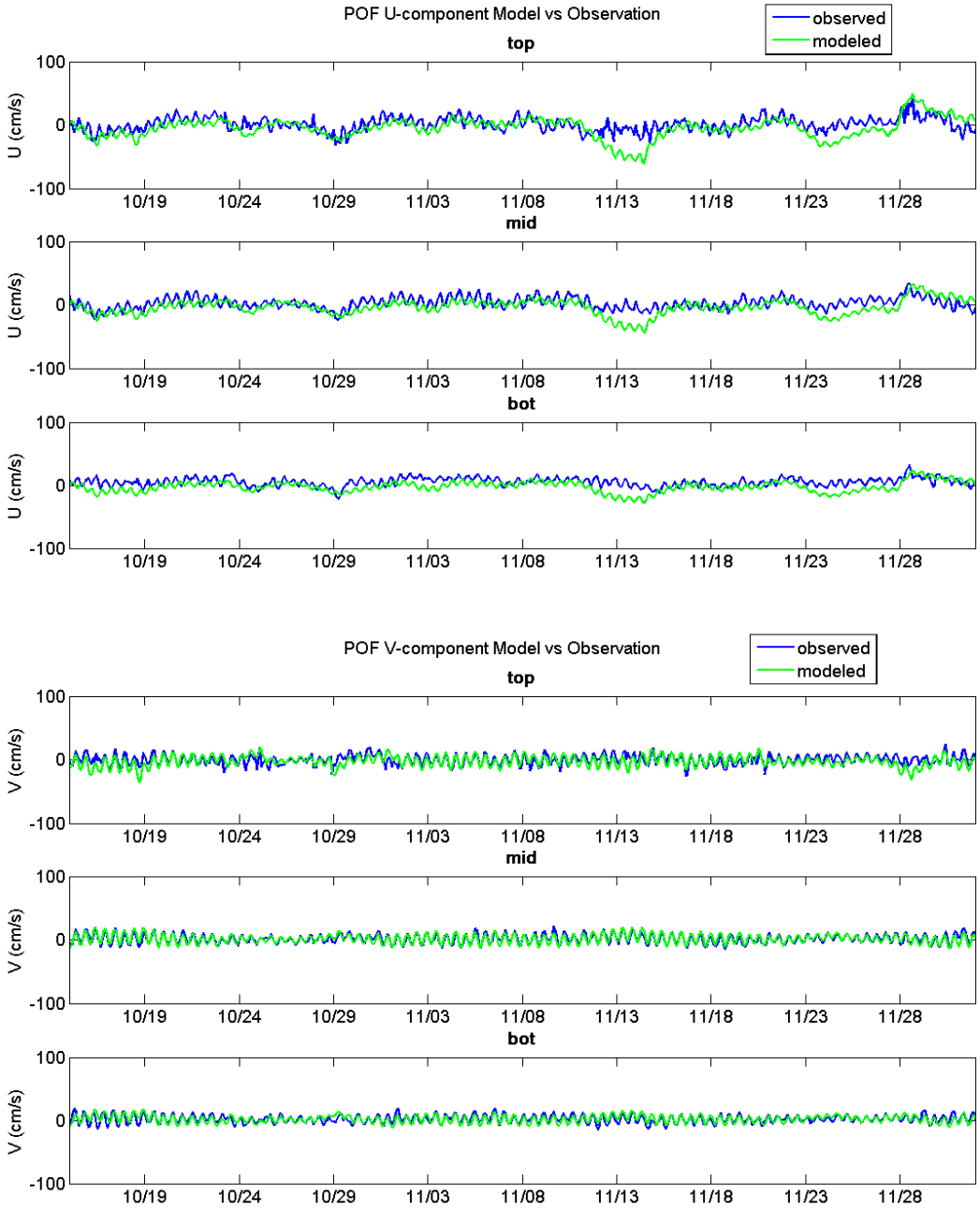

Figure 3-17 Time series comparison of model predicted and observed currents at POF in the top, middle and bottom layers, for the: a) u-component and b) v-component.

To further evaluate the model predictions, harmonic decomposition was performed on both the observed and predicted records of current velocity components for the surface, middle and bottom of the water column. This analysis yielded the major and minor axes of the current ellipses and phases of the contributing harmonic constituents for both observed and predicted current components. For each of the 4 stations the current ellipses were determined and based on

these results a summary of the comparisons is provided in Table 3-3 through Table 3-6 for stations MDS, MDF, POS, and POF respectively. Both observations and model predictions showed that the M2 frequency was the predominant current frequency, containing the majority of the tidal energy. The model predicted the M2 current amplitude best at surface and mid layers and had more variance at the bottom layer, furthermore predictions were better at stations closer to Block Island (MDS and POS) than those further away (at MDF, although the POF comparisons were remarkably good). At the farther stations this could be due to the reduced grid resolution and therefore resolution of bathymetric features in those areas.

Referring to the tables is can be seen that the differences between the model predicted and observed M2 constituent major axes are generally less than 0.02 m/s with a maximum deviation of 0.05 m/s in the MDF bottom current ellipse. The difference in the remaining constituents is variable, remaining less than 0.01 m/s for the majority. The M2 phase comparison between the model predictions and observations is similarly close, with the difference angle remaining less than about 10 degrees with an exception in the bottom currents at both the POS and POF stations. In general, the model predicted tidal current ellipses, driven predominantly by the M2 tidal component, show a close agreement with the observations indicating that the model captures the magnitude and the circulation patterns in the study area.

Table 3-3 Comparison of tidal current ellipses for significant harmonic constants at MDS.

Layer	Constituent	Frequency	Current Ellipse Major Axis (m/s) modeled	Current Ellipse Minor Axis (m/s) modeled	Current Ellipse Phase Angle (deg) modeled	Current Ellipse Major Axis (m/s) observed	Current Ellipse Minor Axis (m/s) observed	Current Ellipse Phase Angle (deg) observed	Major Axis Difference (Model - Obs)	Minor Axis Difference (Model - Obs)
top	O1	0.038731	0.02	0.01	104	0.04	0.01	192	-0.022	-0.003
top	K1	0.041781	0.02	0.01	112	0.04	0.01	178	-0.015	0.002
top	N2	0.078999	0.06	0.02	341	0.02	0.00	338	0.035	0.013
top	M2	0.080511	0.21	0.07	4	0.20	0.07	356	0.014	-0.004
top	S2	0.083333	0.04	0.01	9	0.02	0.01	341	0.012	-0.007
mid	O1	0.038731	0.02	0.01	103	0.03	0.00	173	-0.019	0.005
mid	K1	0.041781	0.02	0.01	105	0.04	0.01	178	-0.015	0.001
mid	N2	0.078999	0.05	0.02	335	0.02	0.01	6	0.030	0.001
mid	M2	0.080511	0.20	0.06	1	0.20	0.07	354	-0.001	-0.009
mid	S2	0.083333	0.03	0.01	6	0.02	0.01	318	0.009	0.000
bot	O1	0.038731	0.01	0.00	98	0.03	0.00	175	-0.015	0.000
bot	K1	0.041781	0.02	0.01	102	0.03	0.00	172	-0.018	0.004
bot	N2	0.078999	0.03	0.01	329	0.03	0.01	5	0.005	-0.003
bot	M2	0.080511	0.14	0.04	357	0.16	0.04	346	-0.022	0.005
bot	S2	0.083333	0.02	0.01	7	0.02	0.01	316	0.004	0.000

Table 3-4 Comparison of tidal current ellipses for significant harmonic constants at MDF.

Layer	Constituent	Frequency	Current Ellipse Major Axis (m/s) modeled	Current Ellipse Minor Axis (m/s) modeled	Current Ellipse Phase Angle (deg) modeled	Current Ellipse Major Axis (m/s) observed	Current Ellipse Minor Axis (m/s) observed	Current Ellipse Phase Angle (deg) observed	Major Axis Difference (Model - Obs)	Minor Axis Difference (Model - Obs)
top	O1	0.038731	0.01	0.00	107	0.03	0.01	157	-0.016	-0.009
top	K1	0.041781	0.01	0.01	127	0.04	0.02	6	-0.022	-0.016
top	N2	0.078999	0.03	0.00	295	0.04	0.02	303	-0.003	-0.015
top	M2	0.080511	0.13	0.04	322	0.15	0.10	310	-0.018	-0.058
top	S2	0.083333	0.03	0.01	314	0.03	0.02	302	0.000	-0.008
mid	O1	0.038731	0.01	0.00	112	0.02	0.01	150	-0.013	-0.009
mid	K1	0.041781	0.02	0.00	115	0.03	0.02	5	-0.018	-0.019
mid	N2	0.078999	0.04	0.01	293	0.04	0.02	301	-0.002	-0.011
mid	M2	0.080511	0.13	0.04	318	0.15	0.10	311	-0.022	-0.059
mid	S2	0.083333	0.03	0.01	315	0.03	0.02	299	-0.003	-0.008
bot	O1	0.038731	0.01	0.00	110	0.02	0.01	147	-0.013	-0.004
bot	K1	0.041781	0.01	0.00	112	0.03	0.02	359	-0.021	-0.018
bot	N2	0.078999	0.02	0.00	288	0.03	0.01	304	-0.009	-0.008
bot	M2	0.080511	0.09	0.03	313	0.14	0.10	311	-0.051	-0.063
bot	S2	0.083333	0.02	0.00	320	0.03	0.01	301	-0.010	-0.010

Table 3-5 Comparison of tidal current ellipses for significant harmonic constants at POS.

Layer	Constituent	Frequency	Current Ellipse Major Axis (m/s) modeled	Current Ellipse Minor Axis (m/s) modeled	Current Ellipse Phase Angle (deg) modeled	Current Ellipse Major Axis (m/s) observed	Current Ellipse Minor Axis (m/s) observed	Current Ellipse Phase Angle (deg) observed	Major Axis Difference (Model - Obs)	Minor Axis Difference (Model - Obs)
top	O1	0.038731	0.01	0.01	103	0.02	0.00	160	-0.014	0.003
top	K1	0.041781	0.02	0.01	108	0.03	0.01	199	-0.018	-0.004
top	N2	0.078999	0.03	0.01	328	0.02	0.01	323	0.011	-0.003
top	M2	0.080511	0.13	0.03	352	0.12	0.05	354	0.007	-0.027
top	S2	0.083333	0.02	0.00	358	0.01	0.01	325	0.007	-0.006
mid	O1	0.038731	0.01	0.01	105	0.03	0.00	160	-0.017	0.001
mid	K1	0.041781	0.02	0.01	107	0.04	0.01	181	-0.020	-0.005
mid	N2	0.078999	0.03	0.01	325	0.01	0.01	320	0.020	-0.004
mid	M2	0.080511	0.13	0.03	350	0.12	0.06	350	0.010	-0.034
mid	S2	0.083333	0.02	0.00	357	0.02	0.01	344	0.003	-0.007
bot	O1	0.038731	0.01	0.00	103	0.02	0.00	164	-0.007	0.003
bot	K1	0.041781	0.01	0.01	106	0.02	0.00	189	-0.008	0.006
bot	N2	0.078999	0.03	0.00	323	0.02	0.01	298	0.004	-0.002
bot	M2	0.080511	0.11	0.02	348	0.08	0.01	316	0.031	0.011
bot	S2	0.083333	0.02	0.00	0	0.02	0.01	9	0.001	-0.011

Table 3-6 Comparison of tidal current ellipses for significant harmonic constants at POF.

Laye	Constituen	Frequenc	Ellipse Axis modele	Ellipse Axis modele	Ellipse Angle modele	Ellipse Axis observe	Ellipse Axis observe	Ellipse Angle observe	Major Differenc (Model -	Minor Differenc (Model -
to	O	0.03873	0.0	0.0	10	0.0	0.0	10	-	0.00
to	K	0.04178	0.0	0.0	15	0.0	0.0	1	-	-
to	N	0.07899	0.0	0.0	29	0.0	0.0	32	0.00	-
to	M	0.08051	0.0	0.0	32	0.0	0.0	30	0.00	-
to	S	0.08333	0.0	0.0	31	0.0	0.0	31	0.00	-
mi	O	0.03873	0.0	0.0	11	0.0	0.0	12	-	0.00
mi	K	0.04178	0.0	0.0	11	0.0	0.0	16	-	-
mi	N	0.07899	0.0	0.0	29	0.0	0.0	30	0.00	-
mi	M	0.08051	0.0	0.0	31	0.0	0.0	31	0.00	-
mi	S	0.08333	0.0	0.0	31	0.0	0.0	31	0.00	0.00
bo	O	0.03873	0.0	0.0	11	0.0	0.0	13	-	0.00
bo	K	0.04178	0.0	0.0	11	0.0	0.0	7	-	-
bo	N	0.07899	0.0	0.0	28	0.0	0.0	26	-	-
bo	M	0.08051	0.0	0.0	31	0.0	0.0	28	-	-
bo	S	0.08333	0.0	0.0	32	0.0	0.0	27	0.00	0.00

Figure 3-18 and Figure 3-19 show examples of model predicted flood and ebb tidal surface currents in the OSAMP and RE zone area, respectively. The OSAMP area, covering the area between the entrance to Long Island Sound on the west, to the entrance to Buzzards Bay to the east and Narragansett Bay to the north is clearly a complicated domain. During the flood tide, the currents essentially bifurcate near the center of the OSAMP area (Rhode Island Sound), heading west into Long Island Sounds at the western edge, east into Buzzards Bay on the eastern edge and north into Narragansett Bay to the north. The currents exhibit the opposite pattern on the ebb tide. An acceleration of current speeds is clearly seen in the narrow straights between the eastern end of Long Island and Block Island during both the flood and ebb stages. This partly due to the narrowing of the area feeding Long Island Sound and partly due to the shallow areas on both sides of the central channel through the straights (see Figure 3-5).

The complicated flood and ebb patterns seen in the larger OSAMP domain, affect the circulation patterns in the RE zone south of Block Island as well. There is often a split in the flow to either side of the island during both flood and ebb stages, where the current speeds are considerably larger on the west side of the zone as a function of the narrowing and swallowing of the straights area between Block Island and Long Island (Figure 3-19). Model predicted surface current speeds in the RE zone range from a high of 0.5 (m/s) in the western portion to 0.25 (m/s) to the area southeast of Block Island.

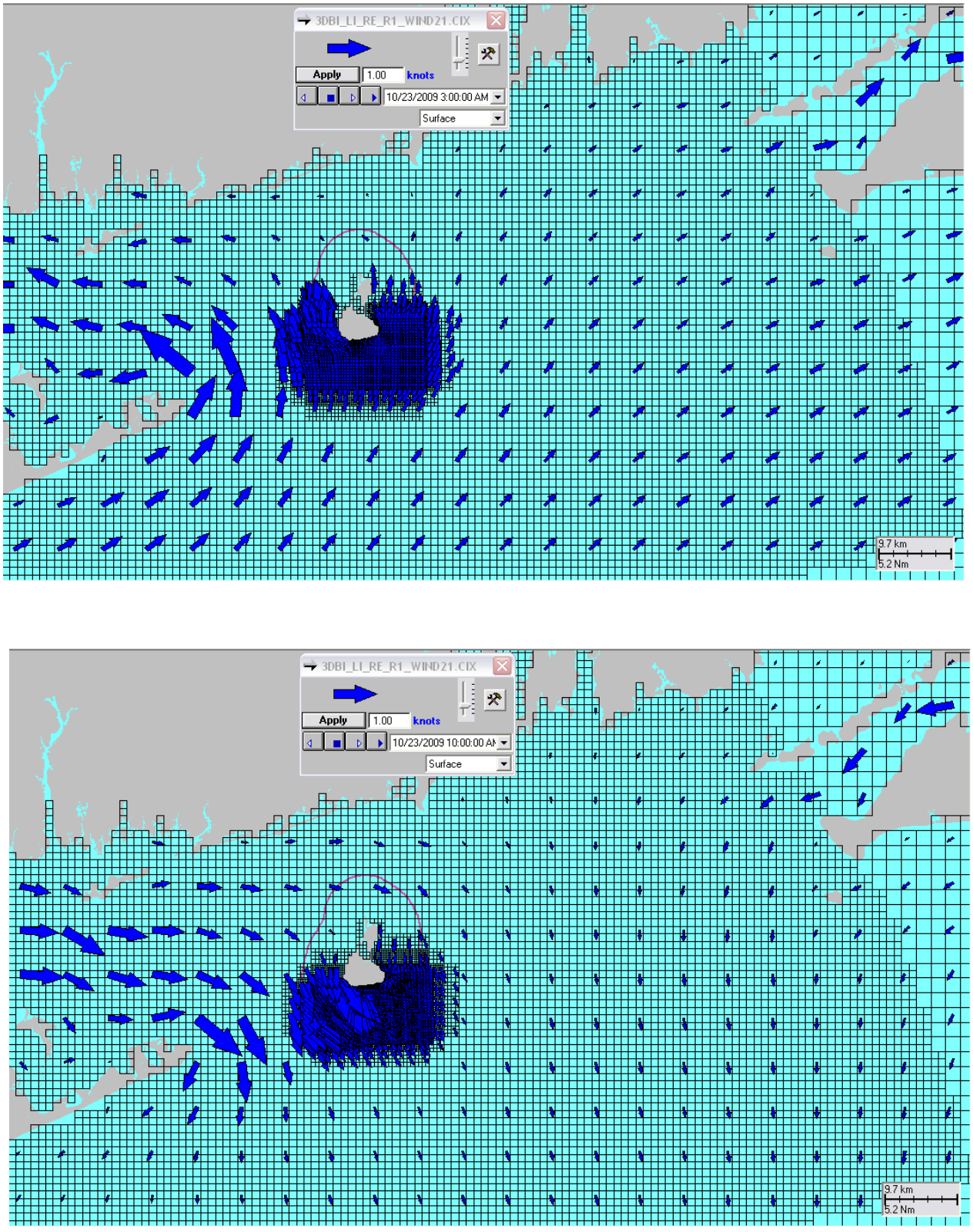

Figure 3-18 Example model predicted surface current vector map for the OSMAP area, showing every third current vector for: a) flood tide and b) ebb tide.

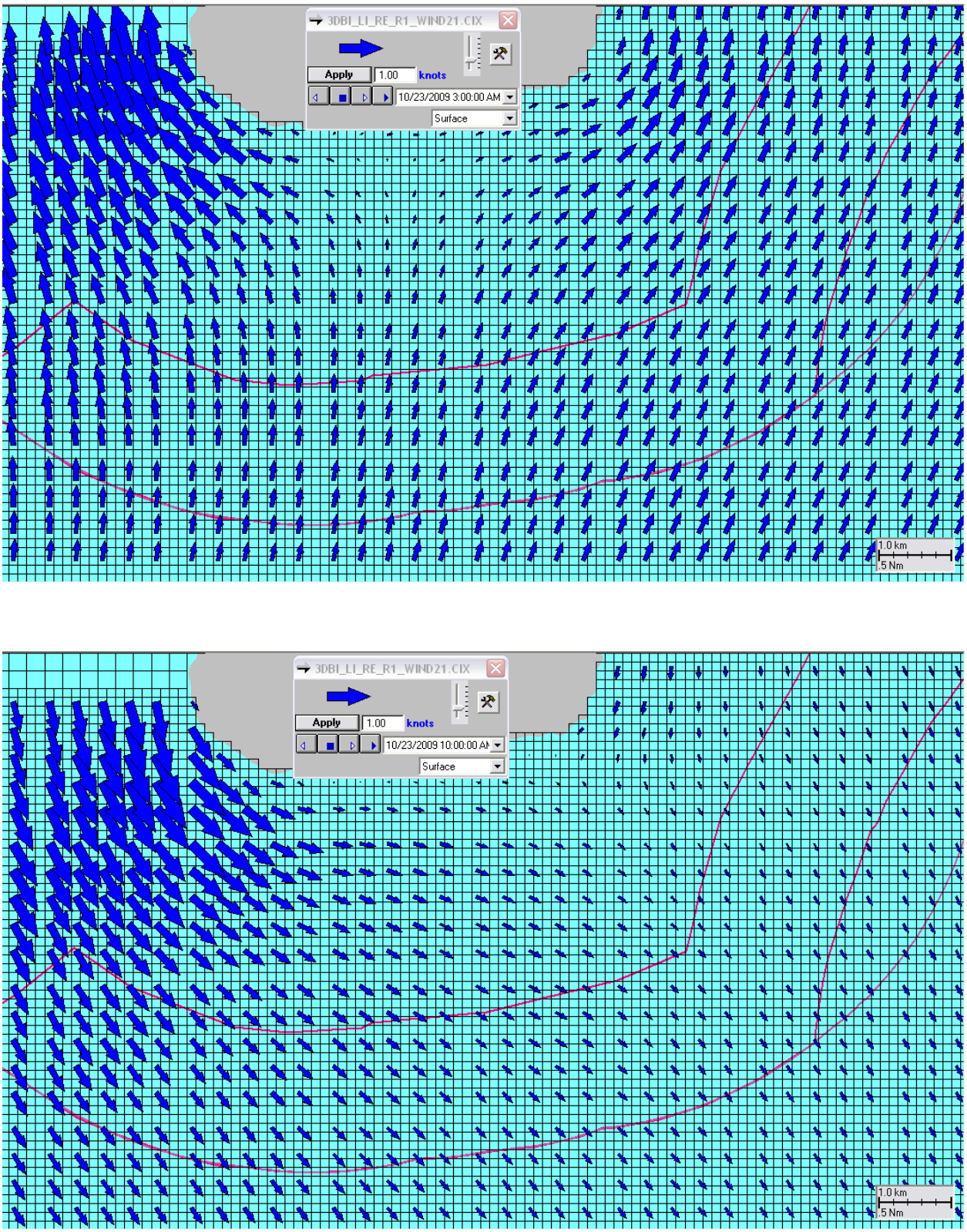

Figure 3-19 Example model predicted surface current vector map in the RE zone for: a) flood tide and b) ebb tide.

The model predicted bottom currents in the RE zone are presented in Figure 3-20(a) and (b) for the flood and ebb tidal stages respectively. Again, the currents show a large variability ranging from the largest currents, 0.25 (ms/) in the western portion of the RE zone near the straights to the smallest currents 0.15 (m/s) in the deeper eastern section near the shipping channel. Figure 3-21(a) and (b) show the contours of bottom current speed for these examples of flood and ebb.

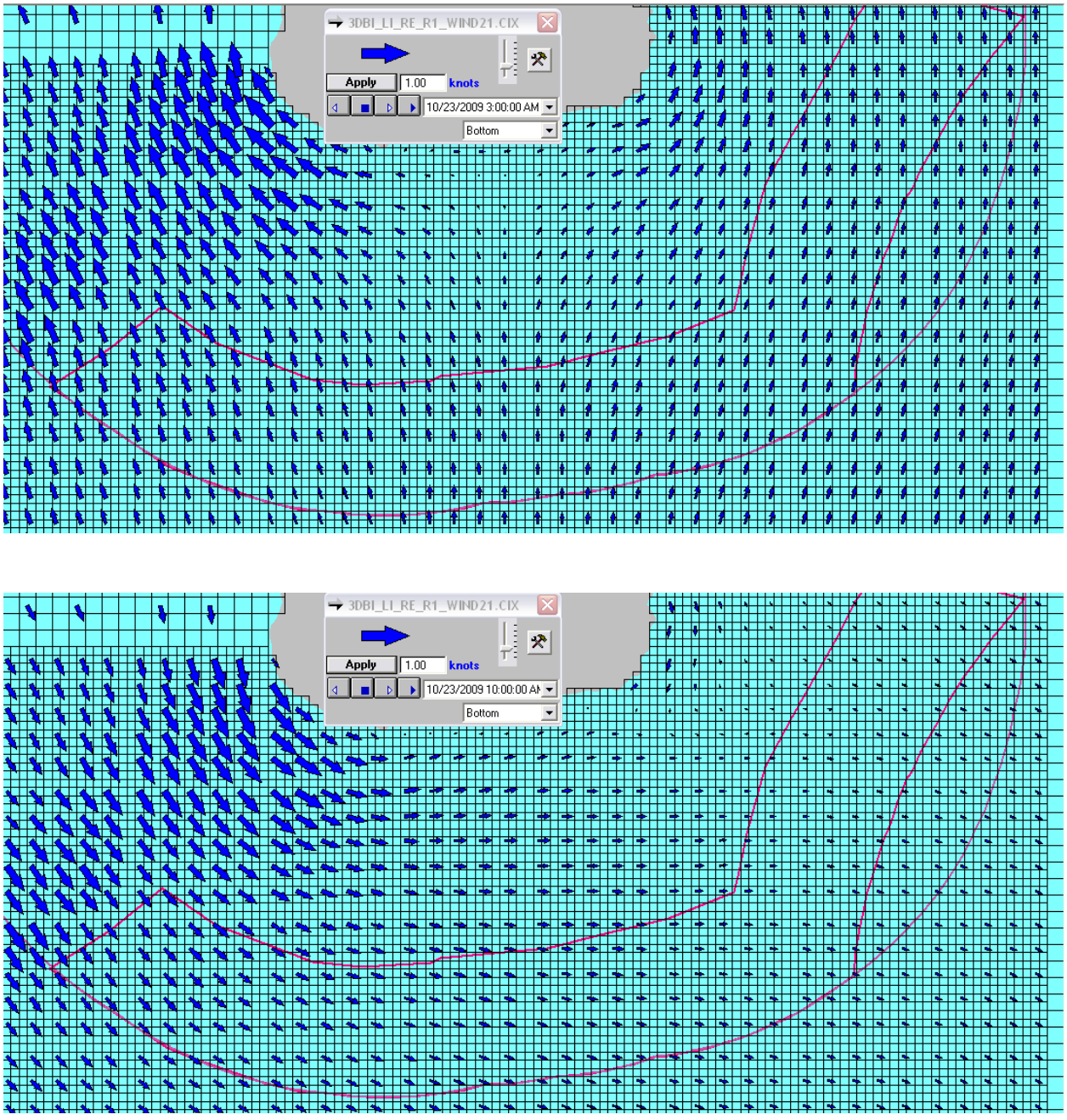

Figure 3-20 Example model predicted bottom current vector map in the RE zone for: a) flood tide and b) ebb tide.

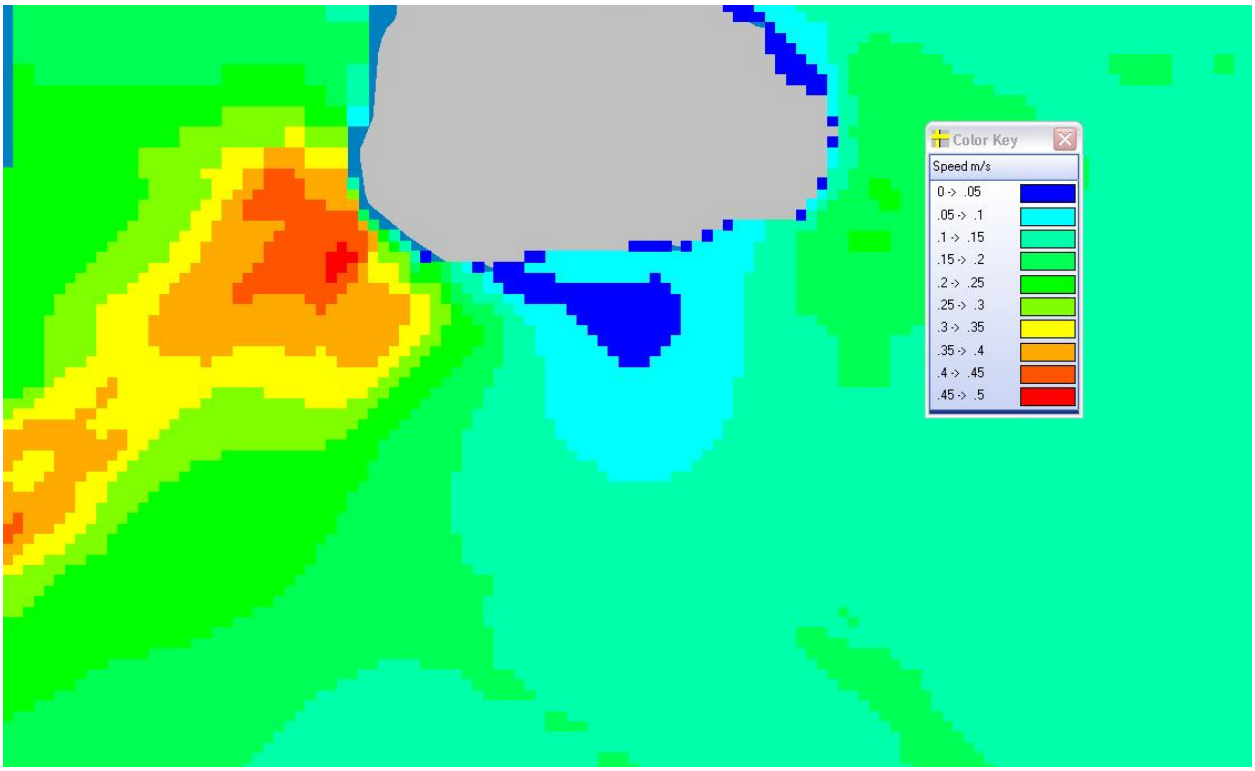

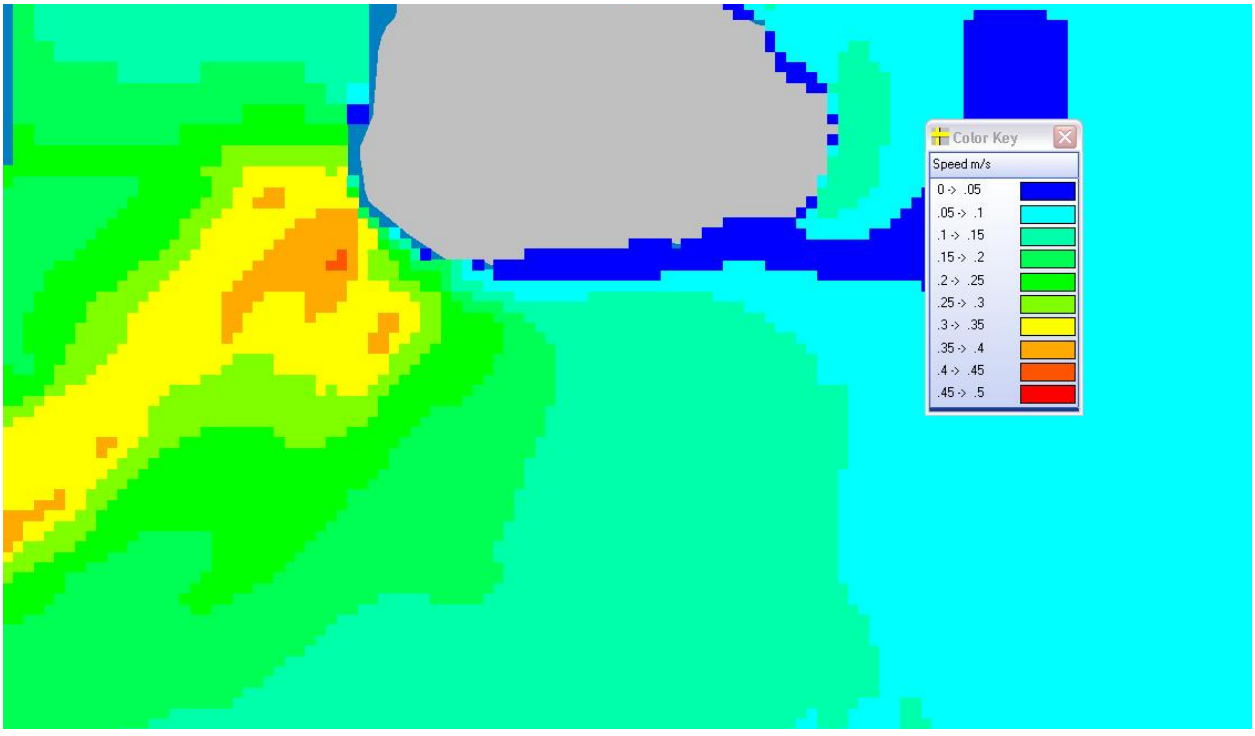

Figure 3-21 Example model predicted bottom current speed map in the RE zone for: a) maximum flood tide and b) maximum ebb tide.

4 Discussion and Conclusions

It has been proposed that a wind turbine farm be developed off the southeastern coast of Block Island, south of the Rhode Island mainland. The development of an offshore wind farm will necessarily require a great deal of underwater construction including drilling and setting the piles for the turbine foundations, burying electrical transmission cables and other infrastructure construction tasks. During this period additional water column suspended sediments may impact the construction areas and it is therefore of interest to understand what the current speeds and circulation patterns are in the development area. To that end, Applied Science Associates, Inc. (ASA) has performed a hydrodynamic modeling study to estimate the currents and circulation in the renewable energy (RE) development area with a focus on bottom stress and currents. The results of the study will be used by URI scientists to determine the potential for sediment re-suspension and transport of suspended sediment that might results from the construction and operation of the small wind farm.

ASA used the HYDROMAP model system, which calculates velocity vectors on a stepwise continuous variable rectangular grid system. A benefit of the model is that it allows coarse grid resolution in the areas offshore the coast of Rhode Island and finer resolution in the Block Island Sound area and renewable energy zone area of interest. The model was driven by tidal harmonic data along the open boundaries and wind stress at the surface. The model predictions were compared to observations collected as part of the OSAMP, including four ADCP current meter locations and NOAA tidal elevation data at Montauk and Newport. The comparisons showed that the model not only adequately predicted the tidal forcing response in the study area, but also the longer period episodic wind driven events that are characterized by passing weather systems. The model appeared to be able to reproduce both the horizontal spatial variability in the system as well as the vertical profile of the currents, as represented by the ADCP observations at the surface, mid and bottom of the water column.

Both observations and the model predictions confirm that the dominating tidal constituent is the M2 constituent which represents between 50-60% of the total tidal amplitude at all stations. The amplitude predictions for all constituents tend to be higher than the observed but are generally within 20% of the observed with the exception of Montauk. The Montauk station is located in the shallows of an embayment that the mode grid does not resolve in fine detail, this may contribute to the over prediction of tidal amplitude.

Review of the current analysis indicates that the differences between the model predicted and observed M2 constituent major axes are generally less than 0.02 m/s with a maximum deviation of 0.05 m/s in the MDF bottom current ellipse. The difference in the remaining constituents is variable, remaining less than 0.01 m/s for the majority. The M2 phase comparison between the model predictions and observations is similarly close, with the difference angle remaining less than about 10 degrees with an exception in the bottom currents at both the POS and POF stations. In general, the model predicted tidal current ellipses, driven predominantly by the M2 tidal component, show a close agreement with the observations indicating that the model captures the magnitude and the circulation patterns in the study area.

The bottom currents were further reviewed and an understanding of the bottom speed developed. The renewable energy zone follows the edge of the 3 mile state waters limit along the southern portion of the line, from the straights between Long Island and Block Island to the west, to the shipping channel exclusion zone on the east. The zone is approximately 2 km wide, and has a bulge on the east side representing the shipping channel exclusion zone. Bathymetry in the RE zone is quite variable ranging from less than 10m, in the western portion to greater than 35m to the east. This bathymetric range and the straights to the west produce a significant variability in the bottom speeds as well, ranging from a high in the shallow western portions of 0.25 m/s down to a high in the eastern portions of 0.15 m/s.

5 References

Davies, A.M. 1977: The numerical solutions of the three-dimensional hydrodynamical equations using a B-spline representation of the vertical current profile. Bottom Turbulence. Proc. 8th liege colloquium on Ocean hydrodynamics. J. C. J. Nihoul. Ed.. Elsevier. 27-48.

Gordon, R.B. and M.L. Spaulding, 1979. A nested numerical tidal model of the Southern New England Bight. Report to NOAA, Hampton, VA, From Univ. of Rhode Island, Kingston RI.

Isaji, T.E., Howlett, C. Dalton and E. Anderson, 2001. Stepwise- continuous-variable-rectangular grid, in Proceedings of the 7th International Conference on Estuarine and Coastal Modeling, St. Pete Beach, FL, November 5-7, 2001.

Isaji, T. and M. Spaulding, 1984. Notes and Correspondence. A model of the tidally induced residual circulation in the Gulf of Maine and Georges Bank, *Journal of Phys. Ocean.,* June. pp. 1119-1126.

Mukai, A.M., Westerink, J.J., and Luettich, R.A., 2001. Guidelines for using the Eastcoast 2001 database of tidal constituents within the western North Atlantic Ocean, Gulf of Mexico

and Caribbean Sea, Coastal and Hydraulics Technical Note CERD/CHL CHTEN-IV-40, U.S. Army Engineer Research and Development Center, Vicksburg, MS.

National Geophysical Data Center, 1998. GEOphysical Data System for Hydrographic Survey Data, National Ocean Service, Ver. 4.

National Geophysical Data Center, 2001. 2-Minute gridded global relief data, (October 2001) CD-ROM.

Owen, A., 1980. A three-dimensional model of the Bristol Channel. J. Phys. Oceanog. 1987. 10, 1290-1302.